CHARACTERIZATION OF SANDWICH PANELS SUBJECT TO LOW-VELOCITY IMPACT

Non-Destructive and Destructive Inspection of Non-standard Sandwich Composite Panels

CARACTÉRISATION DES PANNEAUX SANDWICH SOUMIS À UN IMPACT À FAIBLE VITESSE

Inspection non-destructif et destructif de panneaux non-standards en composite sandwich

A Thesis Submitted to the Division of Graduate Studies
of the Royal Military College of Canada
by

Stephen Prior, BEng, rmc

Captain

In Partial Fulfillment of the Requirements for the Degree of
Master of Applied Science in Aeronautical Engineering

April, 2016

To my future wife Christina, your support during my years of study has kept me focused and exceedingly happy. To Mom and Dad, thank you for being the best parents a son could have. Growing up near base and looking up at aircraft is what first made me wonder about how it all works; this early inspiration has driven my journey to learn more and more.

Acknowledgments

I would like to thank my supervisors Dr. Diane Wowk and Dr. Catharine Marsden for their guidance at the Royal Military College of Canada and making possible the internship at National Research Council of Canada (NRC).

The following group from the Aerospace Portfolio of NRC aided my research during the summer and assisted in my experimentation. Their practical insight and experience was beneficial to the development of a fixture and they provided the proper methodology regarding impact testing, sectioning and mounting specimens, microscopy and NDI techniques. A special thanks to Bob Rutledge, Marko Yanishevsky, Richard Desnoyers, John Rogers, John MacMillan, Michael Brothers, Ali Merati, Rick Cole, Olga Lupandina, Roy Campbell, Shashank Pant, Andre Beltempo, Lucy Li, Marc Genest and others who provided help along the way. You were all friendly and very accommodating during my internship, and your assistance provided insight regarding full-scale testing and facilitated what made my thesis possible.
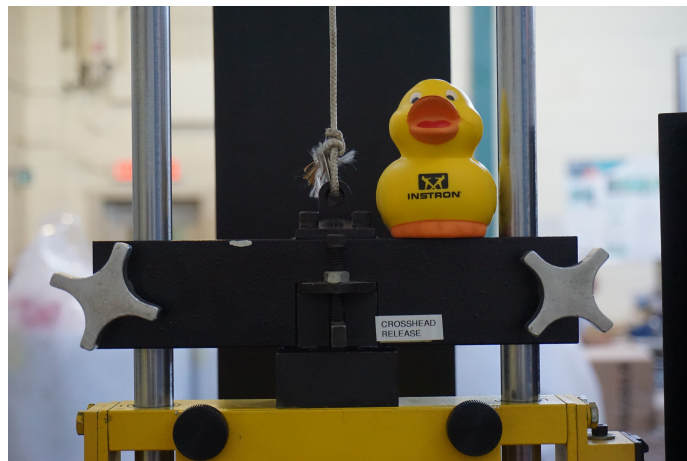
Abstract

Low-velocity impact on composite sandwich structure is a concern in the aerospace community, which has led to academic and industry investigation of failure modes, strength reduction and damage tolerance of structures with special attention to barely visible impact damage. Blunt impact as a result of tool drops or ground handling accidents may cause damage to the facesheet and core compromising the integrity of the panel while leaving minimal surface indication.

This research characterizes damage as a result of out-of-plane impact of selected non-standard sandwich panels. Panels consist of carbon-fibre reinforced epoxy facesheets, and an aluminum alloy honeycomb core; thicknesses of facesheets, core, and density of core were varied for the panels.

A fixture was designed to allow for a drop-weight impact tower to contact panels perpendicular to their upper surface. Following impact, dents were measured via micrometer and laser topography. Underlying panel damage was characterized with through-transmission ultrasound, radiography and an in-house damage detection method named the C-scan tap test which detected changes in local stiffness similar to the computer-aided tap test. Non-destructive methods were followed by a sectioned characterization of the damage through the impact zones.

Four studies were carried out, looking at how damage is affected by impactor diameter, impact on a repaired panel, the effectiveness of the C-scan tap test, and the presence of longterm dent relaxation. Hemispherical impactor diameter was shown to influence damage area and failure mode for a given impact energy level. Impact on a repaired panel led to significant hidden damage underneath the repair patch. The C-scan tap test performed well when compared to ultrasound and radiography. Longterm dent relaxation was minimal for the panel studied, less than 30 μm over a week-long period.

Keywords: low-velocity impact, characterization, composites, CFRP, sandwich panels, honeycomb, non-standard panels, impactor diameter, fail-

ure mode, repaired panel, BVID, tap test, computer-aided tap test, CATT,
dent relaxation, drop-weight impact

Résumé

L'impact à faible vitesse sur une structure fabriquée en sandwich composite est une préoccupation dans la communauté aérospatiale et le sujet d'enquête universitaire et industrielle sur les modes de défaillance, la réduction de la force et de la tolérance aux dommages des structures avec une attention particulière aux dommages d'impact à peine visible. Un impact contondant résultant d'outils échappés ou d'accidents de manutention au sol peut causer des dommages au revêtement et au noyau compromettant l'intégrité du panneau tout en laissant de minuscules traces sur la surface.

Cette recherche caractérise les dommages d'impact perpendiculaire sur des panneaux sandwich non-standards. Les panneaux sont composés d'un revêtement d'epoxy renforcé de fibres de carbone, et un âme nid d'abeilles en alliage d'aluminium; l'épaisseur du revêtement, de l'âme, et la masse volumique de l'âme ont été variées pour les panneaux.

Un gabarit a été conçu pour permettre aux masses d'un tour d'impact de frapper les panneaux perpendiculairement à leur surface supérieure. Après le choc, les bosses ont été mesurés avec un micromètre et par topographie laser. Les dommages du panneau sous-jacent ont été caractérisés par échographie par transmission, radiographie et une méthode propriétaire de détection de dommage nommée test marteau C-scan qui détecte des changements dans la rigidité locale de façon similaires au test marteau assistée par ordinateur. Les méthodes non destructives ont été suivies par une caractérisation en coupe des dommages dans les zones d'impact.

Quatre études ont été réalisées, spécifiquement les dommages varient selon le diamètre de l'impacteur, l'impact sur un panneau réparé, l'efficacité du test marteau C-scan, et la détente à long terme des bosses. Le diamètre de l'impacteur hémisphérique influence la taille des dommages et le mode de défaillance pour un niveau d'énergie d'impact donnée. L'impact sur un panneau réparé resulte en des dommages importants cachés sous la pièce de réparation. Le test marteau C-scan donne des résultats comparables à l'échographie et la radiographie. La détente à long terme fut minime pour le panneau

étudié, moins de 30 µm sur une période d'une semaine.

Mots-clés: impact à faible vitesse, caractérisation, composites, PRFC, panneaux sandwich, nid d'abeilles, panneaux non-standards, diamètre de l'impacteur, modes de défaillance, panneau réparé, BVID, test marteau, test marteau assistée par ordinateur, CATT, détente à long terme, essai d'impact par chute

Contents

List of Tables

List of Figures

List of Acronyms

BVID	Barely-Visible Impact Damage
CAI	Compression-After-Impact
CATT	Computer-Aided Tap Tester
CFRP	Carbon Fibre Reinforced Plastic
GFRP	Glass Fibre Reinforced Plastic
HEWABI	High-Energy Wide-Area Blunt Impact
MIA	Mechanical Impedance Analysis
NDI	Non-Destructive Inspection

1 Introduction

The need for strong and lightweight materials in the aerospace industry has led to a greater application of composite materials due to their high specific strength and stiffness. Composites fall into various classes, as seen in Figure 1.1. A sandwich panel is a structural composite, and often combines fibre-reinforced composites for either the facesheets (e.g. carbon fibre reinforced plastic, CFRP), the core (e.g. Nomex) or both. Common facesheet materials are aluminum alloy and CFRP, while common core materials are aluminum honeycomb, Nomex, and foam.
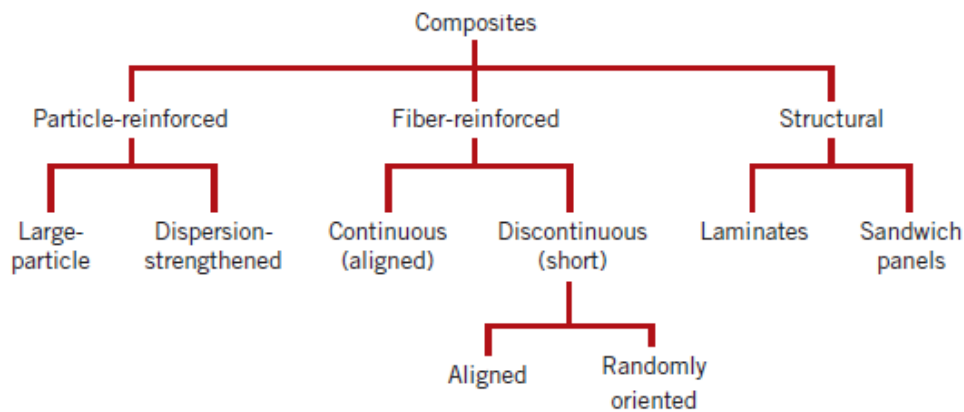
Figure 1.1: Classes of composite materials [1].

A sandwich panel has two high strength facesheets separated by a bonded lightweight core (Figure 1.2), leading to a strong structure in bending.[1] This

---

[1] A very basic form of sandwich panel is cardboard. Cardboard is stiffer than thin pieces of paper alone, and is used to make rigid boxes which have good strength for a minimal weight increase.
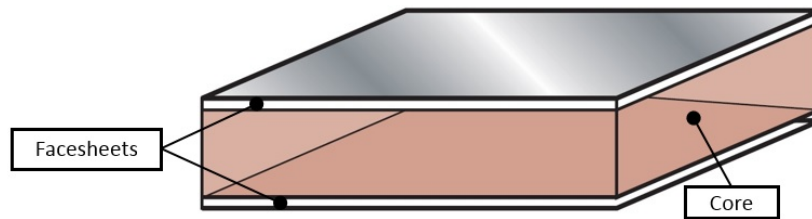
Figure 1.2: A sandwich panel (modified from [2]).

yields the same benefits of an I-beam with one distinct advantage: it provides continuous support for the facings (versus a single web supporting the flanges). This continuous support of a sandwich structure is especially useful in aerodynamic applications as seen in Figure 1.3 where warping could cause added drag, decreased airfoil efficiency and problematic aeroelastic effects [3].
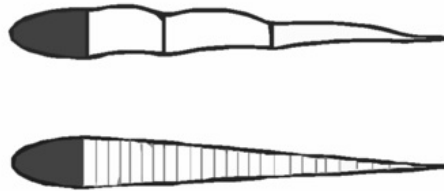
Figure 1.3: Exaggerated skin deflection of a typical wing structure (top) versus honeycomb (bottom) due to aerodynamic loading.

Sandwich panels provide excellent specific stiffness in bending as seen in Figure 1.4, and are ideally suited for aerospace applications including aircraft flooring, interiors, as well as aerodynamic and control surfaces [4]. Aluminum honeycomb is used as a high shear strength core material. Figure 1.5 shows a honeycomb core; it is constructed by bonding periodically along sheets of aluminum, and then expanded to the honeycomb shape.[1] This gives the material greater shear strength along the bonded, or ribbon direction of the honeycomb.

While sandwich structures have many benefits, one concern in the aerospace community is their integrity when impacted out-of-plane. Out-of-plane impact can lead to various complex failure modes, often with damage of both the facesheet and core. Cores are softer than facesheet material in the out-

---

[1]Honeycomb is standardized using a weight for a given volume such as pounds per cubic foot (pcf) or kilograms per cubic meter.
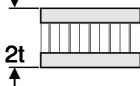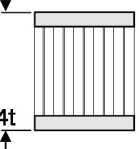
	Solid Material	Core Thickness t	Core Thickness 3t
Stiffness	1.0	7.0	37.0
Flexural Strength	1.0	3.5	9.2
Weight	1.0	1.03	1.06

Figure 1.4: Separation of high strength facesheets provides additional stiffness with minimal weight penalty [4].
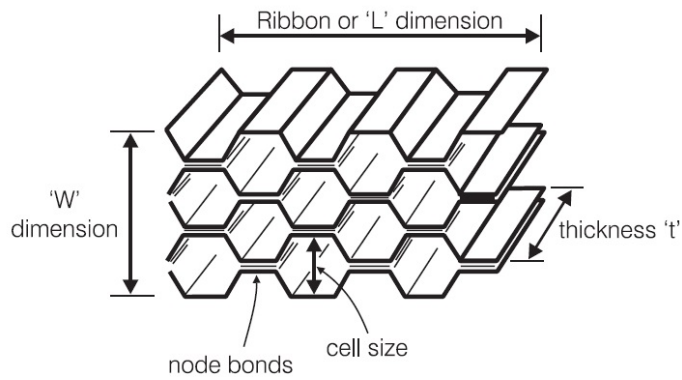
Figure 1.5: Honeycomb shape showing ribbon direction, transverse 'W' direction, thickness, node bonds and cell size [5].

of-plane (thickness) direction and absorb more of the impact energy than the facesheet, and the stiffer facesheets may rebound concealing core damage from an impact event.

1.1 Motivation

This thesis investigates damage characteristics caused by low-velocity impact on composite sandwich panels. While a ballistic impact will leave a clear indication of damage due to penetration, a blunt low-velocity impact may show limited to no visual indication of damage depending on the materials used and construction of the panels.

Impact damages may be detected by on-board monitoring systems. Acoustic emission has been shown to be able to detect crack initiation in composite panels and subsequent damage propagation under loading [6]. Acoustic instrumentation is also able to determine the location of damage sites since some of the energy that occurs from impact events is in an acoustic form, and growing damages may be detectable. An application of an acoustic monitoring system was the space shuttle Columbia, outfitted with acoustic emissions equipment in order to detect impacts on the wing leading edge [7]. Monitoring damage in this way is not always practical, and most aerospace structures do not detect damages as they occur; instead, regular inspections are performed in order to ensure no damage is present. The most frequent inspections are visual. If damage is not visually detected, this means damage may exist in the material for prolonged periods of time before a more detailed inspection can be performed. Damages that will go undetected between inspections should be assumed to exist in the structure as part of a damage tolerant design philosophy, and factored into the strength of the structure [8, 9].

While sandwich composites offer many design advantages, there are some particular areas of concern. Out of plane impact via tool drop, hail, and ground handling operations (to name a few) can cause damage to either the facing of the sandwich composite, the core, or both. If a laminate such as carbon fibre reinforced plastic (CFRP) is used, there is a possibility that the dent can relax, obscuring possible damage underneath the facing which cannot be visually detected. This damage results in a reduction of strength, and has potential to grow over time under spectrum loading, further reducing strength.

One of the greatest structural threats is blunt, low-velocity impact from ground service equipment; 60% of minor damage for commercial aircraft has been due to ground vehicles and equipment [10] and a report from National Aerospace Laboratory (Amsterdam) surveyed Schiphol Airport noting that

one ground handling incident with aircraft damage occurred for every 5000 flights [11], a statistic which likely extends to airports around the world. Addressing these accidents leads to significant repair costs and reduced flight hours, but also leads to some concern regarding the possibility of unreported accidents that leave no visual indication of damage.

Impact may cause damage to the facesheet of a sandwich panel which may lead to water or hydraulic fluid ingress. This can cause corrosion for metallic sandwich components, weaken the strength and stiffness of fibre-reinforced composites or degrade the facesheet-to-core adhesive leading to disbond.[1] Fluid ingress is an ongoing concern for both the commercial and military community [12, 13]. Disbonding of sandwich structure may lead to severe in-flight accidents as a result of low-pressure loading at altitude and flutter. 6 March 2005, Air Transat Flight 961 at 35000 ft above sea level lost a large portion of the rudder as seen in Figure 1.6, which was likely the result of a significant disbond and subsequent failure due to flutter. The aircraft experienced a loss of directional stability making the aircraft difficult to control. During landing the rudder control inputs were not effective; fortunately, the aircraft landed safely [13].

The majority of published work looks at testing or numerical analysis of standardized samples, usually with simplified designs. This thesis will look at a few specimens from a high performance aircraft horizontal stabilizer that were previously sectioned for an aerodynamic weighting survey. The panels studied contain changes in core density and facing ramps (locations where plies increase or decrease). A method will be proposed to induce and to characterize impact damage for such non-standardized panels.

---

[1]Fluid in control surfaces may also cause adverse effects due to the additional mass and change of the component's center of gravity. Water may also change state due to cold temperatures at altitude or hot temperatures on the ground which may increase the pressure inside the sandwich panel causing damage (e.g. blown core).

Figure 1.6: View of vertical tail plane and the remainder of the rudder from Air Transat Flight 961 [13].

1.2 Goals

Four studies were explored on non-standard panels to achieve the following goals:

1. Explore different failure modes by varying impactor diameter
2. Compare impact on a repaired and regular panel
3. Develop a non-destructive method to detect damage
4. Analysis of dent relaxation over time

The real panels available for testing were well-suited for exploratory research. The aforementioned goals will help to better understand, characterize and detect damage caused by impact which is relevant to the aerospace community.

1.3   Chapter Overview

Chapter 2 provides a brief overview of the literature pertaining to impact, damage types, parameters that affect damage, inspection techniques and dent relaxation. **Chapter 3** covers the preparation, fixture design, testing, non-destructive techniques as well as sectioning and microscopy. **Chapter 4** covers the four studies performed: damage as a function of impactor diameter; impact on a repaired versus regular panel; effectiveness of the C-scan tap test for damage characterization; and dent relaxation of a composite sandwich panel. **Chapter 5** summarizes how the study goals were achieved, and discusses areas for further research.

2 Literature Review

This review will cover basic theory regarding impact, as well as research that has been conducted to understand impact of sandwich panels, failure modes of composites, parameters that affect impact resistance, and the base research which prompted the studies described in Chapter 4.

2.1 Low-velocity Impact

Impact events are usually categorized as low-velocity (e.g. tool drop), high-velocity (e.g. hail), ballistic (e.g. small arms fire) or hypervelocity (e.g. space debris). An impact where the response is mass dominated is "low-velocity", although specific velocities are sometimes noted in the literature. This impact category allows for a contact duration that is longer than the time needed for flexural and shear waves to reach the boundaries of the panel [14]. Most of the literature agrees that the structural response (e.g. force-displacement curve, static failure load, ultimate load) and damage incurred for a low-velocity impact event is comparable to a quasi-static indentation [14–17].[1] Low-velocity impact is of particular interest as it can cause damage in composites that can be very difficult to detect which is less of a concern for higher-velocity projectiles as they tend to cause obvious damage or penetrate the panel.

Low-velocity impact on sandwich structures may lead to a large reduction in tensile, compressive, shear and bending strength, and having once exceeded a threshold impact energy level, a panel may be left with having as low as 40% of its initial strength [18]. A reduction of airfoil stiffness as a result of impact damage may lead to problematic aeroelastic phenomenon such as

---

[1]A quasi-static indentation is a slow deflection to a desired impact depth equivalent to a low-velocity impact that would be expected to yield the same damage. The force-displacement history, once smoothed, should be very comparable for the two events. It should be noted that there are some differences in these events, which are well discussed by *Feraboli* and noted by *Lagace* [14, 16].

loss of control effectiveness, divergence, flutter or a state of oscillatory motion leading to fatigue problems [3].

Blunt impact of even relatively low impact energy level can cause significant core damage with minimal surface indentation as seen in Figure 2.1. Residual tensile force of the damaged core keeps the facesheet from rebounding back to its undamaged state [19]. However, if a disbond occurs between the facesheet and the core as a result of the impact event, the facesheet may relax completely obscuring any surface indication of impact having occurred.
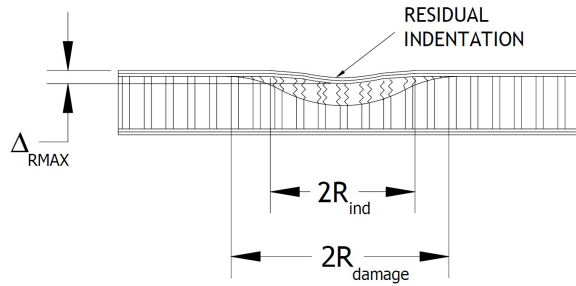
Figure 2.1: Residual indentation caused by blunt impact [20]. Note that the damage diameter ($2R_{damage}$) extends past the residual indentation ($2R_{ind}$).

There are various methods of modeling impact; the spring-mass model, empirical and numerical methods will be touched on, however there are many complex methods of describing impact, which will not be discussed. Due to the variability in the panels and impactors explored in this thesis, any one model would not properly describe all impact scenarios. The energy-balance model will be touched on in Section 2.5.1 as it was used to determine drop height.

2.1.1 Spring-Mass Model

A simplification used in order to simulate the dynamics of an impact event is to treat the projectile-composite collision as a spring-mass model as seen in Figure 2.2 [18], and described by the following dynamic equations. One spring represents stiffness of the structure (k_{bs}) and the other represents the nonlinear membrane stiffness (k_m). M_1 and M_2 represent the mass of the projectile and structure respectively. P is the contact force (a non-linear function of the contact stiffness k_c) as seen in the following equations:

$$M_2\ddot{x}_1 + P = 0 \tag{2.1}$$

9

$$M_1\ddot{x}_2 + k_{bs}x_2 + k_m x_2{}^3 - P = 0 \tag{2.2}$$

When $x_1 < x_2, P = 0$ meaning the projectile is no longer in contact. Assuming geometric nonlinearity and the indentation is negligible, the mass of the structure is ignored as the projectile and structure move in tandem:

$$M_1\ddot{x} + k_{bs}x = 0 \tag{2.3}$$

Utilizing this simplification for the equations of motion, contact duration (τ) can be derived, and can be shown to increase with increasing projectile mass (M_1) and decreasing structure stiffness (k_{bs}):

$$\tau = \pi\sqrt{\left(\frac{M_1}{k_{bs}}\right)} \tag{2.4}$$
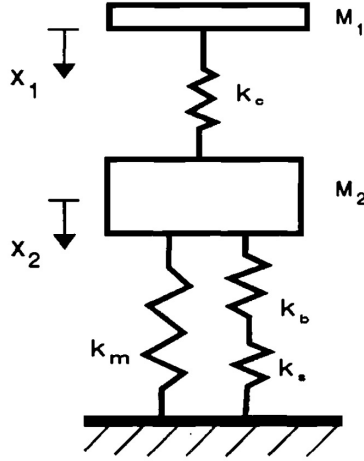
Figure 2.2: Spring-mass model showing the mass of the projectile (M_1), mass of the structure (M_2), non-linear membrane stiffness (k_m) and linear stiffness of the structure (k_{bs}); contact pressure is a function of the contact stiffness (k_c) [18].

This simplification is the basis of utilizing a coin, tap hammer, or the computer-aided tap tester to detect damages (changes in local stiffness) of a structure. Tapping a damaged surface would produce a dull sound as it would have a lower frequency and higher contact time than surrounding undamaged structure.

2.1.2 Empirical and Numerical Methods

Analytical methods typically have difficulty matching experimental results for strength reduction caused by impact; there are many variables that influence an impact event and the damage incurred which will be discussed briefly in Section 2.4 with regard to experimental testing. Empirical methods have had some success for describing stiffness reduction [21]. While not explored in this thesis, *Olsson* proposed an approach for flat sandwich panels that does not rely on empirical indentation laws and that accounts for core crushing, delamination and facesheet deflection [22].

Finite element models have been devised that have good agreement with experiments performed on composite panels comprised of aluminum and *Nomex* cores [23–25]. Some of the numerical models can be very detailed and replicate failure modes accurately, and other provide more general damage details. The downside of these methods is that often coefficients need to be determined through testing, or refinement of numerical models must be made to fit the experimental results. This makes it difficult to extend these models to unique situations, different panel geometries, material types and thicknesses and cannot be modified quickly with a high degree of confidence in the results.

2.2 Certification

A structure being put into service must be evaluated for impact threats that may be encountered over the service lifetime. Concern should especially go towards impacts that may go undetected such as barely-visible impact damage (BVID)[1] and high-energy wide-area blunt impact (HEWABI)[2] which can be caused by collisions of large service vehicles [26]. Impacts from runway debris, tool drops, hail, vehicle collision and any other possible impact event should be considered with the probability of occurrence, ideally determined from damage threat assessments and simulations for various projectiles (e.g. sharp, blunt, small, and large) [8]. As part of a damage tolerant design philosophy, BVID shall not lead to a structural failure at design ultimate load, and non-detectable damages are to be assumed to exist in the structure for certification. Advancing detection capabilities and enhancing our understanding of composite damage caused by impact will allow future structures to be more optimally designed with a lower factor-of-safety due to increased confidence.

---

[1]For visual inspection, BVID is damage that is at the "threshold of reliable detection" [8].

[2]While Category 5 damage such as HEWABI is important to composite certification, it is not explored in this paper.

Figure 2.3 shows the building blocks that are part of any certification effort. If the building block evidence is sufficient and the loading is conservative, certification can be achieved by testing one component test article with a final strength, fatigue and damage tolerance validation [8].
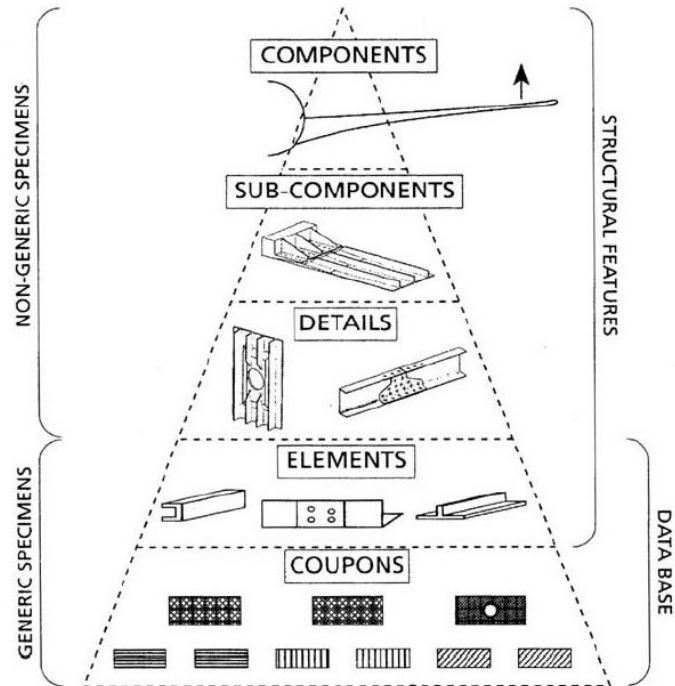
Figure 2.3: Certification building blocks [8]. The panels investigated in this paper are categorized within "non-generic specimens".

To comply with the damage tolerance design philosophy and since there is not a complete understanding of damage characterization, resistance and tolerance in the aviation community, certification of structures utilizing these structural composites require that BVID or manufacturing defects that are not detectable must be able to withstand ultimate load over the aircraft lifetime. Damage exceeding the allowable damage limit must be repaired and should be able to withstand limit load once [20].

Planar damage area appears to be an ideal method of measuring damage, since multiple inspection methods are able to measure damage in this way, and it corresponds well with impact energy level (planer damage area varies linearly with increasing damage [20]); thicker cores and smaller impactor di-

12

ameter lead to less damage area.

Historically as part of the certification process, composites are impacted and their damage (e.g. delamination area, dent depth, etc) would be plotted against incident kinetic energy. Compression-after-impact (CAI) tests show the reduction of compressive strength of the panel, and would be plotted against kinetic energy [14]; this strength is used to determine the panel's damage tolerance, and to determine the margin of safety for an impact damaged panel. CAI testing does not help to characterize damage, failure mode and does not account for panel geometry or curvature. This study is focused on characterizing damage in realistic panel configurations and not interested in predicting residual strength.

2.3 Types of Damage

This section will discuss the various failure modes for sandwich panels as well as how damage initiates and propagates during an impact event.

2.3.1 Failure Modes

Impact on composite panels can lead to various failure modes. For a CFRP laminate with an aluminum honeycomb core, possible failure modes include delamination, matrix cracking, fiber failure, disbond, core fracture and core crushing/buckling. Unless the damage is significant or complete penetration occurs, typically the lower tensile facesheet is left undamaged [18].

Damage from impact initiates in the laminate as matrix cracks, which lead to delamination. Matrix cracks alone do not lead to any significant reduction of strength or stiffness unlike delamination [18]. Matrix cracks form as tensile or shear cracks, as observed in Figure 2.4. Shear cracks form at an angle from the in-plane direction, and in theory initiate at the mid-plane (where the shear stresses would be expected to be highest); in practice and especially for thick laminates, matrix cracking initiates at the first ply where contact stresses are high, which forms a pine tree pattern as seen in Figure 2.5 (a) [18]. Tensile cracks occur where the tensile side of the laminate exceeds the transverse strength of the composite. In a thin laminate, due to large flexure, the cracking may initiate at the tensile side of the laminate and lead to a reversed pine tree pattern, as seen in Figure 2.5 (b) [18].

Delamination occurs between plies that have different fiber orientations; due to each ply being orthotropic, and having varying directions of maximum
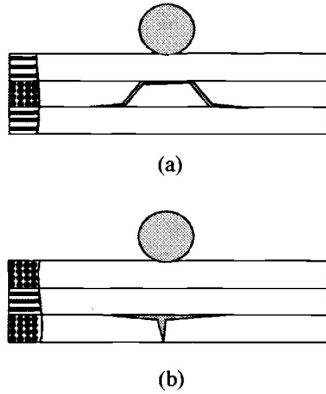
Figure 2.4: Matrix cracks: (a) shear and (b) tensile cracks [18].
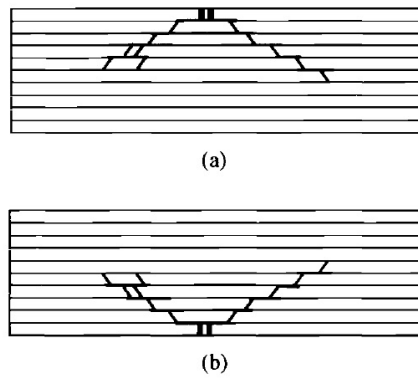
Figure 2.5: Damage patterns: (a) pine tree and (a) reversed pine tree [18].

stiffness, additional stress occurs between adjacent plies of differing angle [18].[1]

The shape of delamination takes a two-lobed peanut shape which follows the major axis of the lower ply as seen in Figure 2.6. Delamination is less likely when the difference in ply angle is minimized between plies [27]. *Bernard* found that damage at the impacted (top) facesheets had the largest delami-

_____

[1]A way to visualize why delamination occurs is to imagine a two plies stacked on top of one another with differing angles between them loaded in three-point bending; if these plies were not bonded together, they would separate when loaded due to their orthotropic material properties. The bonding together of a laminate is acting as a boundary condition, which leads to higher stresses at the locations where higher deflection would be experienced had the plies not been bonded together.

14

nation occurring between the bottom two plies; no damage was observed in the bottom facesheet [28].
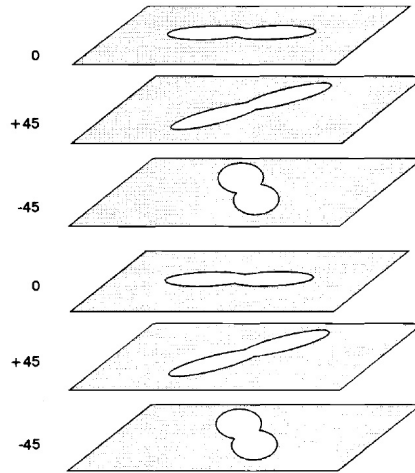
Figure 2.6: Orientation of delaminations in a (0/+45/-45/0/+45/-45) laminate showing typical delamination pattern of the individual plies including the characteristic two-lobed shape [18].

Cell buckling or core crushing tends to be observed in low density core, whereas higher density core exhibits fracture of the cell walls [18]. Cell buckling is commonly observed in the literature for aluminum cores when subject to impact [29]. *Foo* observed that energy absorbed by impact is independent of core density; higher core density led to higher peak loads and smaller damage area in the core and facesheet [30].

Disbonding between the facesheet and core can lead to significant strength reduction of the overall panel. *Southward* found that disbond buckling reduced the load carrying capacity of a sandwich structure up to 64% in four point bending [31].

2.3.2 Damage Initiation and Propagation

Damage in sandwich panels starts typically with delamination of the facesheet; damage area increases linearly with impact energy until a threshold level is reached at which point core crushing progresses and delamination area remains constant [18].

Impact can produce high local shear in the facesheet, leading to delamination; spring-back of the facesheet may lead to further opening up of the delamination, as seen in Figure 2.7 (c) [32].

Impact at the honeycomb core progresses as follows: stress peaks at an initial buckling level, hinges begin to occur one after another in a roughly stable compression stress, the impact loading rebounds linearly and cell walls partially straighten out as seen in Figure 2.8 [32].
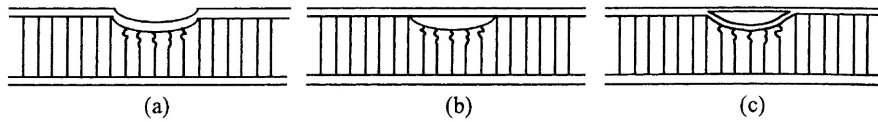
Figure 2.7: Post-impact core damage: (a) dent retains its shape, (b) facesheet rebound leading to hidden damage and disbond, (c) facesheet rebound leading to hidden damage and delamination [32].
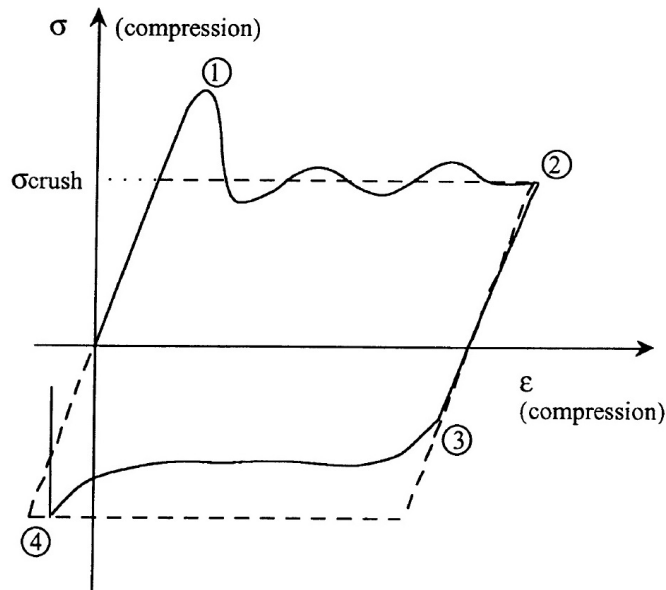
Figure 2.8: Simplified loading of honeycomb: (1) stress peak and initial core buckling; (2) hinges progress through core at a stable compression stress; (3) linear impact unloading; and (4) cell walls partially rebound [32].

16

2.4 Parameters Affecting Damage

Various parameters influence the extent of impact damage for sandwich panels. Material, panel stiffness, characteristics of the projectile, layup of the laminate, curvature of the panel, and boundary conditions all play a role in damage from impact and relate to the extent of strength reduction [21].

2.4.1 Material and Layup

The ability for fibers that make up the laminate to store energy elastically play a large role in the impact resistance of composites. A tougher matrix is more impact resistant than brittle epoxy, and the surface treatment that adheres the fiber to the matrix also plays an important role for impact resistance and residual strength [33]. Tough resin systems are important for laminate damage resistance[1], and therefore beneficial for sandwich structures as well to prevent matrix cracking, which can lead to delamination.

Differences in ply angle between two plies has a significant effect on the amount of damage incurred via impact; this is due to the mismatch in bending stiffnesses at the interface leading to higher interlaminar stresses [33].

2.4.2 Wall Partition Angle and Curvature

Wall partition angle as seen in Figure 2.9 has a large effect on increased energy absorbed by sandwich panels (*Jeon* found that 45 degree wall partition angle led to 25% increased energy absorption, and decreased impact resistance) [34]. Many sandwich panels on aircraft have some degree of wall partition angle, so this should be taken into account at coupon level testing as it will affect the amount of core crushing, damage area and potentially the failure mode mix between the facesheet and the core.

High panel curvature (i.e. small radius as seen in Figure 2.10) will lead to higher peak loads, earlier facesheet fracture (due to the smaller surface area upon impact) and larger planer damage area [35]. Larger damage to the core is associated with a reduction of strength due to alignment of the cell walls in the radial direction (a similar result to increased cell wall partition angle). Blunt impact on a curved panel also leaves less of a residual indentation due to high restorative bending moments in the facesheets when compared to a flat panel [20].

Kistler found that curved laminate panels (not sandwich) led to smaller peak forces, larger peak displacements and contact times [36].

---

[1]Post impact strength increases with resin material Mode I fracture toughness [21].

17
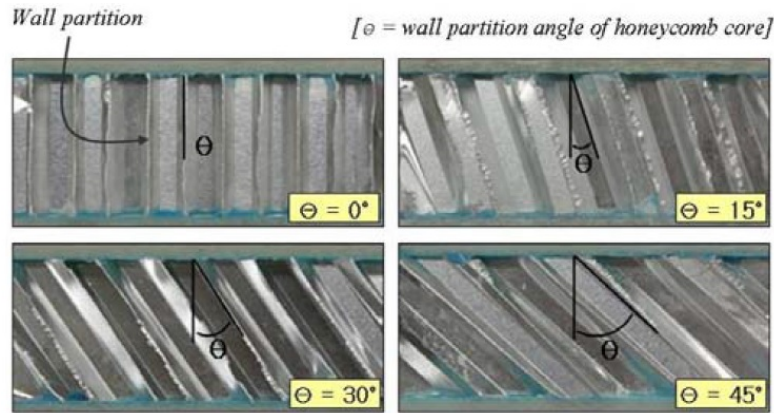
Figure 2.9: Various wall partition angles [34].
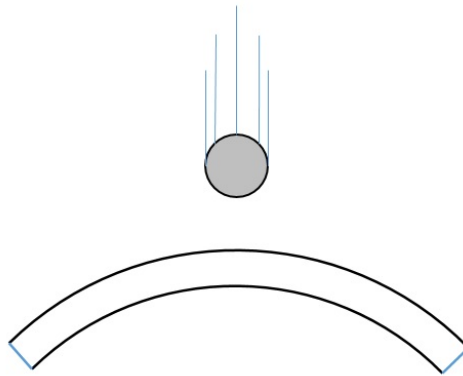
Figure 2.10: Impact of a curved panel.

2.4.3 Boundary Conditions

The boundary conditions for a sandwich panel play a role in the impact event and damage induced. Greater fixity (i.e. fixed versus simply supported) at the ends of a sandwich beam tend to lead to higher peak impactor force for a given energy level [20]; clamped (or fixed) boundary conditions lead to increased peak impact force, decreased displacement and contact duration [36]. The reality for boundary conditions is likely found between a fully-fixed or simply-supported structure or "partial degree of restraint", which may require a detailed analysis or experimental verification to determine the actual degree of restraint [37]. If there is underlying structure, such as a rib underneath

18

the sandwich panel, it would be more appropriate to look at impact on a fixed surface which should lead to greater damage for a given energy level. Knowledge of the overall structure is important for an appropriate idealization of the impact event for experimental or numerical testing. Figure 2.11 shows an idealized situation for impacts on the same panel, at two very different locations; fixtures and testing should attempt to replicate the real boundary conditions of the structure. Impact far enough from supporting structure (e.g. ribs) may be better idealized as being simply supported for the impact event.
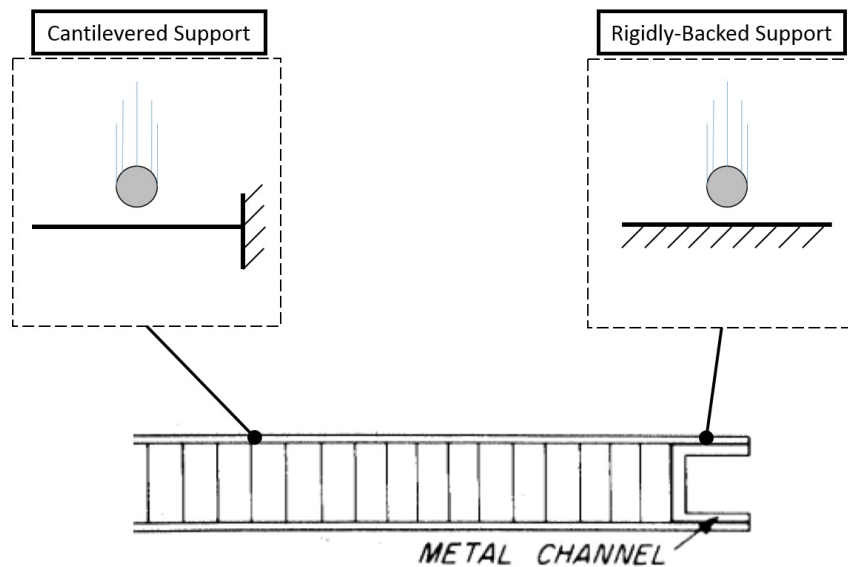
Figure 2.11: Impact on a sandwich panel at two different boundary extremes. Assuming the metal channel is firmly connected to other rigid structure, impact at the far side of the beam when allowed to flex could be idealized as impact at the end of a cantilevered beam, whereas impact on top of the metal channel would have to be idealized as impact on just the facesheet with a rigidly-backed support (modified from [38]).

2.4.4 Non-standardized Panels

Actual aircraft structures and components are composed of various laminate thicknesses (including ramps to different thicknesses, which may lead to residual stresses as well as local anisotropic behaviour), core densities, core splices, varying geometry (e.g. curvature), repairs, and boundary conditions that may

19

not be idealized by typical coupon testing. Testing the complete component and flight testing is part of the certification process which uses evidence provided by coupon testing; studying sections of the final complete components subject to impact may provide insight to the actual failure modes.

Lawrence looked at impacting plastic samples with a high degree of curvature or "irregular profiles". Although more convenient flat coupons could be made out of the same material, the rationale of testing and supporting complex geometries was that residual stresses that are part of the moldings/extrusions may not occur in a flat panel structure, and appear more resistant to impact than it actually is [39]. A similar principle can be applied to non-standardized aircraft panels, and using actual sections of panel takes into account many of the variables that may not exist in an idealized panel such as wall partition angle, curvature, ply ramps, and variations that may occur in the curing and construction of the coupons that may differ from the actual product. The trade-off of using a more realistic panel is that the boundary conditions may vary from the conventional ASTM damage resistance test [40]. Utilizing representative panels may be considered more rigorous from a certification standpoint.

2.5 Damage of Composites

It should be noted that damage resistance is different from damage tolerance. Damage resistance is the ability to incur less damage from an impact or shock event for a given force or energy level, while damage tolerance is the ability of a structure to remain functional, usually for a given applied load [14].[1]

Damage tolerance is an important issue, however this document makes no attempt to directly address fatigue. The focus is on describing and detecting damage, some of which may not be visible on the surface. Visible damage is likely to be noted by the aircrew or servicing personnel, and rectified via a repair, whereas barely or non-visible damage may exist for extended periods of time, perhaps never being addressed within the service life of the composite panel.[2]

---

[1]Damage resistance is important to some areas, like ballistic armour plating, while damage tolerance is of greater interest to an aircraft's ability to continue safe flight (e.g. post impact of a bird or hail) due to damage growth from large static or fatigue loading.

[2]These issues are addressed in aircraft certification, and the structure will be subjected to a multiple of the service life experienced by the actual aircraft; ultimate strength is assessed with various damages strategically placed in locations of high stress. One should feel confident on-board an aircraft, knowing that the structure has been subjected to far more severe loads than are experienced in normal flight.

Based on ASTM D7766/D7766M-11 (Standard Practice for Damage Resistance Testing of Sandwich Constructions) there are three main methods for imparting damage to a panel: quasi-static indentation (rigidly backed panel); quasi-static indentation (edge-supported panel); and drop-weight impact (edge supported panel). An edge supported or rigidly backed panel is usually chosen to best simulate the underlying structure: a rigidly backed support best reflects a sandwich panel with substructure underneath, whereas an edge supported panel would better reflect a structure that is allowed to flex, diverting impact energy into elastic deformation [40].

2.5.1 Drop-weight Impact

A drop weight impact test is a common method of administering impact damage to a material and to test a material's damage resistance [41]. The impact drop tower works by dropping a weight (i.e. the crosshead) from a height to impart a specific impact energy on a specimen below. These devices can range from fully instrumented, to a simple tube approach, whereby a metal bearing is dropped from a specified height guided through a tube. An example tower similar to the one used for this thesis can be seen in Figure 2.12.

Additional weight can be added to the crosshead to change the potential drop energy. The load cell, velocity flag and swappable impactor are all attached to the crosshead. The guide rail ensures the crosshead remains on a vertical trajectory during the drop, and a rebound catch mechanism prevents multiple impacts by catching the crosshead following initial impact. A double-prong flag is attached to the crosshead and when the flag passes the photoelectric-diode of the velocity detector the time between the leading edges of the prongs is provided; this information is necessary for calculations such as specimen displacement, velocity and impact-energy [41]. A solid base plate is used to affix an impact support fixture. Once an impactor is selected, the composite plate or panel is centered beneath the impactor and clamped into place. The latch mechanism is used to position the crosshead at the correct height to achieve the desired impact energy level and a trigger is pulled to initiate the drop of the crosshead.

2.5.2 Force-Time Curve

The impact tower used for this thesis had a load cell to monitor the force over time. In order to measure the contact force over time, the force between the two masses is measured on either side of the load cell, the main mass of the crosshead and the mass of the impactor. In order to avoid load cell errors due
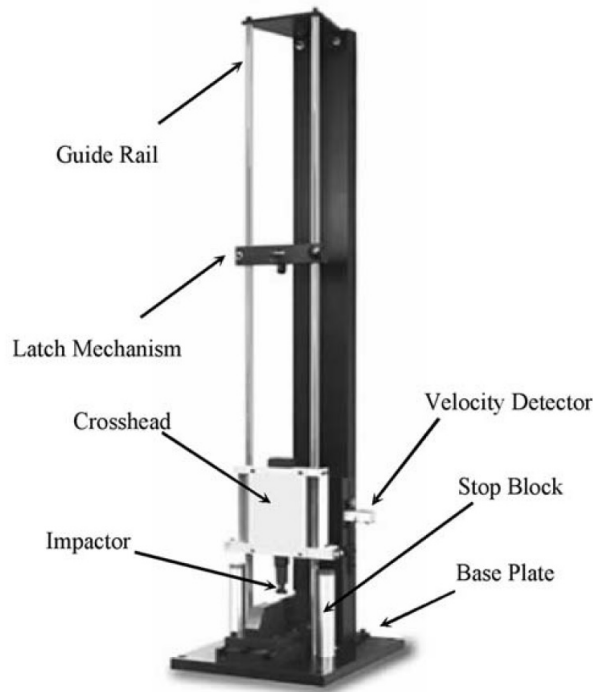
Figure 2.12: Example impact tower [41].

to mass dynamics (i.e. vibration of the impactor against the load cell), the impactor mass should be much smaller than the main mass.

There are characteristic points along a force time diagram that reveal properties of the impact event. Figure 2.13 shows a representative force versus time plot for a drop-weight impact event. Within the force-time data collected, there are many oscillations. These are due to the natural frequency of the impactor, as well as the flexural vibrations of the panel [41]. Other vibrations may be due to the relationship between the weight below and above the impactor. Typically, it is preferable to have 95% or more of the weight above the load cell, which reduces this effect [14, 42].

Figure 2.13 shows F_{max}, F_1 and the duration of the impact event. F_{max} is the peak force during an impact test and the point at which the impactor begins to rebound from the panel (i.e. velocity is zero). F_1 is the critical force which notes once there has been a change in out-of-plane stiffness, usually considered the damage threshold. While F_1 may indicate that the panel has begun to yield or locally fail, lack of this characteristic change in stiffness

22

does not guarantee that damage has not occurred. The change in stiffness can be difficult to detect due to the oscillations in the signal, so the comparisons in later chapters will look at smoothed data in order to aid in identifying the force at which the change in stiffness occurs, and to get a better determination of when the peak load has been achieved. Typically force time curves are smoothed as the mass differences between the impactor and the target panel can lead to inertial and harmonic oscillations causing signal noise [14]. Impact at energy levels above and below the critical force or energy level are known as supercritical and subcritical respectively [14]. The contact duration is related to the stiffness of the structure, as noted earlier in Section 2.1.1.
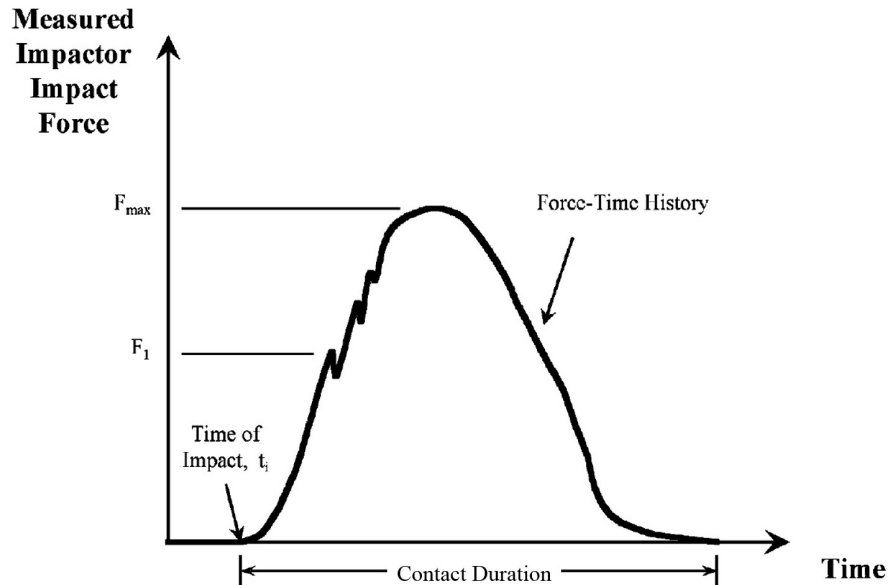
Figure 2.13: Representative impact force time history (modified from [41]).

2.5.3   Impact Energy

Impact energy is best determined from the kinetic energy at the time the impactor contacts the specimen; this is estimated as the potential energy when the crosshead is positioned above the specimen prior to initiating the drop. The potential energy equation can provide a good approximation of impact energy by measuring the mass of the crosshead, load cell and impactor (m), as well as the distance from the tip of the impactor and the specimen:

$$E_P \;=\; mgh \tag{2.5}$$

where m is mass, g acceleration due to gravity and h is the drop-height. There are some energy losses (e.g. friction between the crosshead and the rails) during the drop that reduce this theoretical value to the actual impact energy. The exact impact energy after any losses can be calculated using the velocity of the crosshead just before impact [42]:

$$Impact Energy = \frac{1}{2}mV_o^2 \tag{2.6}$$

where V_o is the velocity at time of impact. Following impact some of the energy is absorbed. Dissipated energy is the energy mainly absorbed by the test frame, as well as from vibrations, friction, and specimen or fixture slippage [14]. When the impactor contacts the specimen, the kinetic energy is reduced by the total energy dissipated (E_D), which is made up of the inertial contribution (E_I), the vibration (and other non-conservative phenomenon, E_V) as well as the total energy that creates damage or absorbed energy (E_{DD}) [14]:

$$E_D = E_I + E_V + E_{DD} \tag{2.7}$$

E_{DD} can be determined by first performing a non-damaging elastic impact [14].[1]

2.6 Non-destructive Inspection

Various methods are used to detect damage, however certain methods are more applicable for characterizing impact damage. Figure 2.14 shows external and internal damages for drop-weight impact.

Table 2.1 shows common inspection methods for damage detection and evaluation. Other considerations when deciding on an non-destructive inspection (NDI) method are its availability, credibility[2], the equipment operating and procurement cost, speed of the inspection method and expertise required; there is often a compromise between the inspection method sensitivity and

---

[1]The inertial and vibration parts of energy were not determined in this thesis due to practical limitations of the drop-tower. Since characterizing the damage was the primary goal, multiple impacts were avoided since some damage may occur at even very low energy levels for sandwich panels.

[2]If the method is certified, academically recognized, and commonly used in industry this makes it credible as a technique.
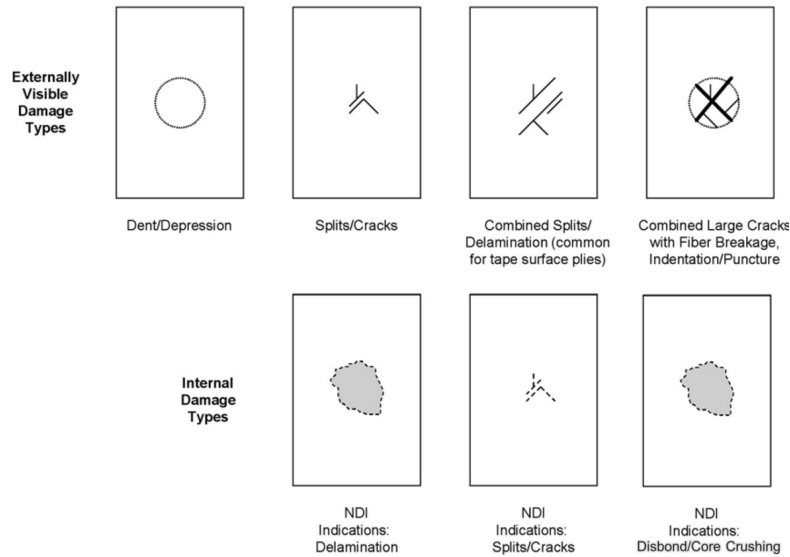
Figure 2.14: Example of commonly observed damage modes from drop-weight impact (modified from [41].)

speed, as seen in Figure 2.15. Using multiple methods can be complimentary, especially when the extent and type of the damage is unknown.[1]

2.6.1   Visual

Visual inspection is typically fast and requires limited expertise and cost. Use of visual aids (e.g. borescope, flashlight) can be employed [44], and areas of suspect damage can be measured via caliper or micrometer and compared against repair manual limitations. Visual inspection can be broad to detect large, obvious defects (e.g. aircrew walk-around before flight) or detailed (e.g. looking at individual parts under magnification) which will occur if a broad inspection indicates possible damage. Visual inspection will not find internal flaws, and may not detect small surface cracks or delaminations [43].

---

[1]This is not a comprehensive list of NDI methods; other techniques exist, however these are some of the most common for composite sandwich panels. Laser topography was employed as a relatively novel technique for external damage characterization explored in Chapter 4. For general inspection other defect detection capabilities (e.g. water ingress, corrosion, etc) may be required. Speed, portability and complexity are considerations when selecting an inspection method.

Table 2.1: Inspection methods for characterization of impact damage.

Type of damage	Inspection method					
	Visual	Tap testing	Thermography	Shearography	Ultrasonic	Radiography
External	●			○		○
-Dent depth	○					
-Dent diameter	○					
-Cracked facesheet	○					○
Internal	○[1]	●	●	●	●	●
-Damage area		○[2]	○		●	○
-Damage depth					○[3]	
-Delamination		○	○	○	○	○
-Disbond		○	○	○	○	
-Crushed core		○	○		○	○

Note 1 – Internal damage can be characterized via microscopy upon destructive sectioning of the specimen.
Note 2 – Damage area can be determined by using grid and quantifying the change in local stiffness over the area.
Note 3 – Pulse-echo ultrasound can detect damage depth, however this may be limited to the facesheet.

Legend
● Inspection method is appropriate.
○ Inspection method may have limited ability to detect damage or cannot distinguish between damage types.
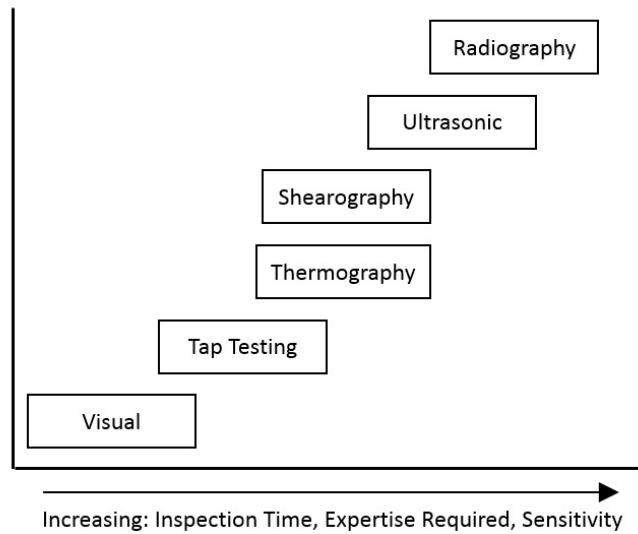
Figure 2.15: Increasing inspection duration and expertise for greater NDI sensitivity (modified from [43]).

2.6.2   Tap Testing

Taping a composite structure with a coin and listening for a reduction in sound is a qualitative method of checking laminates for damage [45]. The tap testing technique utilizes frequencies that are detectable by the human ear in order to detect delamination or disbond in composites [43]; one of the ways the energy from the tap is dissipated is through audible sound due to facesheet vibration compressing and expanding the air. A coin or lightweight tap hammer can be used which will produce a sharp sound for a solid structure, whereas a dull sound will be produced when the underlying bonding has been damaged; the sound should be compared from adjacent locations on the panel to look for inconsistencies.

The woodpecker is another tapping hand-held NDI tool that uses a solenoid for tapping and measures impact duration for detecting damages in a composite. Various other specialized tap hammers (some digital) have been developed all based on either the user listening for a dull tone, or the instrument measures the contact time which reflects a loss of local stiffness caused by impact [46]. These tools also work in the opposite sense: regions of higher stiffness are also noted through a sharper tone or shorter contact time. This would identify internal structures such as ribs, core splices, higher density core and thicker laminate facesheets.

The Computer-Aided Tap Tester (CATT) is a tap test method that uses a magnetic cart for repeated tapping over a gridded surface, which can be seen in Figure 2.16. The cart uses an accelerometer which feeds a voltage to a computer, which then produces a 2-D colour plot of the contact time which is directly related to the local stiffness. This method is much improved over the audible tap tests since it provides recordable, quantifiable information and can be used to size the extent of the damage. The older method of tap testing is subjective, less sensitive and based on the experience of the operator.

The CATT produces a C-scan image[1] which is able to provide internal details such as core splices, changes in core density and damages as a result of impact similar to a through-transmission ultrasonic C-scan.

---

[1]A C-scan is a planform view created by mapping a scan over a 2-D surface, where signal discontinuities (e.g. damages, defects and internal structure) from a set threshold or gate are often represented by colour-coding [48]. This method is appropriate for determining damage area or diameter. The other methods of data presentation are the A-scan and B-scan. The A-scan displays signal strength as a function of time, which can then be used to determine the approximate depth of damage or a defect in the structure at a single location. The B-scan provides a cross-section view by plotting time-of-flight information on the y-axis and the position of the transducer on the x-axis [49].
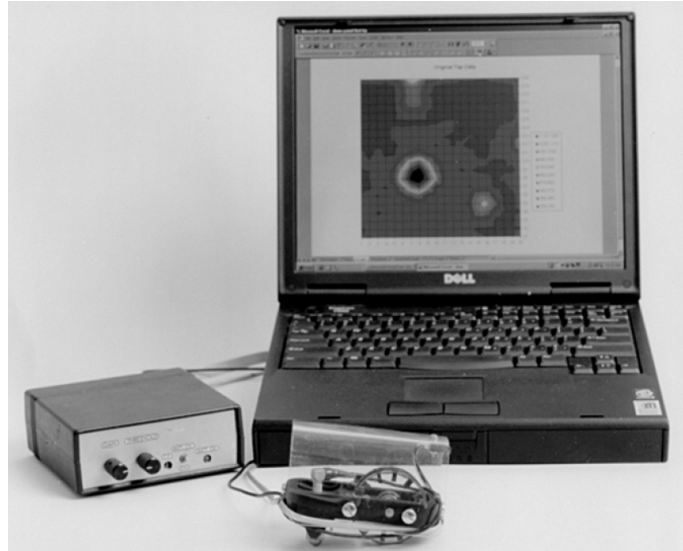
Figure 2.16: The CATT system, showing the magnetic cart, electric circuitry for processing the signal and computer software to display and analyze the C-scan image [47].

Hsu tested the CATT on a retired B747 trailing edge flap (GFRP and fiberglass honeycomb core), which had three impact damages, which were all detected, including the 1 inch steel 2.9 J low-velocity impact. If the contact time is measured, the tap can be modeled as a mass (tap hammer tip, m) contacting the ground with a stiffness of k [46].[1] Figure 2.17 shows an example of a regular and damaged structure, and the differences regarding local spring stiffness (k) and the corresponding signal yielding changes in contact time.

$$\tau = \pi\sqrt{\frac{m}{k}} \tag{2.8}$$

Within a reasonable range of tap force and mass (where additional damage is not incurred for the panel) contact time is a function of stiffness, and variations in the force application has minimal effect on contact time. *Hsu* shows that the square of the contact time varies linearly with tapper mass, and that for a variety of operators, the stiffness was within a variation of $\pm 4\%$ [46]. Furthermore, derived stiffness via the tap method leads to comparable results to mechanically measured stiffness [45].

---

[1]It should be noted that this is the same way an elastic low velocity impact can be modeled.
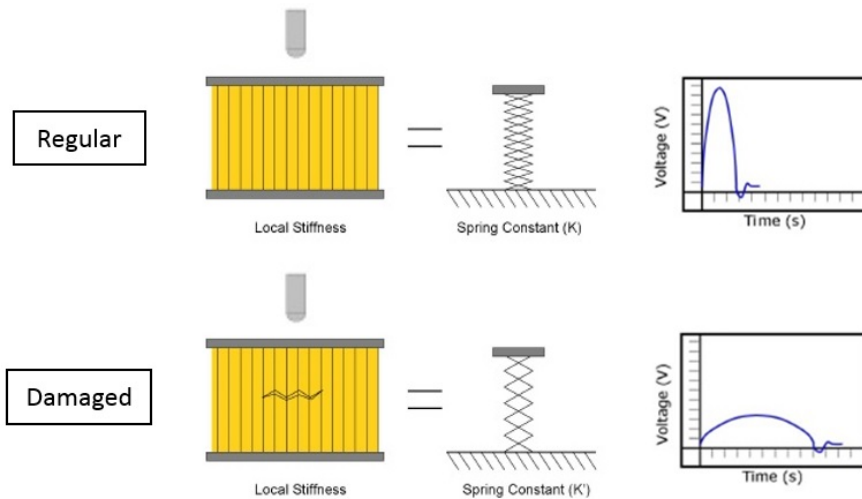
Figure 2.17: Flaw in a sandwich structure is equivalent to a softer grounded spring, which produces a longer contact duration when compared to the undamaged structure (modified from [50]).

The CATT has been used to detect helicopter rotor blade disbonds, to verify the quality of repairs on helicopter blades, as well as boat hulls and various other academic applications [45, 51].

Measuring contact time is a simple and cost effective way to map impact damages and the relationship of tapping and contact time was explored by *Kenner* to detect defects [52]; contact time has been noted to be consistent even with varying peak impact force [46]. *Hsu* characterized damage using the CATT and air-coupled ultrasonic testing. The CATT and air-coupled ultrasound effectively mapped internal features of a composite repair [53]. A disadvantages of tap testing is that damage detection decreases with increasing facesheet thickness [20].

2.6.3 Thermography

Thermography works by observing a heated structure which is made possible by differences in material thermal conductivities by creating a temperature gradient. Two main categories for thermography are recognized: passive and active [54]. Passive thermography uses a infra-red camera to observe the response of a structure to an applied heating (using heating lamps or pads directly heating the structure) or cooling. The heat source can be placed on

29

either the camera side (pulse-echo) or on the opposite side of the structure being inspected (through-transmission) [55]. The pulse-echo method is better at detecting surface damages whereas the through-transmission method better detects deep damages [55]. Active thermography induces heat in the structure via applied cyclic loading or vibration [55]. Thermography is able to detect impact damage such as delaminations and disbonds in sandwich panels [56].

2.6.4 Shearography

Shearography uses a laser light to detect defects from variations in reflected light on a structure's surface.[1] An original image of the lit surface is compared against the image of the stressed structure from heating, pressure or vibrations which shifts the surface contour revealing disbonds or delaminations [43].

2.6.5 Ultrasonic

Ultrasonic inspection is a very common method of detecting damage, utilizing high frequencies in the MHz range [43]. Two main types of ultrasound exist: through-transmission and pulse echo. The setup for through transmission ultrasound can be seen in Figure 2.18. Pulsed high voltage is sent to a transducer, which converts the pulses into ultrasonic waves which propagate through the couplant (often water) to the panel [43]. The receiving transducer converts the ultrasonic waves back into an electrical signal. If there is a damage to the core of a sandwich panel or a disbond, the ultrasonic pulses will lose energy at these locations and the difference from the remainder of the panel is detectable. Ultrasound provides a clear coloured depiction of damage area for voids, delamination, crushed core and any other discontinuities that may affect the signal. Through-transmission may not be effective at characterizing laminate damages, and does not aid the inspector in determining the depth of the defect or damage.[2] Damage in the core may conceal laminate damage as this has a greater effect on ultrasonic wave propagation.

Pulse echo ultrasound allows for inspection from only one side of the component, and works by transmitting and then "listening" for the return of the pulsed-signal that reflects off of surfaces and discontinuities in the material [43, 44]. It can provide details such as depth of damage, however for

---

[1]This technique is similar to holography; both are a interferometric technique that utilize coherent light. Holography requires the interference of two light sources, and it is more sensitive to vibrations when compared to shearography, however holography is more sensitive [57].

[2]For example if a disbond it noted, it will not be possible to determine which side of a sandwich panel the disbond is located using this method.
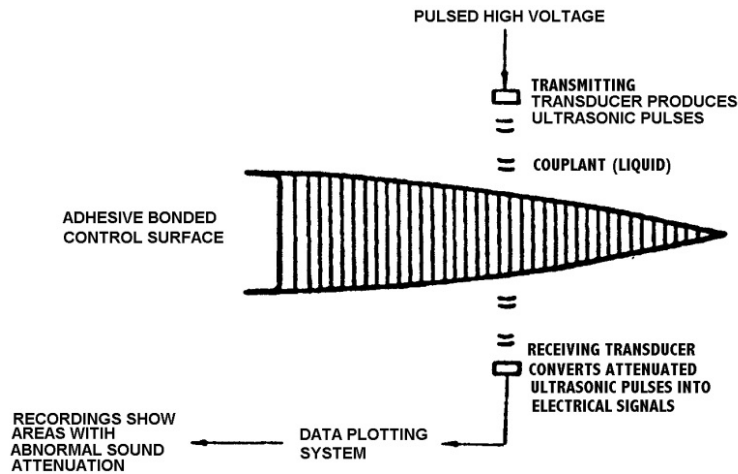
Figure 2.18: Through transmission ultrasound [43].

a sandwich panel it will have difficulty detecting damages that are past the laminate bondline due to significant changes in density [44].

Garnier found that when comparing the effectiveness of detecting various defect types in composites, ultrasonic pulse/echo was the only method that could determine defect depth, whereas infrared thermography and shearography produced more rapid inspection results [58].

2.6.6 Radiography

Radiography (X-ray) provides a detailed image of the interior of a part, however it can be relatively expensive, requires operating expertise from the NDI-technician[1] and caution needs to be used due to the radiation hazard [44]. X-ray can effectively detect water ingress in the core, and can detect core that is damaged (e.g. such as a blown or crushed core) for sandwich panels.

2.6.7 Mechanical Impedance Analysis

Another common NDI method for composite honeycomb structures is Mechanical Impedance Analysis (MIA), which is typically one of the modes of an ultrasonic bond tester. MIA uses a duel-element probe to send continuous low-frequency acoustic waves that cause mechanical movement of the struc-

---

[1]Honeycomb X-ray radiographs require experienced technicians for review [43].

ture [59]. The difference between the induced and received waves is measured, which can be related to the underlying stiffness of the structure; this method is well-suited to detect delaminations [50]. Other bond tester modes such as the pitch-catch mode can be used on honeycomb sandwich panels to detect disbonds by transmitting acoustic energy to the part (pitch) and detecting the acoustic energy with the receiver probe (catch) [59]. An intact bond-line will attenuate some of the acoustic energy, whereas a disbond will increase the energy captured by the receiver probe [59].

2.7 Impactor Diameter

The shape and diameter of the impactor plays a significant role in the damage incurred on a sandwich panel.

Projectile diameter has a more significant influence on maximum damage area than impact energy [28] and impact force required to initiate damage varies with impactor diameter for glass-fibre reinforced epoxy [60]. Damage initiates at lower impact energy levels with smaller impactor diameters [61]. Blunt impactors produced larger damage areas, higher contact loads and delamination, whereas sharper impactors lead to fibre breakage, localized damage, increased contact time and greater indentation depth for composite laminates [62].

Increasing impactor diameter leads to larger damage area [63].[1] *Tomblin* noted that planar damage size for sandwich panels was a better indicator of strength degradation than indentation depth or "BVID" and blunt impact can lead to greater strength reduction than a punctured skin [64].

2.8 Sandwich Panel Repairs

The goal of repairing a sandwich structure is to return the part to the same fit, form and function of the original structure. This means the performance of the part, as well as the strength and stiffness of the panel must be restored (e.g. facesheet loads must be redistributed through the bonded patch) [38].

Once damage has been detected on a panel and assessed to meet repairable criteria[2] the damaged core and facesheets are cut out to prevent any damage

---

[1]This assumes that all other parameters remain consistant, such as the facing thickness, boundary conditions and impact energy level.

[2]Assuming the panel is an aerospace part, this information is likely outlined in the aircraft's structural repair manual.

growth. Figure 2.19 shows a typical repair where the core insert, adhesive(s), and external patch are cured in place.
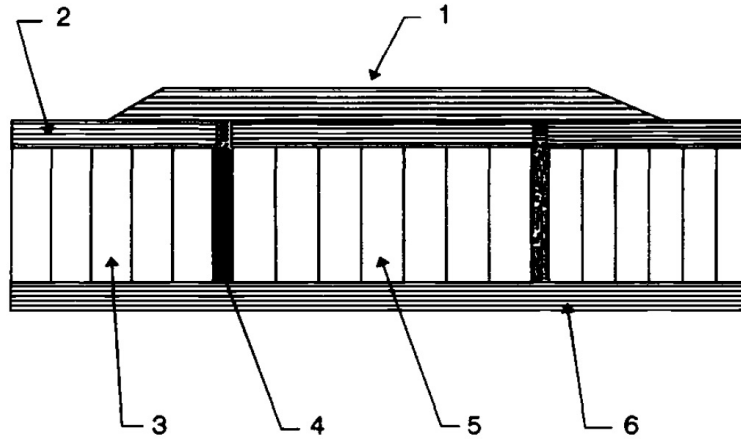
Figure 2.19: Bonded repair on sandwich structure (1: external patch; 2: skin; 3: core; 4: adhesive; 5: core insert; 6: lower skin) [18].

2.8.1 Thick Laminate comparison to a Repair Patch

A repair's task of restoring the ultimate design strength of the panel and arresting damage is assumed (since its out-of-plane stiffness and strength are higher) to also restore, or even strengthen a panel's impact capabilities. A repair patch's impact properties will be compared here simply as a location of thicker laminate.

Thicker laminates tend to be more impact resistant than thin laminates [38, 60] however *Rhodes* noted that additional thickness does not improve impact resistance for sandwich structures, but increasing the core crushing strength does [65]. *Park* noted that reduced facesheet stiffness led to the core thickness having a greater effect on impact resistance [66]. *Kistler* found that thicker laminates had shorter contact time, lower center displacement and a higher peak impact force [36].

A repair patch that adds significant thickness to the laminate should share properties of thick laminates and similar failure modes such as the characteristic pine tree pattern as seen in Figure 2.5 earlier.

2.9   Dent Relaxation

Short term dent relaxation is noted by *Minakuchi* with a foam core sandwich structure. Relaxation appears to take place rapidly over the first five minutes (0.95 mm in the experiment), showing relaxation rate decreases over time [67]. Figure 2.20 shows how the relaxation begins after the elastic unloading of the impactor, at which point the crushed core begins to stretch; the core resists the facesheet relaxation forces attempting to bring the surface to an non-dented state. The equilibrium position between the core and the facesheet leaves the residual dent. Additional failure due to these residual tensile stresses may occur such as disbonding and delamination. A disbond or delamination would allow the facesheet to further relax as seen in Figure 2.7, relieving residual stresses caused by the impact and concealing the underlying damage.
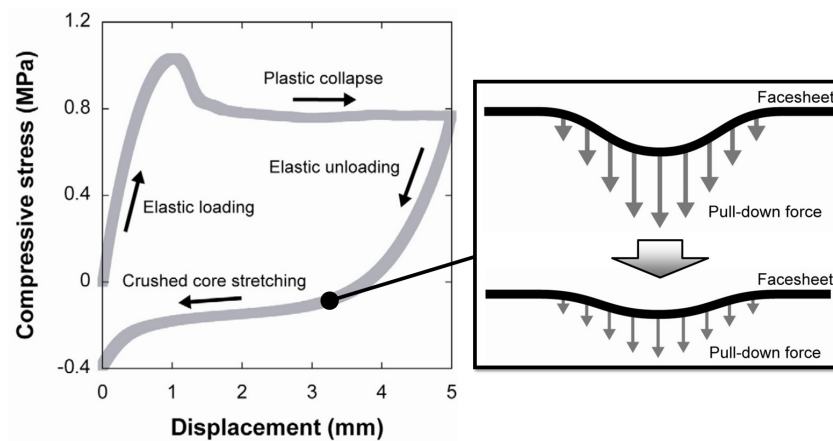
Figure 2.20: Loading, unloading and residual stress of crushed core causing dent relaxation [67].

Long term relaxation (i.e. measured after six months) after impact for Nomex core sandwich structure has been noted by *Ruzek* [68]. This relaxation rate likely depends on many factors, especially the material make-up of the facesheet and core. Relaxation may increase when a dented panel continues to be loaded; this relaxation rate should be considered when certifying a sandwich structure for damages that may go undetected.[1]

---

[1]For example, a hail impact may occur in flight and by the time the aircraft gets inspected on the ground the typical flight loading may further conceal any damage that was present immediately following impact. If the impact was small enough, the damage may go unnoticed over an extended period of time, making visual detection very difficult.

3   Experimental Method

3.1   Overview

The panels used for testing were from an aircraft horizontal stabilizer that had exceeded its useful service life and was sectioned as part of a previous weighting survey. The composite panels are sandwich construction, consisting of carbon fibre reinforced plastic (CFRP) facings adhesively bonded to an aluminum honeycomb core.

The facings were made up of continuous AS4 carbon filaments and 3501-6 structural epoxy matrix. The core was 5056-H39 aluminum alloy bonded to the facings with FM-300 film adhesive (see Appendix A for data sheets). The thickness of the facings varied from $0.66 - 3.18\ mm$, core density varied from $2.3 - 5.3$ pounds per cubic foot (pcf) and the core thickness varied from $3 - 66\ mm$ amongst the panels characterized. Density of the core, and core ribbon direction varied from panel to panel. All panels were symmetrical about the mid-plane. FM-404 foaming adhesive was used within some of the panels to bond separate sections of core.[1] An example of a generic panel layup is presented in Figure 3.1.

Laminate layups consist of 0, 45, -45, and 90 degree possible ply orientations, and constructed in order to create a symmetric laminate on both the upper and lower facings.

Figure 3.2 shows a cross-section of a sample panel, with the materials that make up the sandwich panels annotated. Material properties are detailed in Appendix A.

---

[1]Core densities and ribbon directions change within the overall structure, a design optimization to provide shear strength where it is most required. Core splices would be required regardless, since honeycomb core is ordered in specific sheet sizes then cut to the shape necessary.

AS4/3501-6 CFRP (+45/-45/90/+45/-45)
FM-300 film adhesive
5056-H39 aluminum alloy honeycomb core
FM-300 film adhesive
AS4/3501-6 CFRP (+45/-45/90/+45/-45)
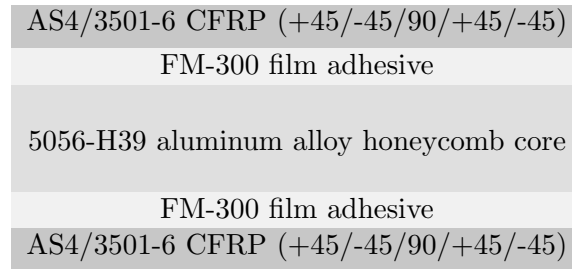
Figure 3.1: Panel layup illustration.
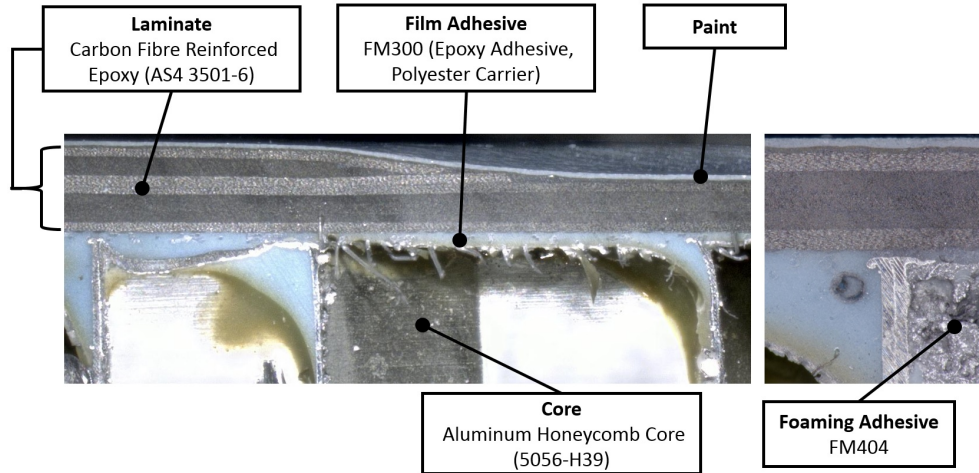
Figure 3.2: Sandwich panel cross-section with the facesheet, core and adhesive materials detailed.

3.2 Preparation and Impact Testing

This section details the the process leading up to impact of the panels, namely panel selection, preparation, pre-impact inspection of panels, fixture design as well as the drop tower setup and impact.

3.2.1 Panel Selection

Seven panels were selected to satisfy four primary objectives: a comparison of damage and damage detectability caused by hemispherical impactors of varying diameter; damage and damage detectability of impact on a repaired panel versus a regular panel; effectiveness of the C-scan tap test (a custom version of the "Computer-Aided Tap Test") when compared to ultrasound and radiography; and measurement of dent relaxation using laser topography.

The first panel B11 was selected for its consistent facing thickness of five plies and consistent core density of 2.3 pcf. This panel can be seen in Figure 3.3. Panel B14 was selected to confirm repeatability of B11. Panel E3R with a repair and an otherwise identical panel E3 without a repair were selected for the second study. Panels D21 and F3 were additionally selected to determine the robustness of the C-scan tap test NDI method due to their different core densities, core splices and facing thickness. Panel B12 was chosen for the dent relaxation study because of its consistent facing thickness.
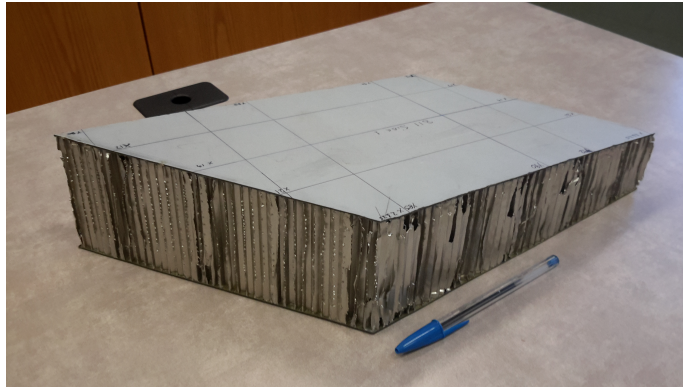
Figure 3.3: Panel B11 for impactor size study.

3.2.2 Panel Preparation

Once the panels had been selected, the exposed core and edges were covered with aluminum tape in order to prevent any water from penetrating the panels during through-transmission ultrasound.

Figure 3.4 shows round pieces of lead tape were applied to the facing near the edges. This served two purposes: it provided a location for comparison and mapping of NDI methods; second, this provided a reference for multiple scans using laser topography. The circular tape locations were used to produce the laser topography deviation map between the undamaged and damaged panels before and after impact.
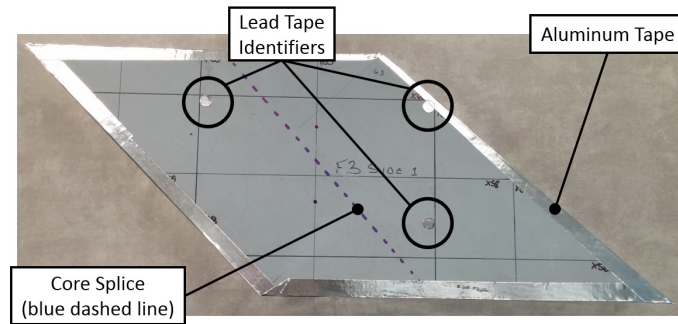
Figure 3.4: Lead tape identifiers and aluminum tape applied to panel.

Locations for impact were marked based on order of impact. Considerations for impact location were edge distance (so that the panel would sit properly in the fixture), distance from areas of interest (e.g. core splice) and other surrounding impact locations. Figure 3.5 shows the impact locations with impactor code and energy level for panel B11.

Core splices were marked on the surface approximately where they were located (identified by observing foaming adhesive at the exposed ends of the panels).

3.2.3 Pre-inspection of Panels

Panels were scanned using both laser topography and ultrasound prior to impact. The laser topography scan allowed for detection of any surface irregularities, and provided the data required to create a post-impact deviation map showing a precise 3-D profile of the impact dent. Ultrasound helped to identify if there were any existing damages such as disbonds or core crushing present within the panel.
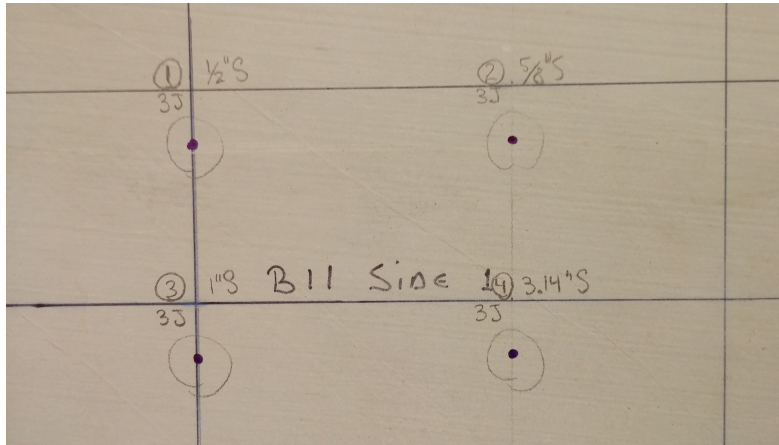
Figure 3.5: Impact order, noted with impactor code and desired energy level.

3.2.4 Drop Tower and Impact

The drop tower used for this study is a product of *Dynatup* (acquired by *Instron* in 1997). This drop-tower has a double column impactor guide mechanism, consisting of guide rails, latch mechanism, crosshead, load cell, rebound catch mechanism, velocity flag/detector, stop block, and swappable impactor as seen in Figure 3.6. The software used with the drop tower is Dynatup Impulse Impact Data Acquisition Version 3.4.59, which measures the force using the load cell, time and velocity using the velocity detector, and extrapolates displacement and energy for the impact event. The load cell capacity was 5000 lb_f.

By knowing the weight of the impactor, load cell, crosshead, attachment and bolt, the height can be determined and set based on the desired impact energy level. By applying $E_p = mgh$, one can determine the necessary drop height. The height was adjusted via a rough motorized control, and final height was ensured using a ruler. The error was considered acceptable when the impactor was within 3 mm of the drop height to achieve the required impact energy level.

The impact location was aligned using a plastic jig that ensured the impactor would strike the surface of the panel at the correct location as seen in Figure 3.7. The panel was secured in place by rotating the jack counterclockwise until hand tight; tooling was not used to prevent excessive compression or pre-load on the panel.

Moving the crosshead and impactor to the surface of the panel, the rebound
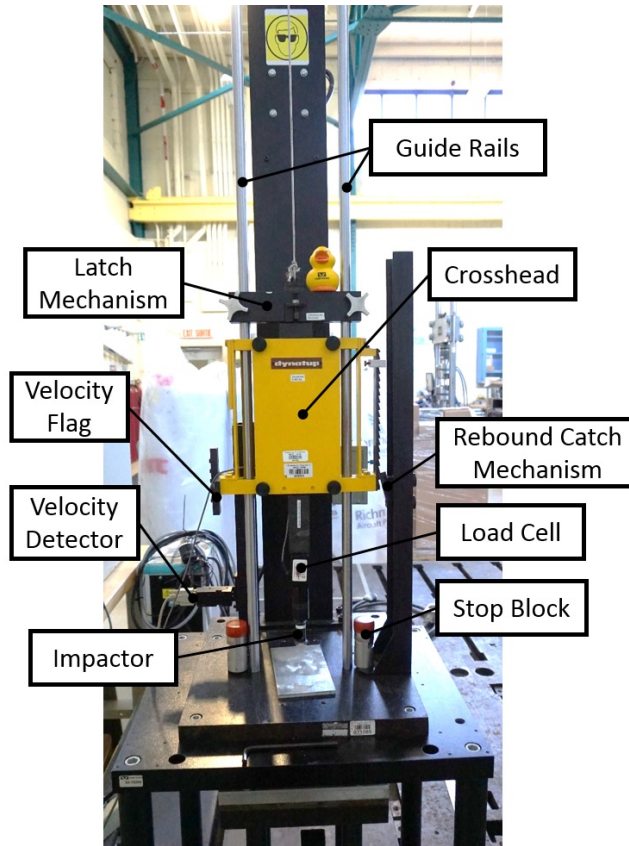
Figure 3.6: Drop weight impact tower components.

catch was adjusted and secured in place. The velocity detector was then adjusted so that at the bottom of the drop the velocity flag attached to the crosshead had just passed the detector (ensuring that the final velocity was recorded prior to impact). The stop blocks are adjusted so that the fixture and drop tower would not be damaged in the unlikely event the impactor pierced the panels.

Once everything was secured in place, and the program was running, the tab at the top of the crosshead would be pulled causing the impactor/crosshead assembly to drop and impact the panel. The computer determines when an impact has occurred from the data provided from the velocity detector and load cell, and plots the force-time information. A combination of the velocity and mass data in the program, along with the recorded force-time data, is used to extrapolate energy at peak force, energy absorbed, deformation at

41

peak force, velocity, and total impact time. The impact process was repeated for all identified zones on the panel.
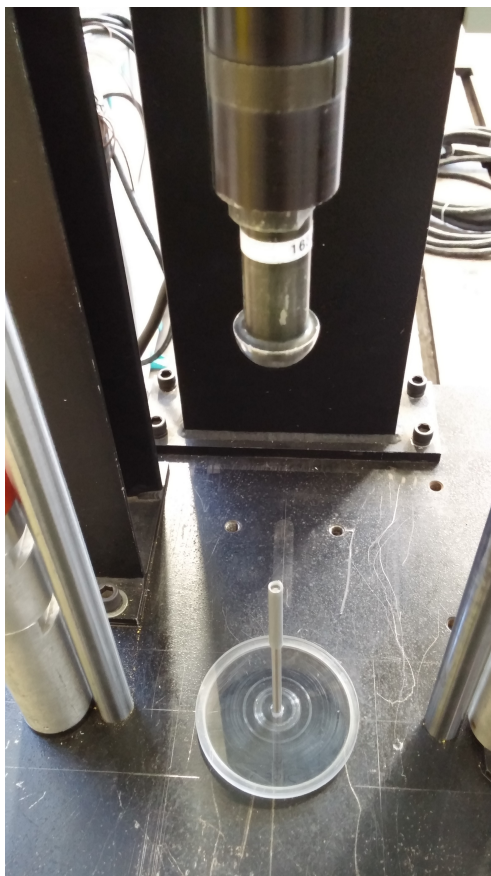
Figure 3.7: Aligning impactor with location on specimen using jig.

3.2.5 Impact Fixture

A fixture was needed to provide the desired support for the various panels during impact, however a standard ASTM test setup could not be used because it could not accommodate specimens of varying shapes and sizes. Furthermore, it was desired to impact perpendicular to the upper facesheet to ensure that the force data recorded from the drop-tower load cell would be accurate; panels would sit flat on the ASTM fixture which would lead to oblique impact of the upper facesheet.

The fixture design incorporates a *Simplex* 12 ton $1\frac{1}{2}$ x .12, 16 inch high leveling jack (a.k.a. screw bell jack) which was modified to act as a variable geometry support surface. The screw jack could be rotated to move upwards and downwards to accommodate varying panel thicknesses. An aluminum platen replaced the original swivel piece, allowing for a 7 inch diameter flat surface or an attachable ring type support.[1] This aluminum contact ring is what was used for all drop tower tests, in order to provide a more realistic boundary condition allowing the panel to flex naturally during impact (drawings of the fixture provided in Appendix B). The entire platen could swivel and rotate, to a maximum of 15 degrees from the horizontal plane to accommodate taper.

A screw jack retainer piece, which fixed the bottom of the jack, ensured that the jack remained centered with the circular cutout of the drop tower where the impactor passes through, and prevented the jack from sliding during the impact event.

Eight polyurethane adhesive rubber bumpers were placed five inches apart above the fixture, equally spaced in a circle to provide a flexible upper boundary condition, and prevent the panels from being constrained from above. The contact surfaces are shown in Figure 3.8.

The specialized fixture setup in the drop-tower is shown in Figure 3.9. The setup allows for the impact to occur perpendicular to the upper facing, while minimizing any stresses caused by overly restricting the panel. It also allows for swapping of panels with relative ease, and impacting a specific location on the panel accurately.

---

[1]This support was designed to have a unsupported region similar to ASTM test method D6264 for a quasi-static indentation while still being adaptable for various sandwich panel geometries [69].
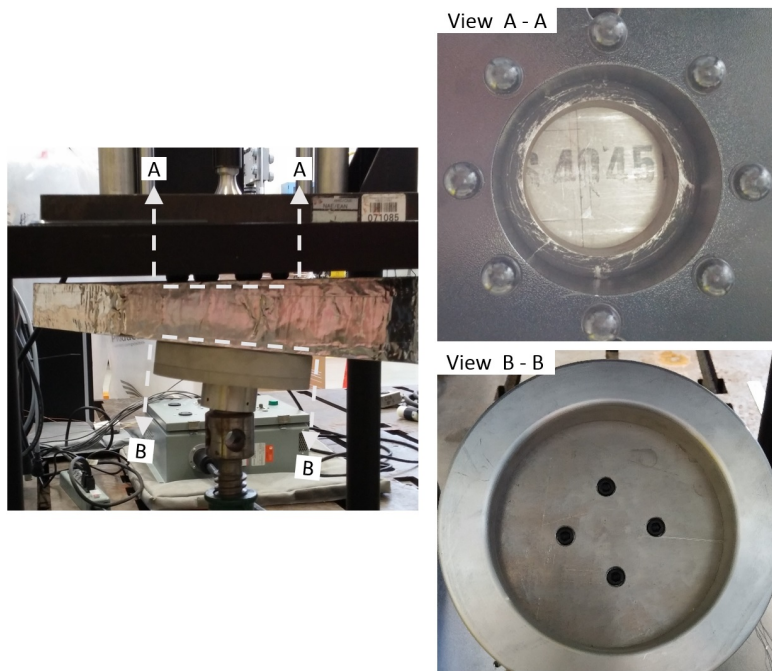
Figure 3.8: Upper and lower support surface (View A-A, B-B respectively).
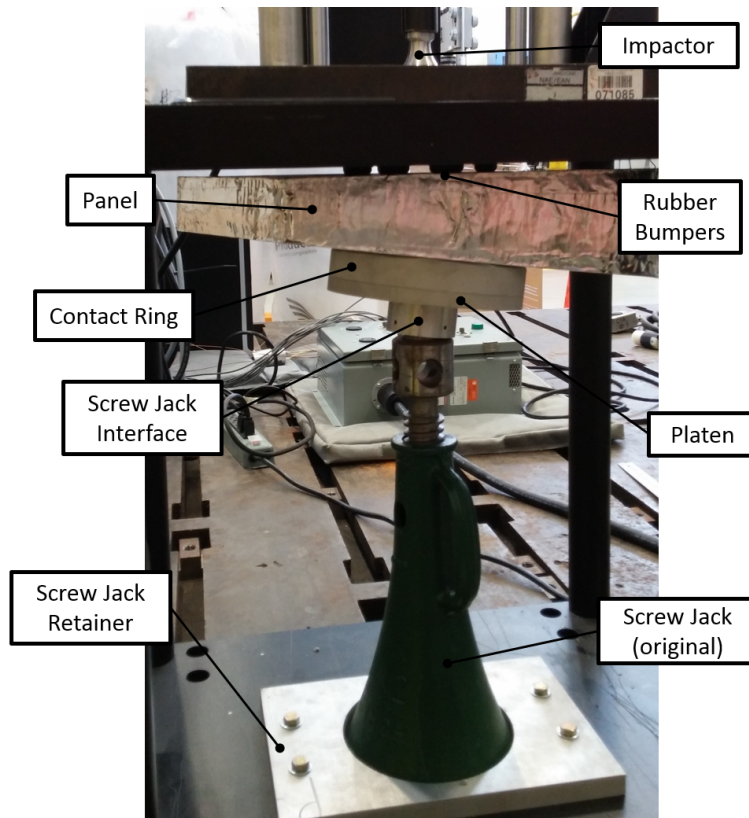
Figure 3.9: Fixture setup with panel B11.

3.3 Non-Destructive Inspection

Damage characterization can be determined using NDI methods prior to sectioning to provide a cross-sectional view of the damage site. The NDI information provides damage characterization detail such as damage area, dent profile, possible failure modes and local stiffness reduction. The force-time history of the impact event helps explain if damage has occurred. Visual inspection and measured dent depth provides a simple damage detection method. A more detailed 3-D profile of the dent can be created using laser topography that is more sensitive when compared to manual measurement. Ultrasonic inspection can reveal core crushing or disbond of the facing from the core. Radiographic inspection can confirm core crush or laminate cracking. The C-scan tap test can detect changes in local stiffness which may reveal the internal damage area as well as the loss of stiffness when compared to the surrounding undamaged panel.

3.3.1 Force-Time Curve

The force-time curve of various impact events are evaluated for general shape and indication of peak load (F_{max}), changes in stiffness (F_1) and contact duration as discussed in Section 2.5.2. Force-time curves are compared when performing repeatability tests; the curves are also compared between the repaired (E3R) and regular panels (E3).

3.3.2 Visual Inspection and Dent Depth

Some of the noticeable indications of damage are from surface characteristics such as visible dents, cracks, fibre breakage, and puncture [41]. Other methods can detect internal and surface damages that may not be apparent to the naked eye.

The visual inspection revealed qualitatively if damage such as impact dents, facesheet cracking or paint chipping were detectable in a well-lit room from about 3 feet away. This was to simulate damage that would likely be detected by aircrew on a preflight walk-around.[1]

Following impact, a picture was taken of the impacted panel. Panel B11 is detailed in Figure 3.10 showing that the damage was not very noticeable from about three feet away for the larger impactors. The upper-left impactor seen in

---

[1]Probability of detection was not explored for any of the inspections in this thesis. Visual inspection reliability is a complex subject; *Cook* performed a PhD thesis on the subject noting the effects of surface colour, surface gloss and dent shape [70].

Figure 3.10 is the smallest diameter, and has a more noticeable impact from visual inspection, but as later explored, the bottom-right largest impactor leads to a greater damage area.
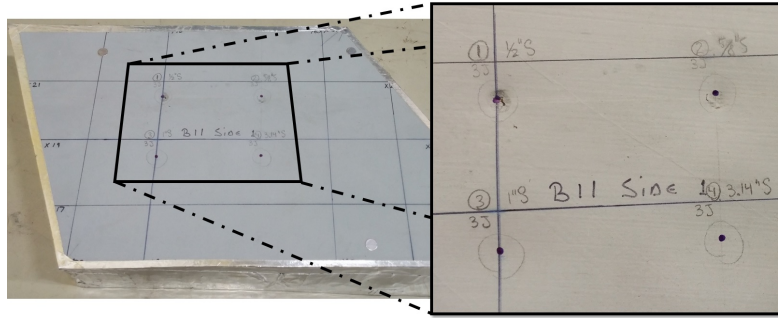
Figure 3.10: Post impact of panel B11 (smaller diameter impactors seen above and larger diameter seen below).

Figure 3.11 shows the method used to determine the maximum dent depth using a set of parallel bars and a micrometer. A dent depth measurement at each impact location was performed once the panel surface had been leveled.

Dent diameter measurements were attempted as per the ASTM D7136 / D7136M-15 [41] measuring eight points from the center of the dent to the level perimeter, however this proved difficult because the surface of the panels had curvature and facing ramps. The measurements for dent diameter require more accuracy, which was not easily achieved using the method outlined in [41]. It was decided that a laser topography would be used to measure dent diameter, as well as detail the overall profile of the dents.

3.3.3 Laser Topography

Surface profiling of the impacted panels was performed using a CCD Laser Displacement Sensor (Keyence LK-086) attached to a THK actuator as seen in Figure 3.12. The complete setup allows the laser to be manipulated in three-directions. This laser sensor operates at $80 \pm 15mm$ from the surface of the item it is scanning (outside of this range does not provide any useful data). Ensuring that the specimen being scanned is as level as possible was helpful to ensure that the scanner would provide a reliable topography of the surface. To do so, a digital protractor was used to shim and level the panels within 0.25 degrees from the horizontal plane seen in Figure 3.13.
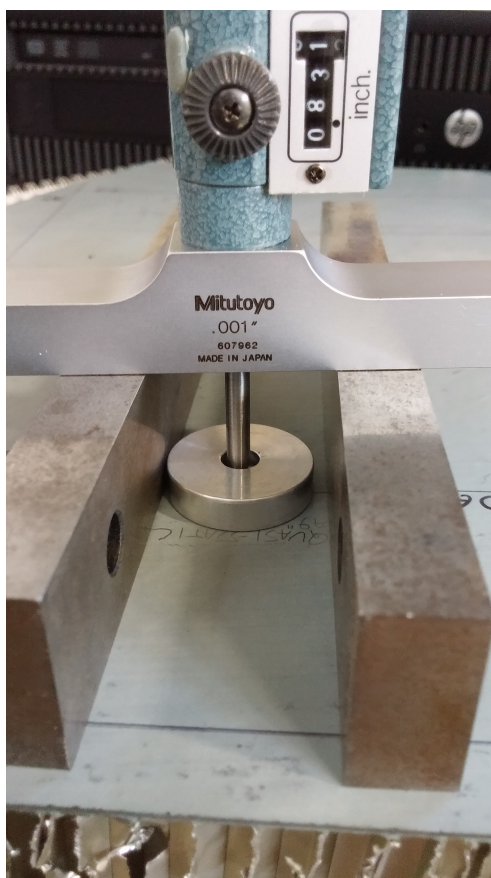
Figure 3.11: Dent depth measurement using a micrometer.

The measurement received from the laser sensor is a voltage, which is converted to a distance and therefore an exact profile of the panel can be determined. In order to determine the exact profile of a dent the selected panels were scanned before impact. With this information, and the lead tape identifiers, in MATLAB the profiled surfaces could undergo a coordinate transformation to be leveled, and subtracted from one-another to leave only the difference, or deviation map between the "good" panel and the "damaged" panel.

The software for scanning was TecView UT (the same software used for ultrasound). The scan increments were 0.25 x 0.25 mm, scan speed was 54.2 mm/s, and the scan method was unidirectional (scans occurred only in one direction, which helps maintain consistency in the measurements). An

48
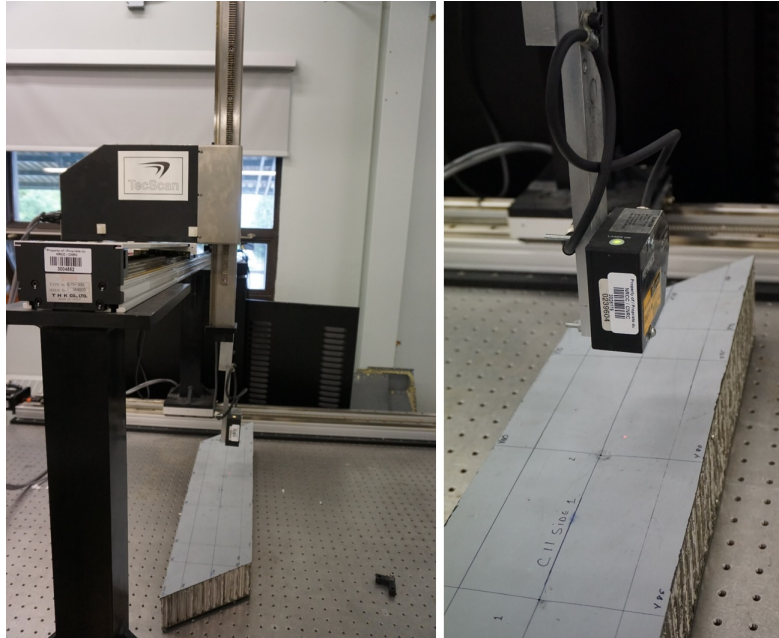
Figure 3.12: Laser topography of a structural composite panel.
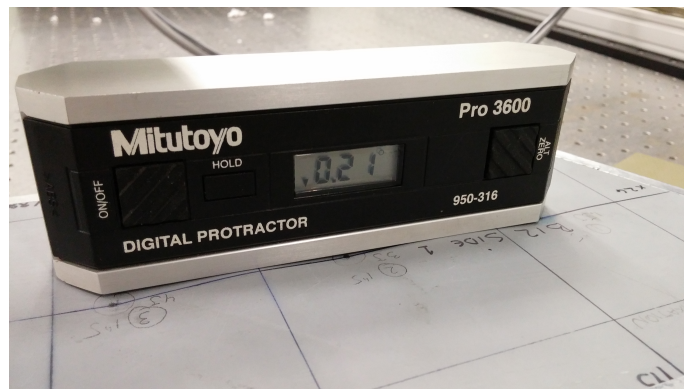
Figure 3.13: Digital protractor to level panels prior to laser topography.

example of an impact-damaged panel (post-processed) is shown in Figure 3.14.
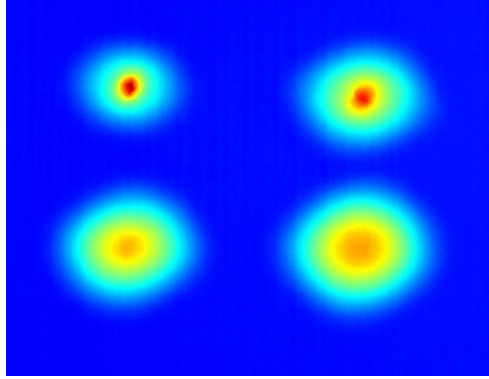
Figure 3.14: Post-processed laser topography of panel B11 (seen in Figure 3.10).

3.3.4   Ultrasonic Inspection

Ultrasonic inspection is a common sub-surface method for detection of foreign materials, delamination, disbonds, fibre debonding, inclusions, porosity and voids [71]. Through-transmission ultrasonic inspection was employed on the sandwich panels, in order to detect any initial damage existing within the panel, as well as to detect facing-to-core disbonds or core crushing post impact.

In preparation for the ultrasonic testing, the cut outer edges of the panels were taped off using an aluminum tape, which prevents the ultrasonic medium (i.e. water) from entering the core of the sandwich composite. The setup used was a TecScan seven axis automated ultrasonic C-scan system with a Utex pulser/receiver and Panametric immersion probes. The data acquisition software used was TecScan [72].

Since the honeycomb sandwich panels were buoyant due to the trapped air in the core cells, weights were placed on top of the panels to ensure they would remain in place during the scan. A panel mid-scan is shown in Figure 3.15.

3.3.5   Radiographic Inspection

Following impact, an X-ray inspection was performed on the panels. The effectiveness of this method will be briefly described in the following chapters. A Lorad LPX160 portable X-ray system was used for the inspections, using
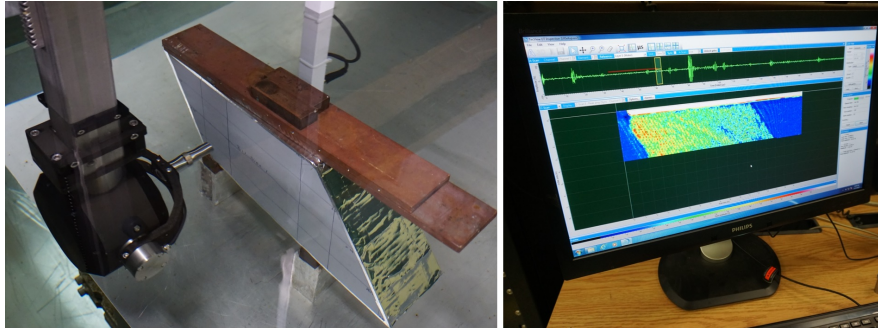
Figure 3.15: Panel B11 in the immersion tank (left) and the C-scan displayed on screen (right).

60 kV and 4 mA for a duration of 20 seconds with 60 inch film-to-focal distance using Kodak MX125 film and Kodak processing [72].

3.3.6   Development of C-scan Tap Test

While the CATT was not available at NRC, it was desired to reproduce the premise of the test using *Microsoft Excel*, an instrumented tap hammer (*Endevco* Model 2302-100), a plastic grid and a PicoScope 2204A oscilloscope and associated software (see Appendix C).

The grid for aiming the hammer and mapping the contact time was created using 1 x 1 cm grid drawn on a transparent piece of plastic. This grid was affixed to the surface of the damaged panels, using the lead tape identifiers as a reference point (for comparisons to other NDI techniques). The grid was tapped using the modal hammer, with 2 g plastic tip attached (EHM1209) as seen in Figure 3.16. This tip seemed the most reasonable since it provided an effective return signal (by being stiff enough) while reducing the potential concern of damaging the panel (by using the harder aluminum tip).

The threshold voltage set for the measurement of contact time was 10 mV. This threshold was used both for contact time measurement, and as a trigger in the software to record the impact event. Setting too low a voltage threshold would lead to recording minor movements of the modal hammer, whereas too high a voltage would miss part of the recorded signal. The force of the hammer tap is output as a voltage, however this can be transformed to a force using the calibration data for the hammer. The hammer had a sensitivity of 22.19 mV/N, and a range of force for measurement of 222.4 N making the peak force of the taps no greater than 3.6 N.

Figure 3.16: Endevco modal hammer and tips (from left to right, plastic, aluminum and rubber).

Following each tap, a voltage-time history was recorded by the PicoScope software, and contact time was manually measured and entered into *Excel*.[1] An example voltage-time history is seen in Figure 3.17. Contact time was recorded in μs. Contact time varied from 380 μs to 960 μs respectively for high to low local panel stiffness.

Each location on the grid was impacted, contact time measured and mapped to the corresponding grid location in *Excel*. Conditional formatting was applied so that:

- High stiffness areas would be blue corresponding to underlying structure or higher density core;
- Medium stiffness areas would be green corresponding to an undamaged panel; and
- Low stiffness areas would be red to indicate damage.

As can be seen in Figure 3.18, an example panel shows how damage can be detectable over an area. By setting a contact time threshold (effectively a threshold for a "damaged" versus "undamaged" stiffness level) the damage area can be approximated, and by looking at the level of contact time, a value can be attached to the amount of damage that is present at a specific location.

The threshold contact time was selected in order to determine a damage area for panel B11, however this threshold would vary based on the modal hammer and tip used, as well as the structure being analyzed in order to

---

[1]It is recommended to automate this process for future use of this method; manual entry of contact time is tedious and wouldn't be practical for field usage.
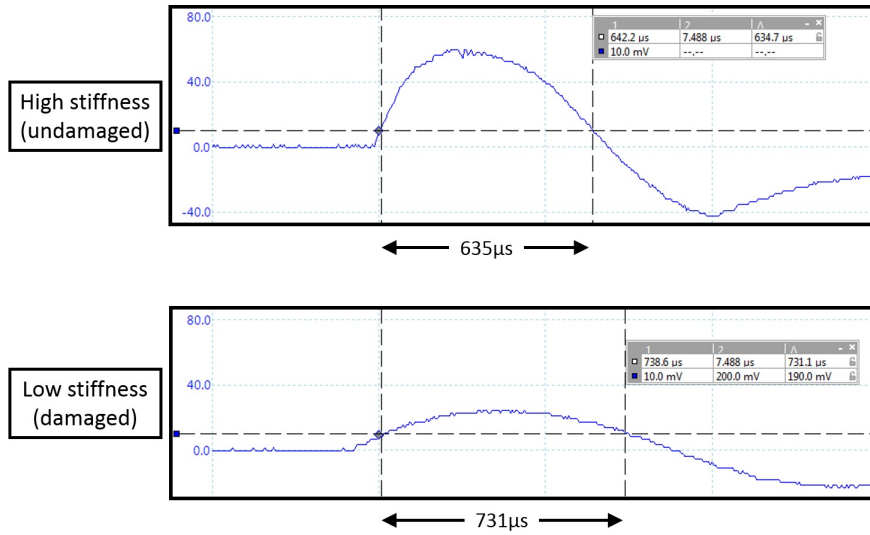
Figure 3.17: Voltage-time history showing high and low stiffness locations. Lower stiffness corresponds to underlying damage.
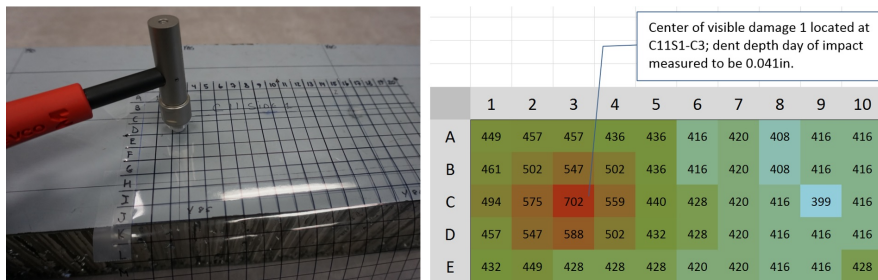
Figure 3.18: C-scan tap test with mapped contact time.

produce a consistent result. If damage area is to be successfully used in practical sandwich panel inspection, procedures and data tables would be required to properly size internal damages.

3.4 Destructive Characterization

Only one method of destructive characterization can be chosen; once the component is sectioned or the plies are chemically separated to observe delamination size and shape, the component cannot be reconstructed. The most appropriate destructive damage characterization method to observe the sandwich failure modes of interest consists of sectioning through the impact area and observing the cross-section. Using a microscope, the damage can be qualified for the impact event.

3.4.1 Sectioning

An initial rough cut was performed on the panels to create the specimen sizes required for further sectioning. The rough cutting was performed with a metal band saw while carefully controlling the feed rate of the panels. While the cuts looked rather clean, under the microscope the rough-cut led to laminate and core damage, and was not appropriate for determining failure mode as seen in Figure 3.19. These pieces were rough cut around the damage areas, and the additional sectioning would be the final preparation prior to damage characterization (Figure 3.20).

A diamond cut-off wheel (Struers M1D20, 200 mm diameter, 0.8 mm width, 22 mm bore) was used to section the rough-cut pieces. A wheel speed of 1900 rpm and a feed speed of 0.100 mm/s was used, and previously tested to ensure that this produced a good quality cross-section under the microscope. These pieces were secured in place using a Kopal vertical clamp. The complete setup before and after cutting can be seen in Figure 3.21.

3.4.2 Microscopy

A VHX 5000 series digital microscope was used for impact zone damage characterization of the cross-sections (see Figure 3.22). This specialized microscope allowed for excellent depth of field in colour, which was ideal for keeping the honeycomb core and the laminate cross-section in focus. It provided a tool for taking measurements of damage, and was user friendly. The microscope was capable of 3-D image stitching for showing the damage zone in detail.
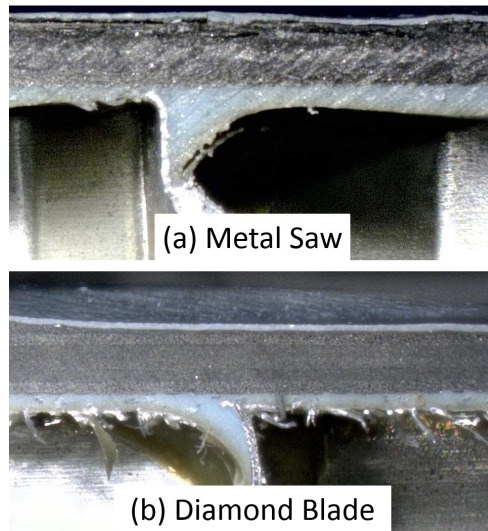
Figure 3.19: Rough cut (a) using a metal saw and (b) clean section using diamond cut-off wheel observed under microscope.
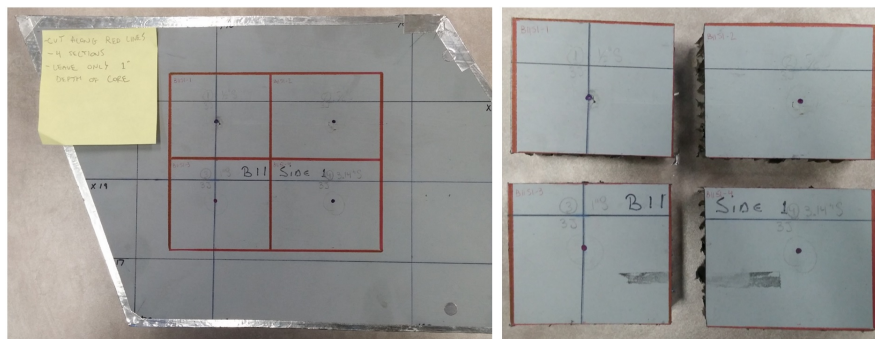
Figure 3.20: Rough cut of panel around damaged zones.

Figure 3.21: Specimen ready for sectioning (left) and sectioned and ready for damage characterization (right).

All impact sites were observed in this way, and details regarding failure mode (i.e. delamination, disbond, and/or core crushing), and quantitative damage are evaluated in the following chapters.
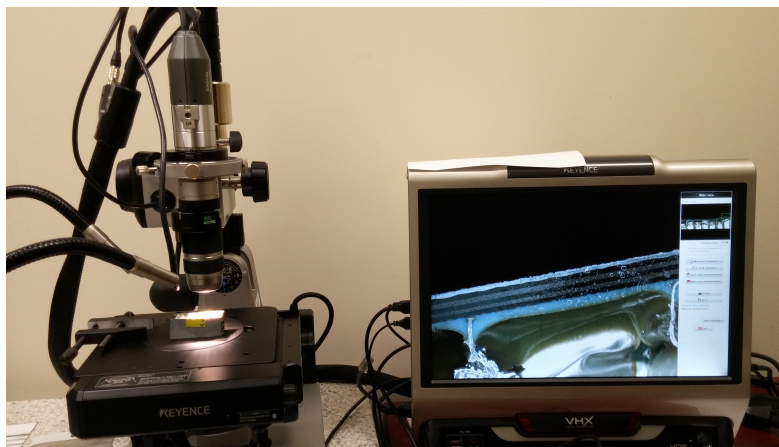
Figure 3.22: Digital microscope in operation.

4 Results

Four studies were undertaken to investigate damage caused by low velocity impact on composite sandwich panels:

1. Damage as a function of impactor diameter
2. Impact on a repaired versus regular panel
3. Effectiveness of the C-scan tap test for damage characterization
4. Dent relaxation of a composite sandwich panel

Each of the above studies compliment the main goal of exploring topics related to damage characterization. The study of impactor diameter investigates how failure modes, damage depth, damage diameter and stiffness change for a given energy level (section 4.1). Assessing the unique situation of impact on a previously repaired panel may benefit design of repairs to take into account out-of-plane impact, or perhaps enhance inspection considerations when a repair is performed on composite panels (section 4.2). The effectiveness of the C-scan tap test may provide more confidence in the CATT or alternate local stiffness NDI methods for consideration when inspecting for damage, or as an inexpensive field-implementable NDI solution in detecting and determining the extent of damage for sandwich panels (section 4.3). Being able to understand the amount of dent relaxation expected in a panel provides credibility when certifying structures for dent limits (section 4.4). Table 4.1 shows the characterization methods used and discussed in each study, as well as the specific panels utilized to achieve the goals of the study. Table 4.2 further details the various panels used and the total number of impacts, hemispherical impactor diameter used as well as the target energy level.

Table 4.1: Outline of panels used and characterization techniques utilized for each study.

| Study and Panel(s) Used | Characterization Technique[1] | | | | | | |
| | Non-Destructive | | | | | | Destructive |
	Force-Time Curve	Visual & Micrometer	Laser Topography	Tap Test	Ultrasonic	X-ray	Sectioning & Microscopy
Impactor Diameter B11 & B14	●	●	●	●	●		●
Repaired vs Regular E3 & E3R	●	●	●				●
C-scan Tap Test B11, D21, E3, E3R & F3				●	●	●	
Dent Relaxation B12			●				

Note 1 – Table does not list all techniques performed; dots indicate if the method was utilized and discussed in the study.

Table 4.2: Total impacts, impactor used and target energy level for each panel.

| Panel | Total Impacts, Impactors Used and Energy Level[1] | | | | | |
	Total Impacts	12.7 mm Steel	15.9 mm Steel	25.4 mm Steel	79.8 mm Steel	79.8 mm Nylon
B11	4	● (3J)	● (3J)	● (3J)	● (3J)	
B12	3			● (1.5J) ● (3J) ● (4J)		
B14	4	● (3J)	● (3J)	● (3J)	● (3J)	
D21	5			●x2 (15J) ● (5J)	● (5J)	● (5J)
E3	3			●x3 (5J)		
E3R	3			●x3 (5J)		
F3	4			●x4 (15J)		

Note 1 – Black dot indicates impactor was used and number of times; the target energy level is specified in brackets (J).

58

4.1 Study 1 - Impactor diameter

This study looks at how increasing dent diameter influences damage for a low velocity impact. Impactor diameter is compared against dent depth, average dent diameter, damage diameter and failure mode. It is expected that increasing diameter will lead to less visual surface damage, smaller dent depth and a possible transition in failure mode. This is relevant to show that the size of the impactor affects the detectability of damage in a composite sandwich panel.

The panels chosen for this study can be seen in Figure 4.1 (selection criteria is discussed in section 3.2.1). Two panels with the same facing thickness and core density were chosen: B11 and B14. Four different diameter impactors were dropped to achieve a 3 J impact energy. Table 4.3 shows key details for the panels, and Table 4.4 shows the drop-tower weights that are included with impactor weight to calculate the necessary height for a 3 J impact.
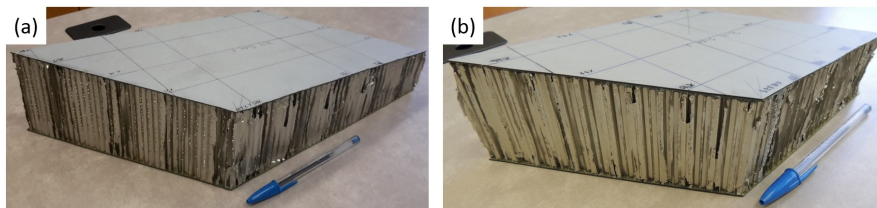
Figure 4.1: Panels chosen for impactor diameter study: (a) B11 and (b) B14.

Table 4.3: Parameters for panel B11 and B14.

Parameter	Unit	Value
Laminate Thickness	µm	650
Core Density	pcf [kg/m^3]	2.3 [36.8]
Core Thickness	mm	49 − 91

Similar panels were chosen to provide a better comparison overall for damage resistance and failure mode. Since panels were symmetric about the midplane, a 90 degree impact (out-of-plane) to the facing means the cell walls are not in-line with the impact force as seen in Figure 4.2; the panels chosen had a small wall-partition angle since large wall-partition angle may increase the amount of impact energy absorbed by the panel [34].

The impacts were performed sequentially from the smallest diameter impactor to the largest. All impactors were hemispherical and made of steel. A
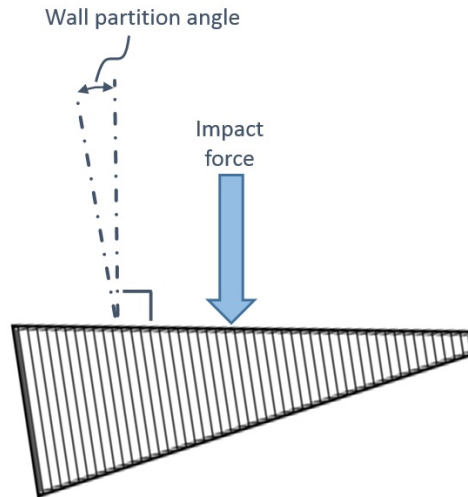
Figure 4.2: Wall partition angle of honeycomb core not aligned with impact force.

Table 4.4: Drop Tower Weights for Energy Calculation

Part	Weight (g)
Crosshead	4535
Attachment & Bolt	1200
Load Cell Assembly	289.4

picture with the impactors next to each impact zone is seen in Figure 4.3 with their diameters, and the actual impact energy achieved for each of the panels can be seen in Table 4.5. Following each impact the impactor was removed, the panel adjusted to the next impact zone, and the height adjusted for the target 3 J energy level.

4.1.1 Force-Time Curve

Consistent impact energy level was not achieved due to the requirement to change the impactors between tests and re-adjust the drop-height for the desired 3 J impact. The impact energy levels achieved for panel B11 and B14 can be seen in Table 4.5 and varied by ± 0.15 J (5 %).

Figures 4.4–4.5 show the force-time curves of the B11 impacts (in black)

60
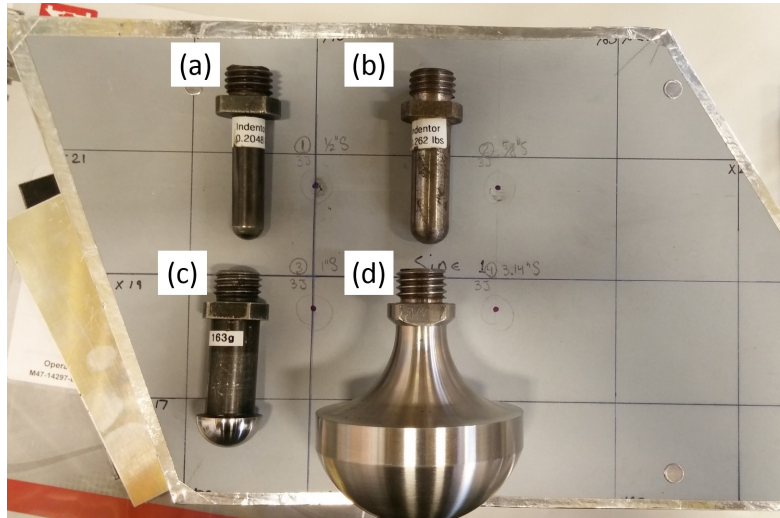
Figure 4.3: B11 with impactors next to impact zones. Tip diameters: (a) 12.7 mm, (b) 15.9 mm, (c) 25.4 mm, (d) 79.8 mm.

Table 4.5: Impactor parameters and impact energy for panel B11 and B14

Impactor Diameter (mm)	Impactor Mass (g)	Drop Height (mm)	Actual Impact Energy B11 (J)	Actual Impact Energy B14 (J)
12.7	93	87	2.76	2.82
15.9	119	87	3.06	2.84
25.4	163	86	2.76	2.83
79.8	1309	72	2.94	2.91

and the B14 equivalent impacts (in orange). The impact from the (smallest) 12.7 mm impactor is seen in Figure 4.4 showing peak load (maximum force where the impactor rebounds and velocity is zero for low-velocity impact), location of stiffness change (i.e. confirmation of damage), core crushing (sometimes visible as a consolidation phase, similar to the stable compression stress as seen in Figure 2.8) and contact time (a function of the impactor, panel local stiffness and damage incurred).

When the impacts for B11 and B14 are compared in Figure 4.4 they produce a similar overall profile. The equivalent impact (in orange) seems to take longer to have a significant failure and yield, however the remainder of the
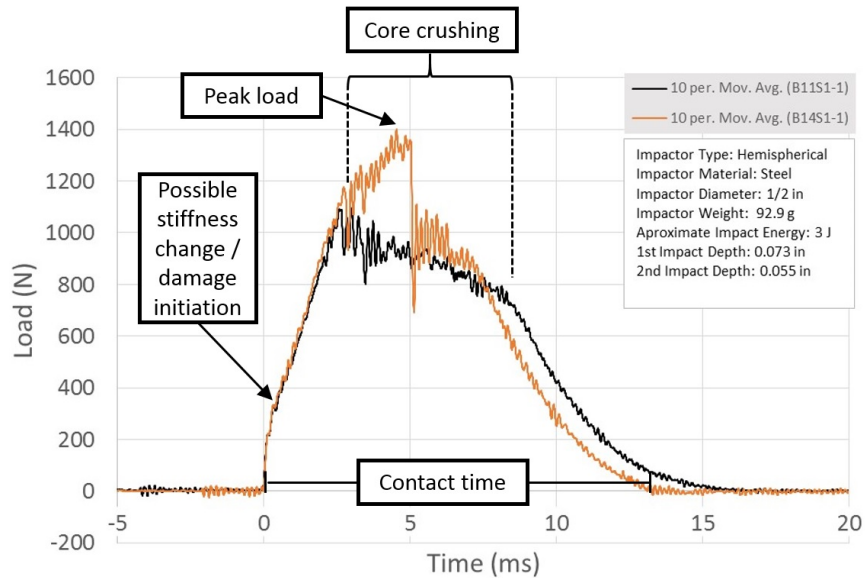
Figure 4.4: Force time curve of 12.7 mm impact and equivalent impact showing location of peak load, core crushing, damage initiation and contact time.

smooth curve is comparable.

Figure 4.5 shows the force time curves for the 15.9, 25.4 and 79.8 mm impacts, and the similar black and orange curves indicate that the expected damage to the panel should be similar for B11 and B14.

For the 15.9 mm impacts, Figure 4.5 (a) shows that panel B11 experienced a brittle facesheet fracture near peak load whereas B14 did not. For the 25.4 mm impacts, Figure 4.5 (b) shows very similar force-time curves. For the large 79.8 mm impactor, Figure 4.5 (c) shows nearly identical force-time curves.
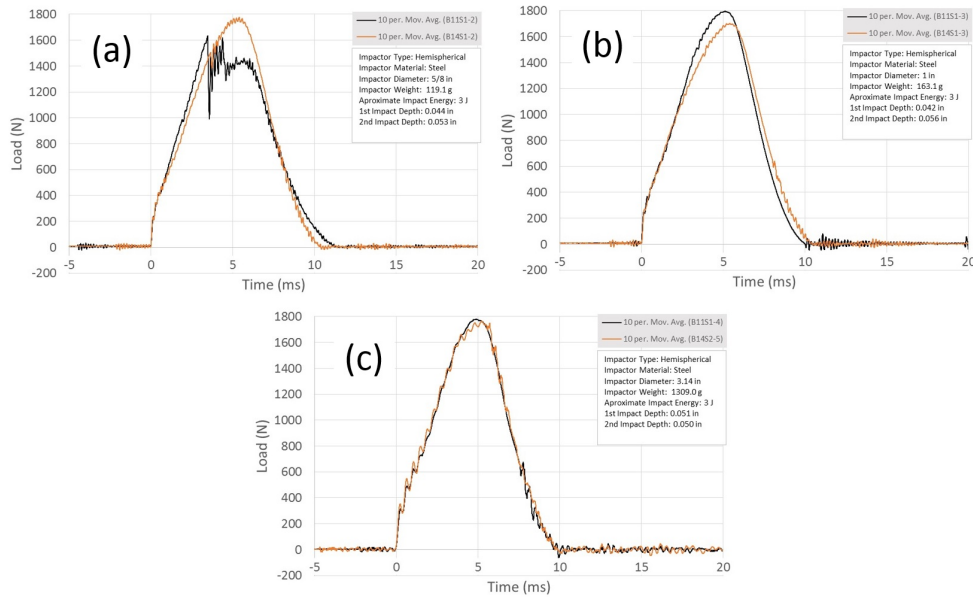
Figure 4.5: Force time curve of (a) 15.9 mm, (b) 25.4 mm, and (c) 79.8 mm impacts.

4.1.2 Dent Depth

The visual comparison and micrometer readings of the impact zones shows the qualitative trend of increased impactor diameter causing damage that is more difficult to see, and quantitative trend of decreasing dent depth. While not all impacts on panel B11 were obvious, they were detectable from up close when observing from a greater angle where the profile of the impact differed from the flat surface of the panel.[1]

The first impact on panel B11 with the 12.7 mm impactor is seen in Figure 4.6 (a). This impact was apparent due to some paint chipping. The 15.9 mm impact is seen in Figure 4.6 (b); this dent was still detectable. The 25.4 and 79.8 mm impacts can be seen in Figure 4.7. Unlike the smaller impactors, the larger impactors were not as easily detectable due a lack of paint chipping and the gradual slope of the dents; however, touching across the surface of the panel would reveal the dent from the larger impactors.

---

[1]This is similar to inspecting a car for denting or warpage; damage is more noticeable looking down the length of a vehicle than observing the surface straight-on.
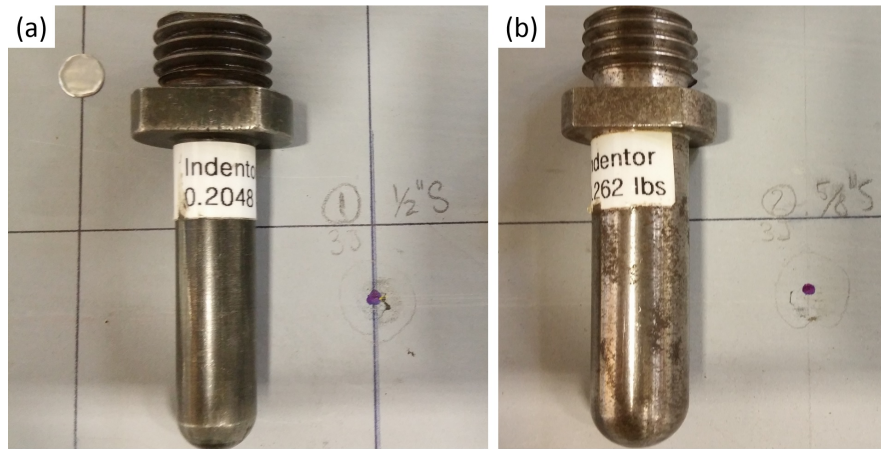
Figure 4.6: B11 (a) 12.7 and (b) 15.9 mm impact, showing paint chipping; impact locations pre-marked with a blue pen and circled lightly with pencil for aligning impactor during test.
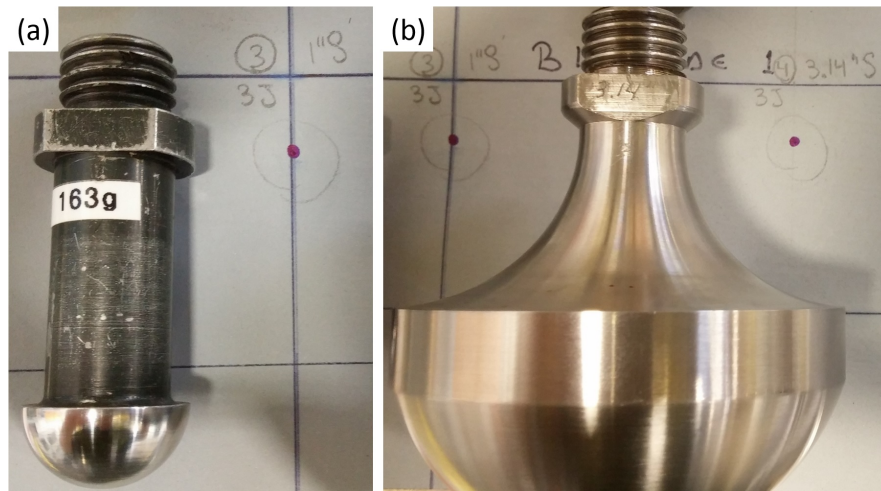
Figure 4.7: B11 (a) 25.4 and (b) 79.8 mm impact, showing no surface marks or noticeable dents.

64

From post-processing of the laser topography measurements, Figure 4.8 shows the B11 dent depth profiles for the 12.7 and 15.9 mm impactors, and Figure 4.9 shows dent depth profiles for the 25.4 and 79.8 mm impactors. The y-axis is stretched compared to the x-axis in order to better show the dent depth. Note that the greatest depth is achieved with the 12.7 mm impactor, while the least depth was the 25.4 mm due to variability in setting the exact drop height (the 79.8 mm impactor would be expected to have the least depth). Normalizing impact depth for actual impact energy does confirm this relationship.
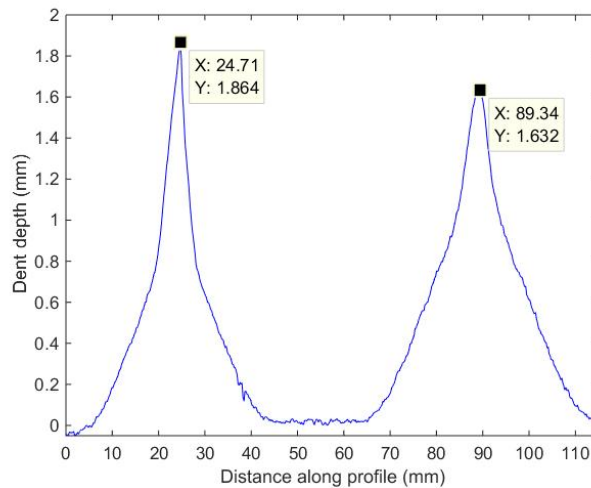
Figure 4.8: Dent profile for B11 across 12.7 (left) and 15.9 mm impacts (right).

Table 4.6 shows a comparison of dent depth for panel B11 and B14. Dent depths for each impactor were similar for both panels. Table 4.7 shows the dent depths of micrometer versus laser topography measurements for panel B11. There was 1 to 31% difference between the two techniques, with the micrometer reading underestimating the depth of the dent. The depths from Table 4.6 and 4.7 are presented in Figure 4.10 to show the relationship between dent depth and impactor size. For a given energy level it was noted that increased impactor diameter tended to lead to decreased dent depth which is the same trend observed in the literature; depth measurements are more consistent for the two panels as the impactor diameter increases.
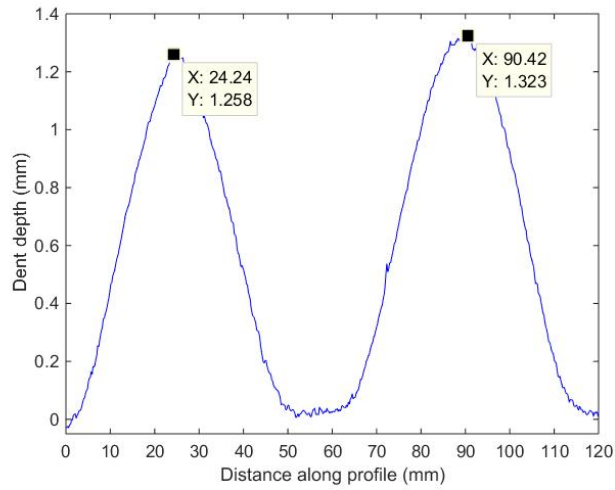
Figure 4.9: Dent profile for B11 across 25.4 (left) and 79.8 mm impacts (right).

Table 4.6: Dent depth micrometer readings for impactor sizes at ~3 J

Impactor (mm)	B11 Depth (mm)	B14 Depth (mm)	Delta abs (mm)	Delta %
12.7	1.854	1.397	0.457	25%
15.9	1.118	1.346	0.229	20%
25.4	1.067	1.422	0.356	33%
79.8	1.295	1.270	0.025	2%

Table 4.7: B11 Dent depth micrometer and laser topography

Impactor (mm)	Depth Micrometer (mm)	Depth Laser Topography (mm)	Delta abs (mm)	Delta %
12.7	1.854	1.864	0.010	1%
15.9	1.118	1.632	0.514	31%
25.4	1.067	1.258	0.191	15%
79.8	1.295	1.323	0.028	2%

66
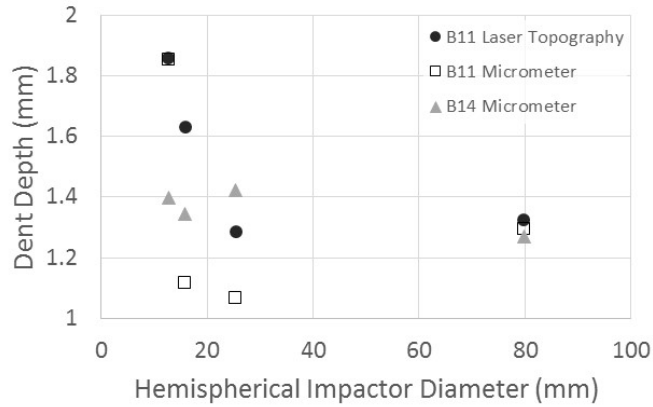
Figure 4.10: Dent depth versus impactor diameter. The trend of increasing impactor diameter leads to decreased dent depth for a given energy level.

4.1.3 Dent and Damage Diameter

As detailed in section 3.3.3 using laser topography allowed for a measurement of dent diameter along with a complete 3-D profile of the dent surfaces for panel B11. By taking an initial scan of the undamaged panel, and a post-impact scan (approximately one hour following impact by the drop tower), these two profiles could be leveled in MATLAB and subtracted from one another, leaving only an accurate depiction of the impact dent.

The initial scan of panel B11 can be seen in Figure 4.11. The colour changes represent the panel not being perfectly level, along with its natural curvature. Note the three lead tape identifiers; these make the deviation map possible in post processing.

Figure 4.12 shows the leveled before-impact (a) and post-impact (b) surface of B11. Once the before and after impact topographies have been leveled, the image registration toolbox is used in MATLAB to translate and rotate the two datasets, and subtracting them from one another, leaving only the difference as seen in Figure 4.12 (c).

67
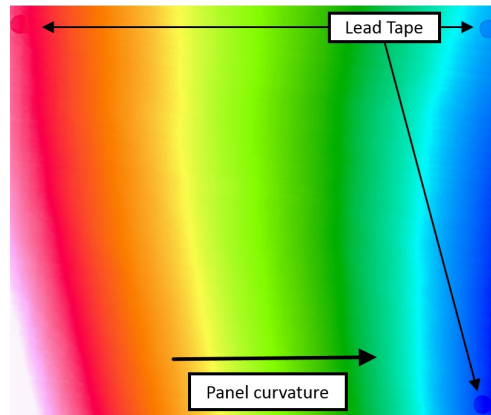
Figure 4.11: B11 laser topography C-scan before impact and lead tape at the top-left, top-right and bottom-right corners. Colours indicate panel slope and curvature.

The contour graphs in Figures 4.13–4.16 show the dents corresponding to the smallest to largest impactors, respectively. Diameters were comparable to the through transmission ultrasound as seen in Figure 4.17. Each laser topography contour line represents 0.2 mm, and is the initial threshold used to measure diameter for each dent. This threshold was selected as it corresponds well with the damage area for the smaller impactors.[1]

---

[1]Each of the NDI methods used may have a defined threshold for measuring damage or sensitivity limitations, which would require further exploration to compare one method to another, ideally with a measured sectioning and characterization of the impact locations. Damage and dents gradually dissipate towards the perimeter, and it can be difficult to define an exact location where it begins and ends.
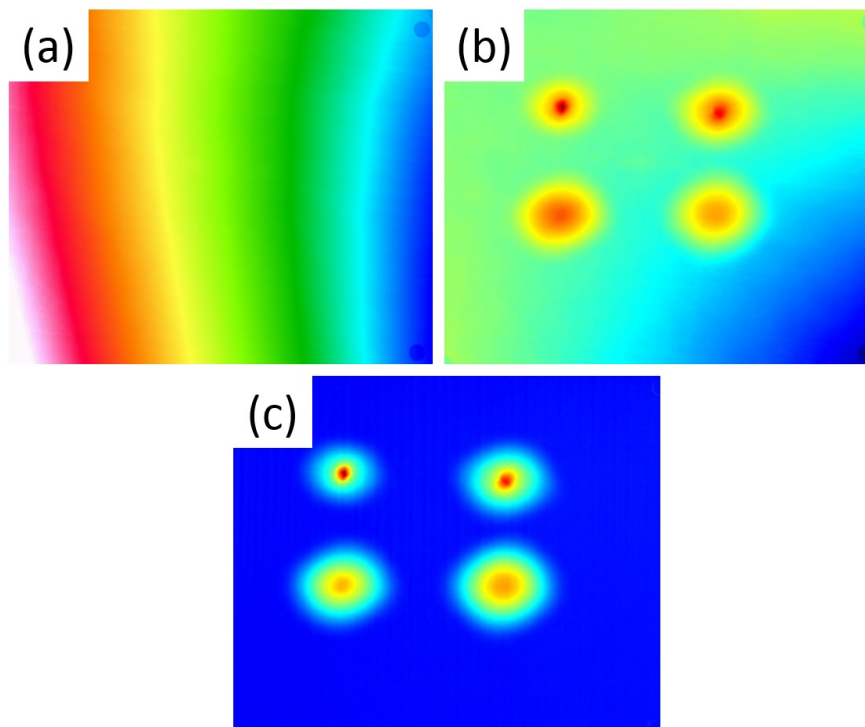
Figure 4.12: B11 (a) before impact showing panel curvature, (b) after impact showing dents and panel curvature, and (c) deviation map showing only dents and no panel curvature. Colours qualitatively show panel curvature and dent profile.
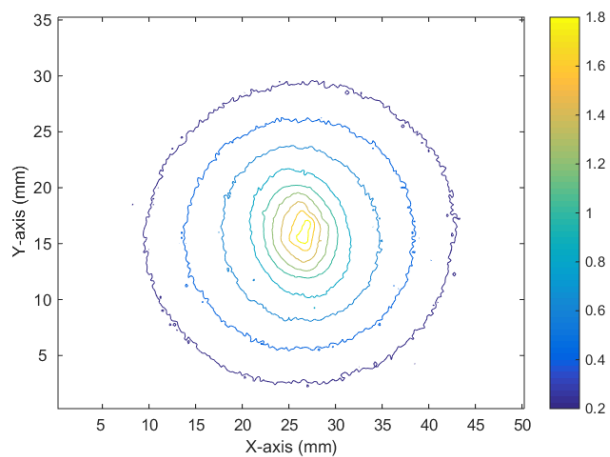
Figure 4.13: Contour of B11 12.7 mm impact.
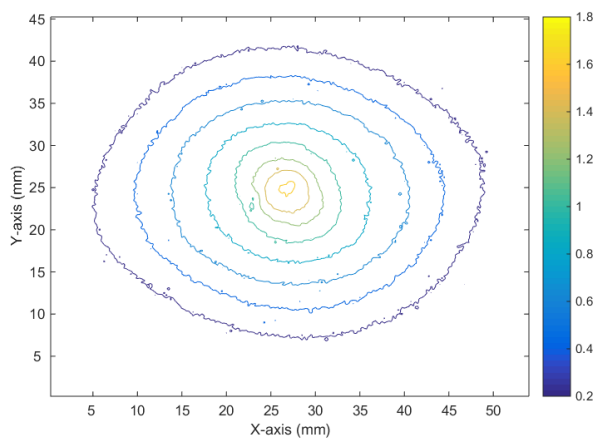
Figure 4.14: Contour of B11 15.9 mm impact.
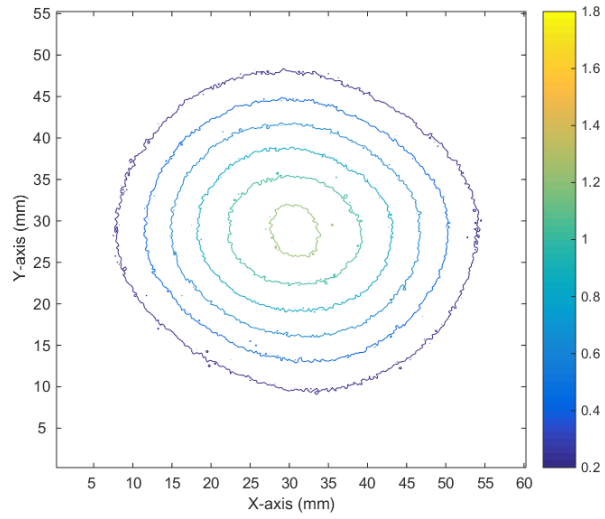
Figure 4.15: Contour of B11 25.4 mm impact.
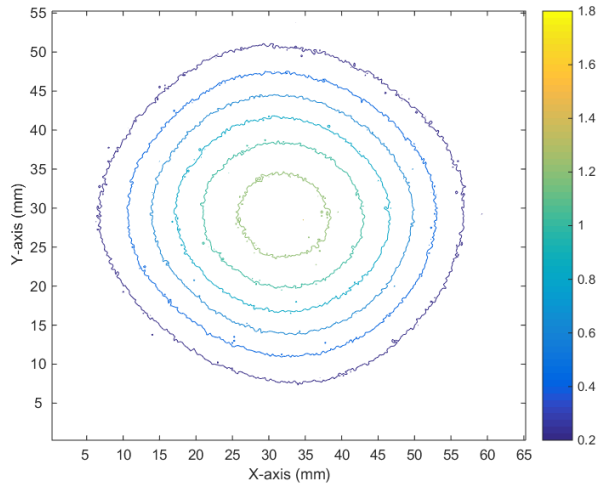
Figure 4.16: Contour of B11 79.8 mm impact.
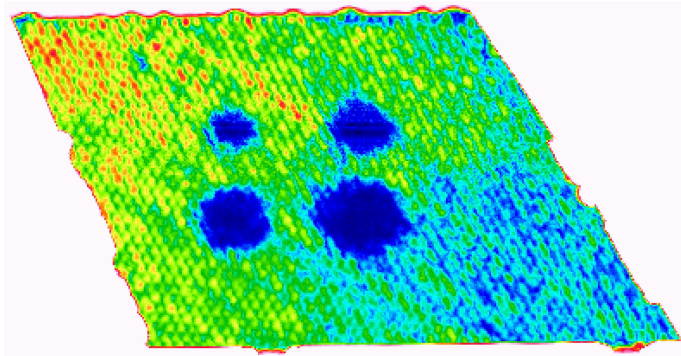
Figure 4.17: B11 after impact through-transmission ultrasound. Damage diameter 30.5, 40.6, 43.2 and 61.0 mm respectively from smallest to largest impact.

The damage diameter was also determined by carrying out the C-scan tap test as per section 3.3.6; Figure 4.18 shows the local contact time map for the damaged B11 panel. By subtracting the average contact time for the panel, and determining the standard deviation, a 3σ contact time was applied as the damage threshold. Damage areas using this threshold are shown in Figure 4.19.

	1	2	3	4	5	6	7	8	9	10	11	12	13	14	15
A	551	601	606	626	591	551	551	581	576	551	526	566	556	566	566
B	601	541	591	589	621	566	556	571	571	581	631	621	616	546	551
C	586	541	626	676	706	651	571	586	556	616	686	681	671	581	586
D	561	591	616	716	766	696	566	616	571	651	771	786	741	636	596
E	556	541	581	621	676	626	591	576	596	596	606	641	666	621	571
F	536	541	561	561	586	596	601	611	606	596	596	656	586	601	561
G	566	561	611	671	636	616	581	601	621	631	676	706	671	646	616
H	531	591	656	716	691	661	616	596	596	701	701	746	716	701	621
I	546	576	666	756	741	681	616	586	621	711	716	746	711	696	646
J	546	546	636	676	696	646	631	601	601	701	721	731	721	711	651
K	536	581	596	631	631	591	596	621	591	611	696	701	701	671	641
L	536	536	546	556	546	581	591	591	601	596	591	596	636	646	601

Figure 4.18: Local contact time map for B11 (μs).

-3	47	52	72	37	-3	-3	27	22	-3	-28	12	2	12	12
47	-13	37	35	67	12	2	17	17	27	77	67	62	-8	-3
32	-13	72	122	152	97	17	32	2	62	132	127	117	27	32
7	37	62	162	212	142	12	62	17	97	217	232	187	82	42
2	-13	27	67	122	72	37	22	42	42	52	87	112	67	17
-18	-13	7	7	32	42	47	57	52	42	42	102	32	47	7
12	7	57	117	82	62	27	47	67	77	122	152	117	92	62
-23	37	102	162	137	107	62	42	42	147	147	192	162	147	67
-8	22	112	202	187	127	62	32	67	157	162	192	157	142	92
-8	-8	82	122	142	92	77	47	47	147	167	177	167	157	97
-18	27	42	77	77	37	42	67	37	57	142	147	147	117	87
-18	-18	-8	2	-8	27	37	37	47	42	37	42	82	92	47

Diameter 1 (cm)	2.99
Diameter 2 (cm)	3.91
Diameter 3 (cm)	4.65
Diameter 4 (cm)	6.08
Average Contact Time Over Damage Area 1	144
Average Contact Time Over Damage Area 2	130
Average Contact Time Over Damage Area 3	118
Average Contact Time Over Damage Area 4	137

Figure 4.19: Damage map for B11 (μs)

A comparison of dent and damage diameter measurements can be seen for the B11 impacts in Table 4.8 and Figure 4.20. As impactor diameter increases, the dent diameter increases. Note that ultrasound and C-scan tap test measure internal damage, whereas laser topography measures the edge of the dent (which provides an indication of underlying damage). How well these methods correspond depends on their respective sensitivity and threshold selection.

Table 4.8: Dent and damage diameter for impactors at $\sim$3 J for panel B11

Impactor (mm)	12.7	15.9	25.4	79.8
Diameter Laser Topography (mm)	30.0	37.9	42.7	46.9
Diameter Ultrasound (mm)	30.5	40.6	43.2	61.0
Diameter C-scan Tap Test (mm)	29.9	39.1	46.5	60.8
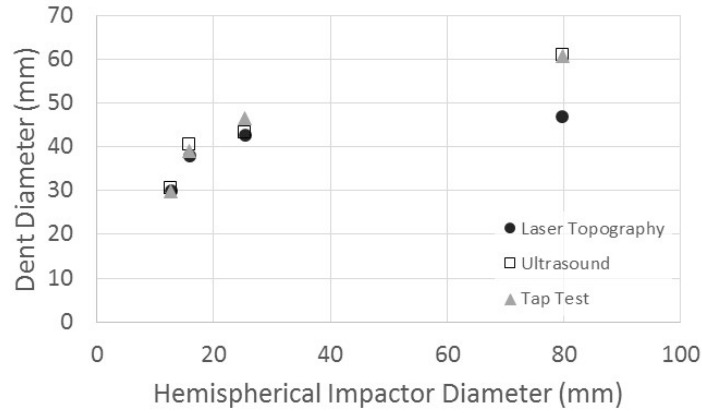
Figure 4.20: Comparison of dent and damage diameter methods.

4.1.4 Failure Mode

Sectioning was performed on each of the B11 impact zones to qualitatively observe failure mode. Figure 4.21 shows an undamaged edge-sectioned piece as a baseline for use when observing impacted areas. The locations where the failure modes are most likely to occur are identified along with where the impactor will strike the panel surface.
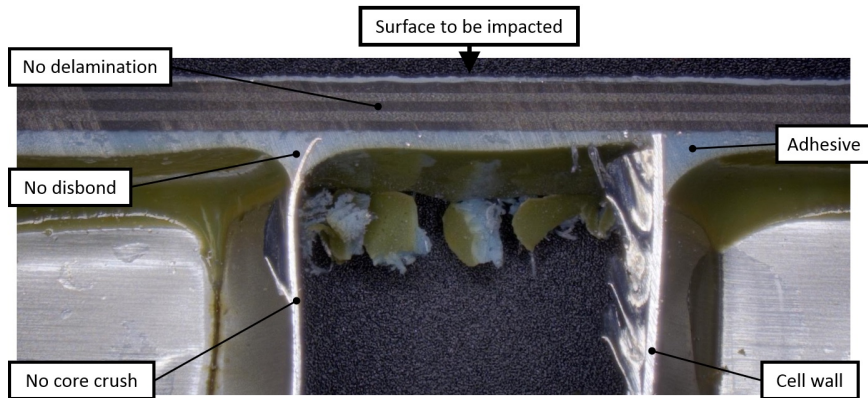
Figure 4.21: Section of B11 with no damage present.

The 12.7 mm impact for panels B11 and B14 can be seen in Figure 4.22. There is significant fibre damage as well as a fairly localized core crushing.

75

Under greater magnification in Figure 4.23, the failure mode is mixed: fibres under the impact zone are all damaged and the bond between the core and laminate has cracked (along with the crushed core previously mentioned). The profile section of the B14 12.7 mm impact is shown in Figure 4.24 and has very similar damage.
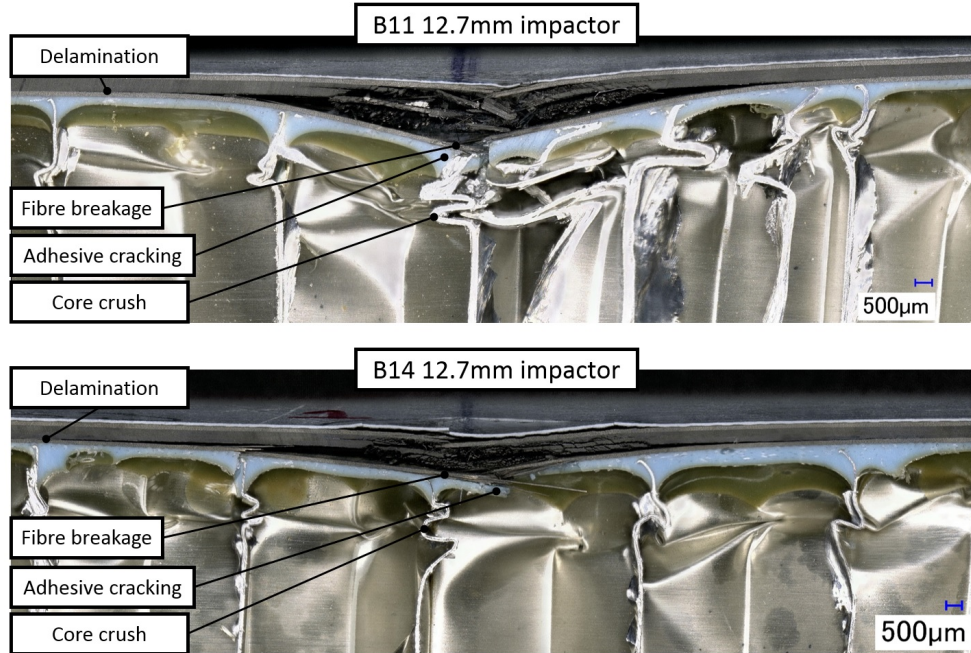
Figure 4.22: B11 and B14 12.7 mm impact cross section with laminate damage, adhesive cracking and core crush.

The cross-sections for the 15.9 mm impact can be seen in Figure 4.25. This is still a mixed failure mode, however the amount of laminate damage and core crush is less when compared to the 12.7 mm impact. The profile of B14 impact is similar to B11, however the laminate damage seems less significant as seen in Figure 4.26. This may be due to the fact that B14 15.9 mm impact had a calculated impact energy level of 2.84 J versus 3.06 J for B11 15.9 mm impact.

Figure 4.27 shows the 25.4 mm impact for both panels. This is still a mixed failure mode, however it is less apparent in these sections. The failure mode continues to transition towards core crush over a greater area with less noticeable laminate damage. In Figure 4.28 delamination for B11 is visible at greater magnification.

Figure 4.23: B11 12.7 mm local impact zone.
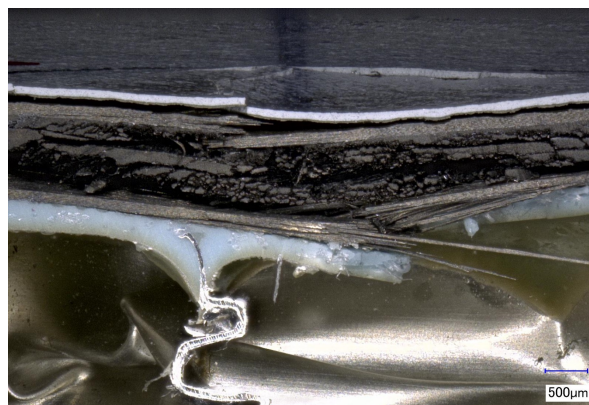
Figure 4.24: B14 12.7 mm local impact zone.
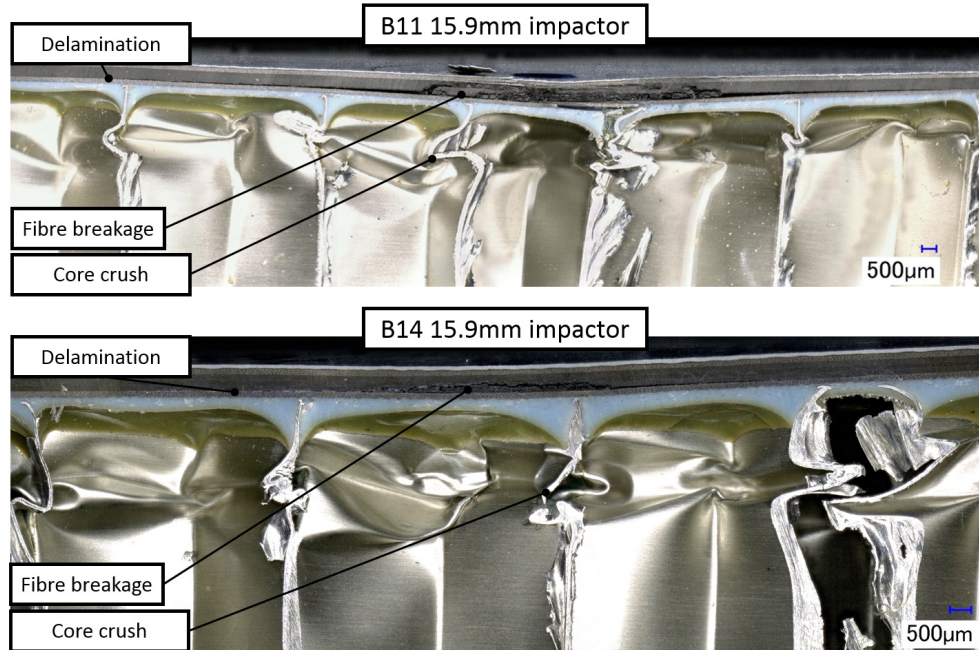
Figure 4.25: B11 and B14 15.9 mm impact cross section with laminate damage and core crush.
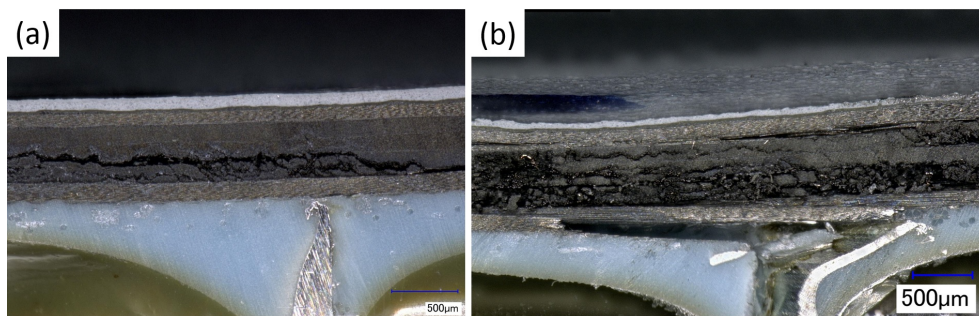
Figure 4.26: 15.9 mm impact of B14 (a) 2.84 J and B11 (b) 3.06 J showing greater laminate damage for higher energy impact.
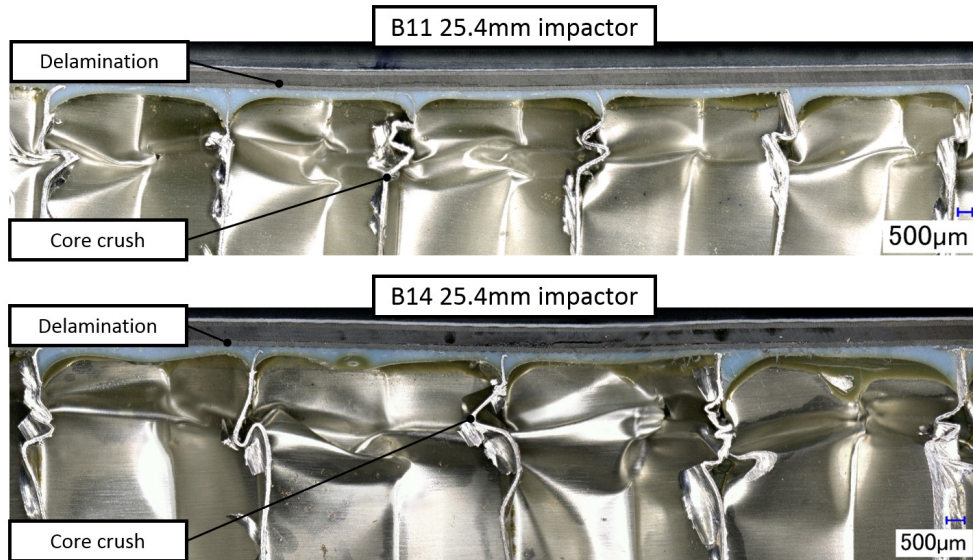
Figure 4.27: B11 and B14 25.4 mm impact cross section with delamination and core crush. Discolouration of B14 laminate due to diamond blade cutting through tape that was affixed to the top of the panel.
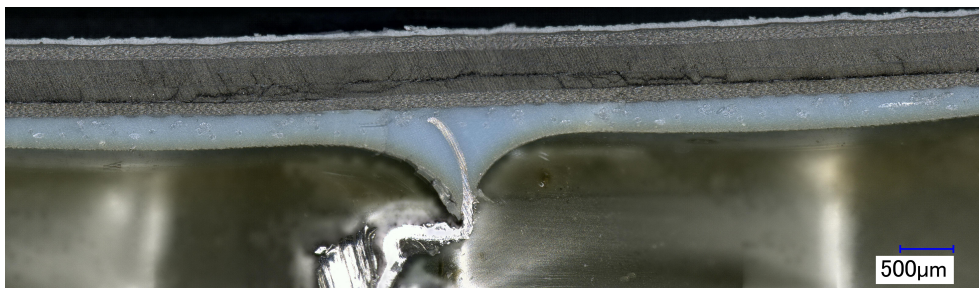
Figure 4.28: B11 25.4 mm impact delamination.

79

The 25.4 mm impact on B14 exhibits the same failure as B11, including the same delamination that initiates underneath the impact zone, after the middle ply and then extends to the next lower ply, as seen in Figure 4.29.
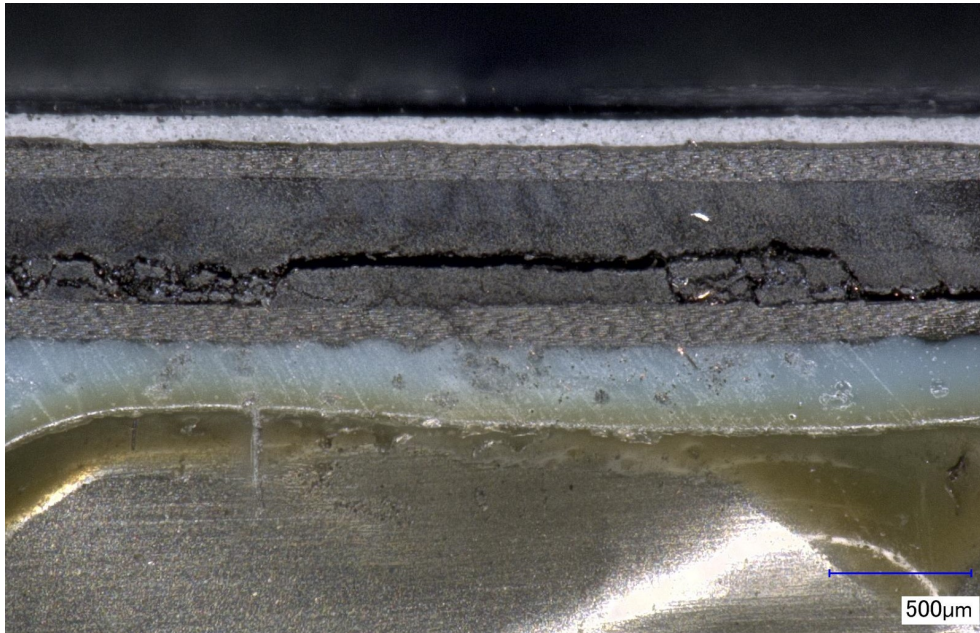
Figure 4.29: Delamination for B14 25.4 mm impact.

Figure 4.30 shows that for the largest diameter impactor the failure mode has shifted exclusively to core crush. There is no laminate damage, however it can be seen in Figure 4.31 that the paint above the laminate has cracked. The 79.8 mm impact on B14 utilized the same impactor and energy level as B11. The same outcome was observed: core crushing was the only damage caused by the largest diameter impactor, with no delamination as seen in Figure 4.32.
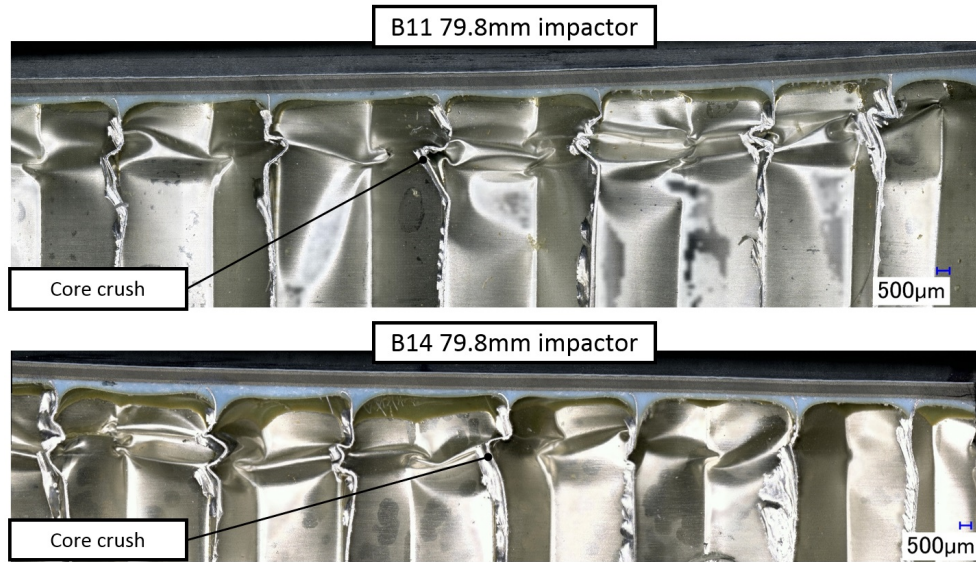
Figure 4.30: B11 and B14 79.8 mm impact cross section with core crush.
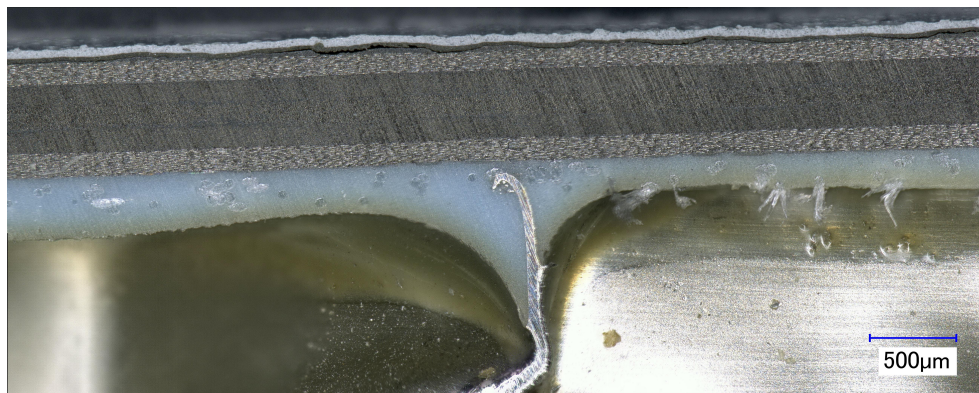
Figure 4.31: B11 79.8 mm impact with no laminate damage.
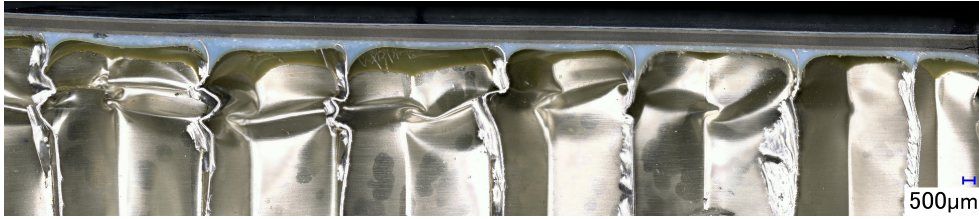
Figure 4.32: Core crushing of B14 79.8 mm impact. Note some delamination along right edge of the laminate; this was likely a result of the rough-cutting, and is not a result of impact.

4.1.5 Summary

Dent depth appears to decrease as impactor diameter increases. Due to the small measurements of dent depth and the variance between equivalent impacts of the same size, this does not appear to be as consistent as measuring dent and damage diameter. Dent and damage diameter measurements are large compared to dent depth, and it appears to show a strong correlation to impactor diameter.

Failure mode changes from laminate damage and core crush to only core crush as impactor size increases. No disbonding was noticeable for this material, impactor and energy level combination except for the local adhesive cracking which occurred for the 12.7 mm impactor.

While all impacts were detectable by the available NDI methods, visual inspection of the panels from a distance would not be a reliable method of detecting large, blunt impact dents.

4.1.6 Discussion

Force-Time Curves

The force-time curve appears to be more consistent when comparing equivalent impacts for a larger impactor. When comparing panels B11 and B14 in Figure 4.4 and 4.5 the smaller impactors (12.7 and 15.9 mm) towards peak load appear to be inconsistent, sometimes experiencing significant oscillations, whereas the larger impactors (25.4 and 79.8 mm) appear to have more consistent loading, with less inconsistency at peak load. The inconsistency for smaller impactors can be attributed to the higher localized loading and sudden brittle laminate fracture combined with core crushing. While the damage

incurred with the 12.7 and 15.9 mm impactor appears to be similar, due to the brittle nature of the CFRP, the laminate layers may fail at different loads whereas the aluminum buckles at a more consistent load. The force time curve becomes very consistent for larger impactors since there is no fibre breakage and the failure mode is exclusively core crush. The constant load that would be experienced by unsupported core crushing is not detectable since the facesheet bonded to the core conceals this effect in the force-time history, however for brittle fracture this constant load is seen as a discrete event once the facesheet has failed as seen in Figure 4.4. Due to the shift in failure mode from a combined laminate and core crush to only core crush, the brittle element of the impact has disappeared which provides more consistent results; the core is being crushed while the laminate bends.

Dent Depth

Dent depth tends to decrease with increasing impactor diameter, given a constant impact energy level. The largest impactor had similar dent depth for panel B11 and B14 while all the smaller impactors had more variability in their depth measurements. The micrometer appeared to underestimate the depth value, and the 15.9 mm impactor had a large measurement difference, possibly attributed to a measurement error (not correctly recording the depth) or difficulty measuring the center of the impact. Due to the challenge associated with achieving a consistent energy level and a limited supply of panels, it is difficult to reach a definitive conclusion on the relationship between impact depth and impactor diameter beyond a general trend. While there is a noticeable relationship between failure mode, amount of damage incurred and impactor diameter, the same relationship is not present in the depth measurements; measurement of dent depth does not appear to be an accurate predictor of underlying panel damage.

Dent and Damage Diameter

Dent and damage diameter increase with impactor diameter for a given energy level which corresponds with the literature. It was found that measuring dent diameter may under or over-predict underlying damage, depending on the impactor size and the measurement sensitivity.

Failure Modes

Figure 4.22 to 4.30 shows the trend of decreasing damage and reduced failure mode for increasing impactor size. The 12.7 mm impactor shows fibre failure,

delamination, cracked facesheet to core bond as well as crushed core. Fiber breakage is not as apparent from the 15.9 mm impactor, however delamination, cracked bondline and crushed core are still present. The 25.4 mm impactor shows less delamination and less core crushing, and for this impactor-energy combination matrix cracking is observed to initiate from below the middle 90 degree ply, and then shear to above the lower ply causing a delamination between the +45/-45 degree ply as seen in Figure 4.29. Delamination is more likely at this ply interface since the angle is greatest between the plies, and due to flexure of the thin laminate, the in-plane loads are greater at the lower plies. For the 79.8 mm impactor, aside from some damaged for the surface paint, the only failure mode is core crush. The largest impactor experiences less core crush because of reduced dent depth when compared to the smaller impactors.

The laser topography profile curvature may be able to determine if fibre failure has occurred for the material combination of CFRP facesheet and aluminum alloy honeycomb core. This concept is summarized in Figure 4.33. The sharp profile of Figure 4.8 corresponds to fibre failure and delamination as seen in the Figure 4.23 and 4.25 cross-sections. Figure 4.9 shows the profiles for the larger impactors; these profiles have different curvature and also less laminate damage as seen in Figures 4.28 and 4.31. It may be of interest for future studies to evaluate if the fibre failure of the laminate can be distinguished through the use of laser topography.

BVID and Damage Limits

One of the difficulties in this study was performing accurate depth and diameter measurements. Measurements on coupons are simpler because the facesheets are usually flat and parallel. Using depth as a measure of BVID does not seem to be an accurate way of determining damage extent, whereas slope or rate of change in depth would be better measures for what would be visually detectable; this would require multiple measurements at fixed intervals from the center of the impact site. A dent caused by a large impactor would be more difficult to see than that caused by a small impactor for the same dent depth, and the failure mode may vary significantly. Suspect impact locations would be better categorized using an damage threshold determined from an NDI method. Laser topography would allow for a more precise way of studying and defining damage for in-service panels, which may lead to more confidence and less conservatism when applying structure dent limits.
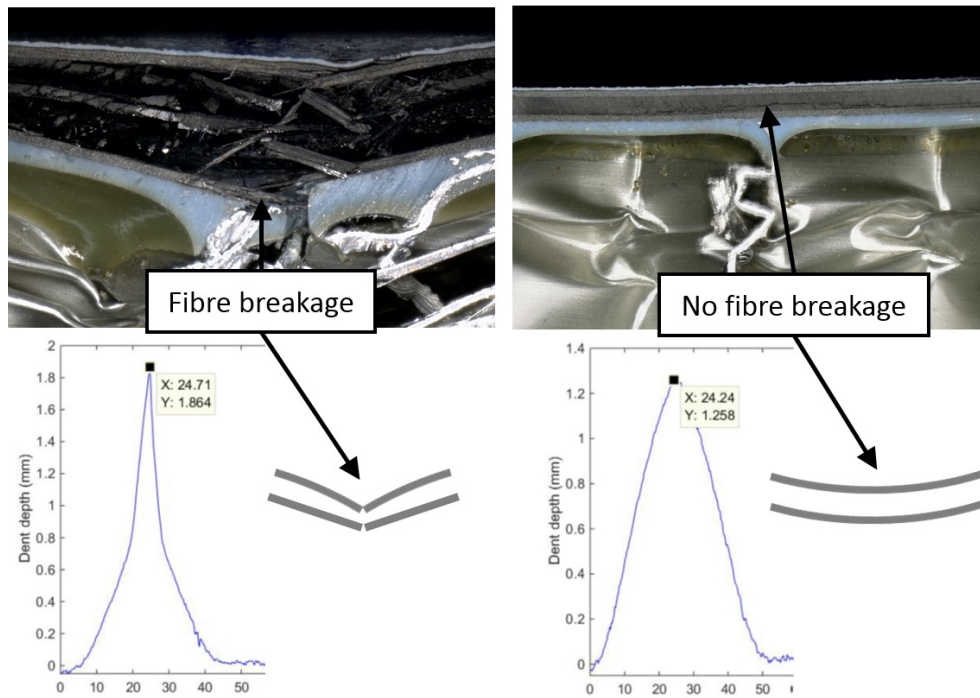
Figure 4.33: Impact failure mode and laser topography curvature for B11 12.7 mm (left) and 25.4 mm impactors (right). The sharper profile on the left may be indicative of significant laminate damage, and may be useful for characterization of impact damage.

Sources of Error

Sources of error include difficulty in micrometer measurements, determining an appropriate threshold for dent diameter for laser topography and contact time damage threshold for the C-scan tap test, ultrasound threshold, as well as impact energy variation. Furthermore, while this experimental study has the advantage of exploring unique geometries and features that are difficult to duplicate with coupons, it lacks the ability to be repeated due to a limited number specimens, and therefore these results are trends and not definitive statistical relationships that can be applied to all sandwich panels.

4.2 Study 2 - Damage characteristics for repaired versus regular panels

This study focused on how damage from low-velocity impact differed between a repaired panel and a regular panel. The stiffness at a repair patch is higher than a regular panel due to increased thickness, but there are factors that may influence the failure mode or the detectability of damage from additional materials such as potting compound and foaming adhesive, additional plies, and challenges with performing a proper repair (e.g. ensuring that the repair patch is well bonded to the underlying sandwich panel) .

The study was performed by impacting the same locations on two otherwise identical panels. Figure 4.34 shows the two panels, and the impact locations: one impact was on the edge of the ramp of the repair, another in the middle of the repair[1], and a third hit just outside the repair patch. These impact sites are identified as zone 1, 2 and 3 respectively for the regular and repaired panels.

These panels were of similar basic construction to the B11 panel consisting of 5-ply facesheets. All impacts were performed at ∼5 J with a 25.4 mm steel impactor. Other panel parameters are noted in Table 4.9. Note that zone 1 has a 3.1 pcf density core, and zone 2 and 3 have 2.3 pcf core.

Table 4.9: Parameters for panel E3 and E3R

Parameter	Units	Value
Laminate Thickness	µm	650
Core Density	pcf [kg/m^3]	$2.3 - 3.1$ [$36.8 - 49.7$]
Core Thickness	mm	14 - 32

---

[1]This is as close to the center of the repair as can be achieved by the fixture, which requires a minimum of 2.5 in from any edge in order to be properly supported.

Figure 4.34: Repaired (a) panel E3R with patch and (b) regular panel E3. For the repaired panel, zone 1 is along the edge of the repair where the plies and thickness begin to taper off, zone 2 is in the center of the repair where there is increased effective facing thickness of the patch/panel combination, and zone 3 is just outside the repair patch.

4.2.1 Force-Time Comparison

The regular and repaired panel force-time histories are compared for each zone location, to show the differences in peak load, stiffness and to provide insight into possible failure modes. This force-time comparison shows that a repaired panel performs differently from a regular panel when subject to low-velocity impact.

Figure 4.35 shows zone 1 at the edge of the repair. The impact on the regular panel results in a lower constant peak load indicating possible crushing of the core. The repaired panel reaches a higher peak load, and has a shorter contact time (i.e. the duration of the force curve), which follows the trend of a thicker and stiffer facesheet.

Figure 4.36 shows zone 2 at the center of the repair. The regular panel has a contact time of ∼11 ms and reaches approximately the same peak load of 2400 N as the regular panel as seen in Figure 4.35, however the peak load shape is different when compared to the zone 1 impact. The trend for the repair patch is also similar, however yielding may occur slightly later during

87
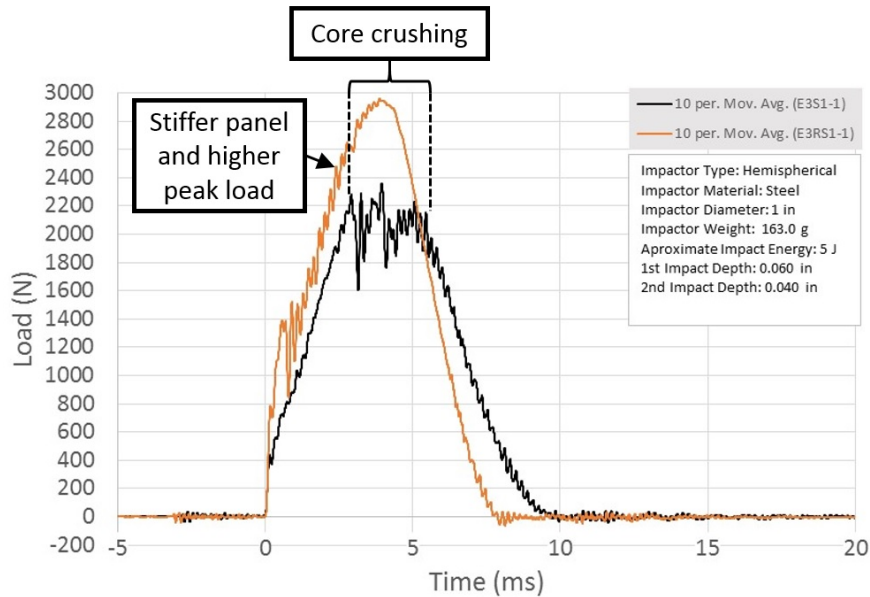
Figure 4.35: Comparison of repaired (orange trend-line) and normal (black trend-line) panel force time curve for zone 1 impact. Peak load for the repaired panel is higher when compared to the regular panel and contact time is shorter (i.e. higher local stiffness) which is consistent with thicker facesheets. A constant peak load for the regular panel may indicate core crushing.

the impact event.

Note that contact time is slightly higher for the zone 2 regular panel, indicating a stiffer location. The load at which core is crushing is also different between the two panels (i.e. zone 1 is crushing at 2000 N whereas zone 2 is crushing at 1700 N). These differences are reasonable, since the zone 2 core is lower density than at zone 1. Figure 4.37 shows the difference for the zone 1 and zone 2 core crush load. When brittle failure of the facesheet occurs, there is a constant load similar to that of unsupported core; unsupported high density core has a higher core crush load than low density core.

Figure 4.38 shows the zone that is outside of the repair patch area, and appears to have similar impact characteristics (e.g. peak load and contact time) to the regular panel, which is as expected. The repair has a longer contact time, which may indicate it has incurred more damage than the regular panel. Note that the repaired panel has a core crush load comparable to the regular panel for zone 2 as it is the same core density. The regular panel of
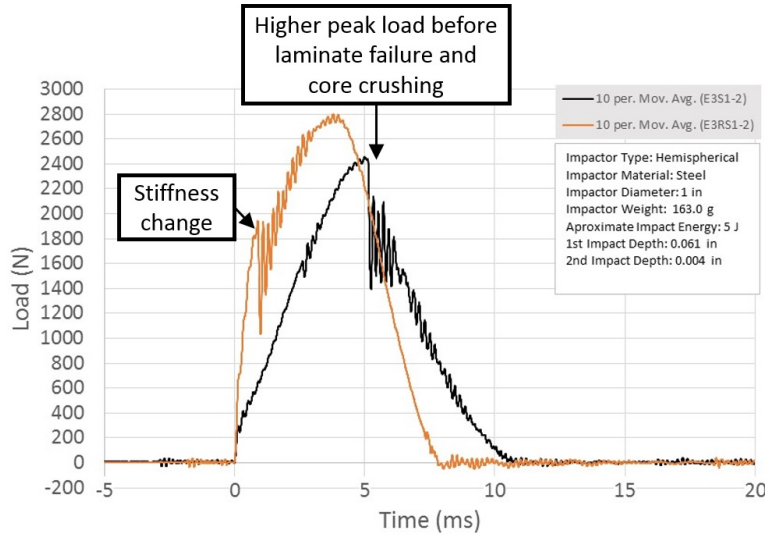
Figure 4.36: Comparison of repaired (orange trend-line) and regular (black trend-line) panel force time curve for zone 2. There is an early stiffness change for the repaired panel, however it reaches a similar peak load to the zone 1. The regular panel achieves a higher peak load before a short constant load, indicating the core absorbing the impact.
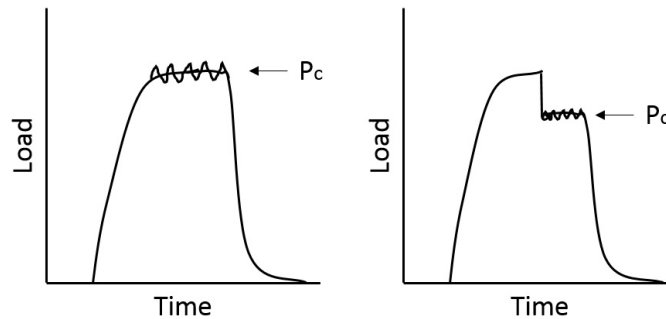
Figure 4.37: Comparison of force-time core crush load (P_c) for the regular panel from zone 1 higher density core (left) to zone 2 lower density core (right). Once a brittle failure of the facesheet occurs, the loading is typically stable compression of the core, absorbing impact energy and deflecting.

89
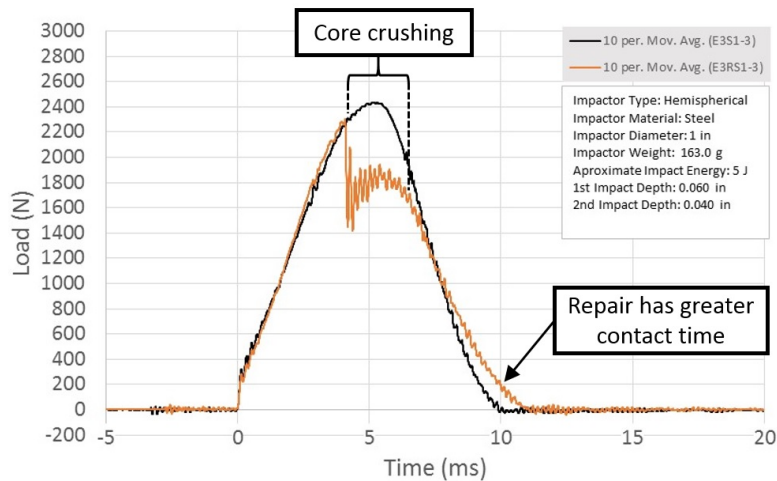
Figure 4.38: Comparison of repaired (orange trend-line) and regular (black trend-line) panel force time curve for zone 3. The repair has a longer contact time, which may indicate it has incurred more damage than the regular panel.

zone 3 does not experience a brittle fracture, but it does achieve the same peak load as the regular panel in zone 2.[1]

4.2.2 Visual Inspection and Dent Depth

Figure 4.39 shows the regular panel following impact. All impact damage was visible.[2] Figure 4.40 shows the repaired panel; while the zone 1 and zone 3 impacts were detectable, the zone 2 impact in the middle of the repair patch was not noticeable. Table 4.10 shows the dent depth micrometer measurements for both panels. The regular panel dent depths were comparable. The edge of the repair provided some additional dent resistance when compared to the regular panel, the center of the panel showed almost no indentation at all due to additional stiffness of the patch, and outside the repair patch the impact led to even greater dent depth than that of the regular panel.

---

[1]Without the brittle facesheet failure the constant core crush load in the force-time history is not seen, but this does not mean that there is no core damage occuring.

[2]Being able to see the impact locations is expected since this panel is similar in nature to B11; because a higher energy level was used, the impact should have led to a larger dent and have been more detectable.
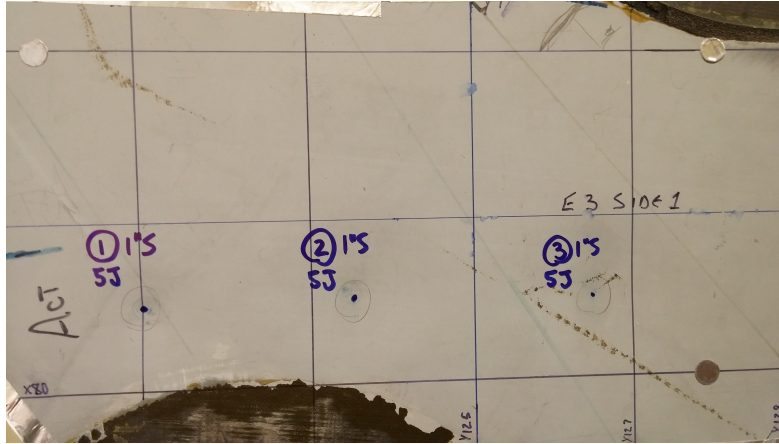
Figure 4.39: E3 post-impact with all dents visible.
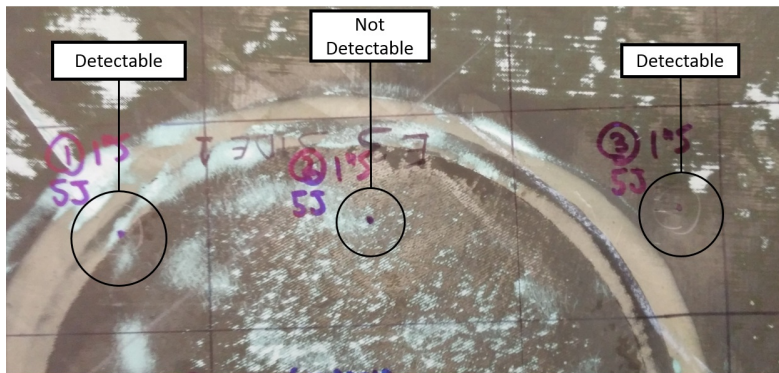
Figure 4.40: E3R post-impact with zone 1 and 3 impacts visible, but zone 2 was not visually detectable.

Table 4.10: Dent depth micrometer readings for 25.4 mm impactor at ~5 J

Panel	Zone 1 Depth (mm)	Zone 2 Depth (mm)	Zone 3 Depth (mm)
E3	1.52	1.55	1.52
E3R	1.02	0.10	2.03

4.2.3 Dent Shape and Diameter

This section will present the laser topography images to provide a qualitative sense of the shape and diameter from the impacts on each panel.
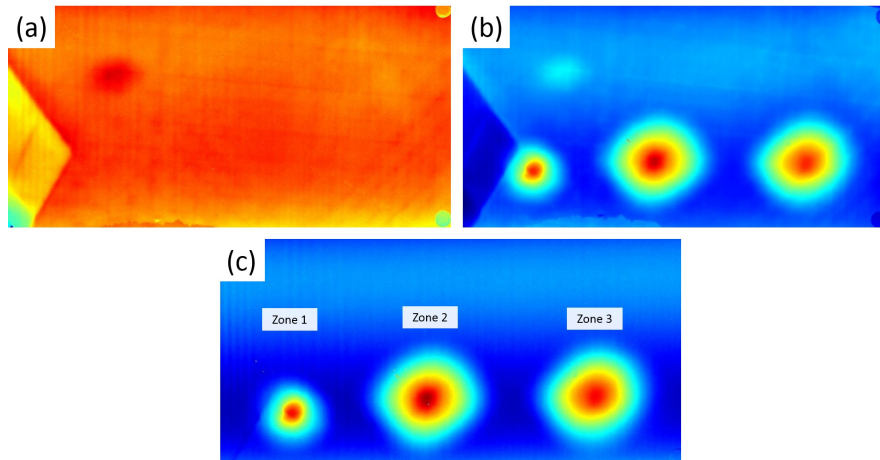
Figure 4.41: E3 (a) before impact, (b) after impact, and (c) deviation map showing smaller zone 1 dent diameter when compared to the other impacts. All impacts 5 J performed with 25.4 mm impactor.

Figure 4.41 shows the topography map for the regular panel before impact, after impact, and the deviation map between these scans. The zone 1 impact as seen in Figure 4.41 (c) has a smaller diameter than the other two impacts, since this zone is higher density core than on the other side of the splice as seen in Figure 4.42 (b).

Figure 4.43 (a) shows the topography map for the repaired panel before impact, (b) after impact and (c) the deviation map of the scans subtracted from one-another. The center impact is obscured (Figure 4.43 (b)), however even though the impact is barely identifiable, the zone 2 (center) impact is still detectable due to a very slight change in the surface when using the deviation map (Figure 4.43 (c)).
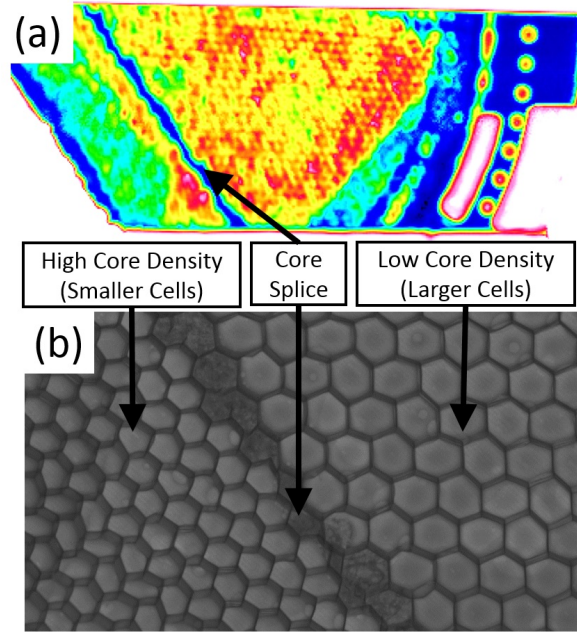
Figure 4.42: (a) Ultrasound and (b) X-ray of E3 core cell geometry showing core splice, higher and lower density core.
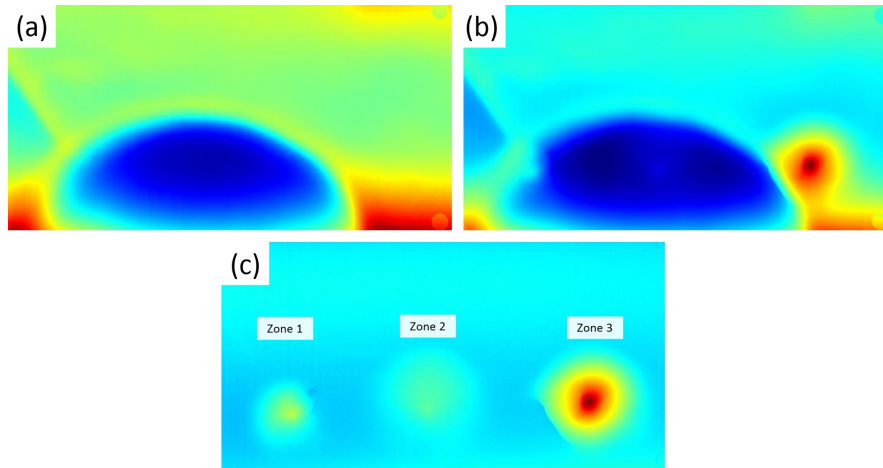
Figure 4.43: E3R (a) before impact, (b) after impact, and (c) deviation map showing faint depth profile for zone 1 and a barely noticeable depth profile for zone 2 when compared panel E3 topography.

4.2.4 Cross-section and Failure Mode

This section will describe the difference in damage and failure mode observed between impact on the regular panel and the repaired panel.

The damage cross-sections for E3 and E3R zone 1 are shown in Figure 4.44. E3 has significant laminate damage, facing-to-core bond damage as well as core crushing, whereas E3R has less damage, but still delamination, core crushing and the potting compound is cracked. With the combined thickness of the facesheet, patch and potting compound the laminate appears to have absorbed more of the impact energy as the core is less crushed when compared to E3.
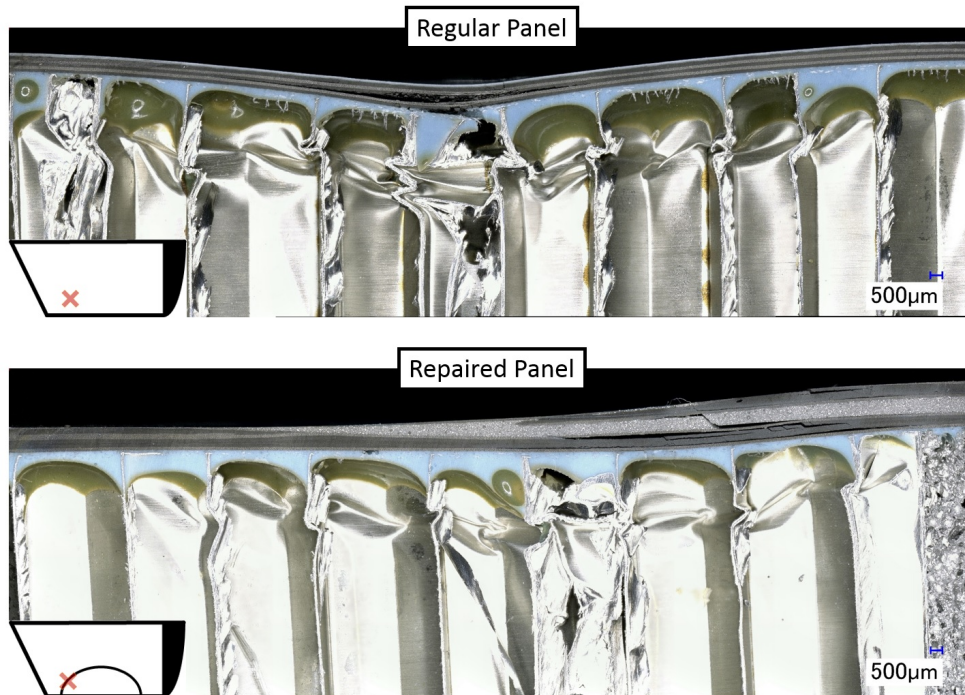
Figure 4.44: Regular (E3) and repair (E3R) panel zone 1 cross-sections. E3 has incurred significant laminate damage, delamination, adhesive cracking and core crushing. The E3R impact occurred at the edge of the repair patch, and caused delamination and shear cracking in the laminate, cracked potting compound and core crushing. Location on panel noted at bottom-left corner of cross-sections.

Damage cross sections at zone 2 for E3 and E3R are shown in Figure 4.45.

E3 appears to have less laminate damage than zone 1. This is likely due to the lower core density at this location.[1] More of the impact damage is absorbed by the lower density honeycomb core.
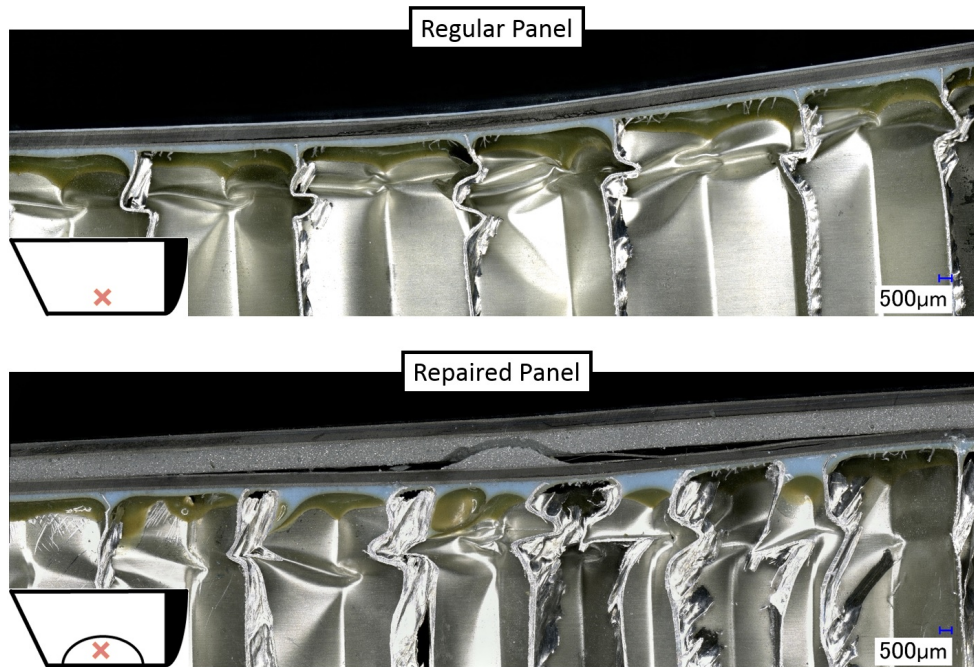
Figure 4.45: Regular (E3) and repair (E3R) panel zone 2 cross-sections. E3 has some laminate damage and a delamination extending between the fourth and fifth ply, as well as some core crushing. E3R shows core crushing along with some delamination at both the upper and lower ply, as well as a significant crack in the potting compound between the patch laminate and the underlying panel laminate. Location on panel noted at bottom-left corner of cross-sections.

Zone 2 on the repaired panel is of interest: even though there was only slightly measurable indentation caused by the impact, the underlying damage was significant. Figure 4.46 shows multiple modes of failure: delamination, potting compound fracture and core crushing are all present under the BVID.

---

[1]Core density may be difficult to determine when looking at the cross-section or side of a cut panel; since orientation of the core (i.e. ribbon direction) changes throughout engineered panels, the apparent size of the honeycomb cells may appear to change when only a change of orientation has taken place.

The facesheet laminate has some delamination initiating, and the repair patch has a delamination starting underneath the second ply, which has a reverse pine-tree fracture, causing delamination in the lower plies as is characteristic of thick laminates [18]. Voids appear to be present in the repair patch, which may weaken or lead to a more easily damaged laminate as these locations may act as local stress raisers and possibly be initiation sites for delamination or crack growth.
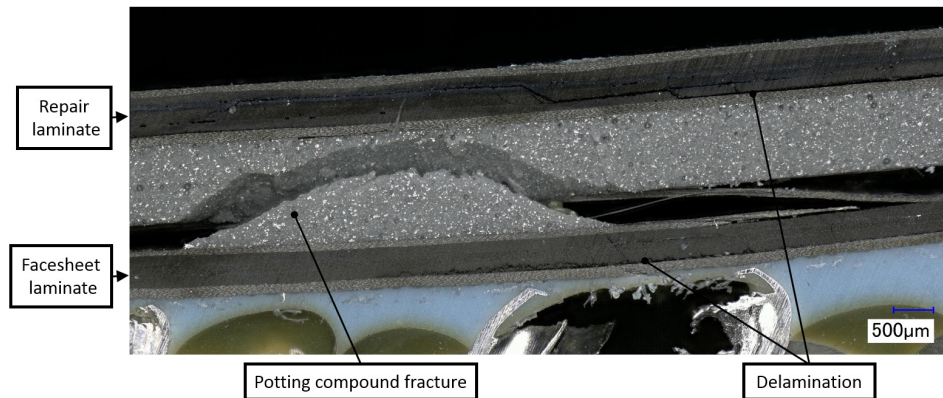
Figure 4.46: E3R zone 2 delamination and damaged potting compound.

Figure 4.47 shows zone 3 for panel E3 and E3R. E3 has less delamination at zone 3 than at zone 2, but is otherwise comparable. Zone 3 is located just outside of the repair patch. The impact site is towards the right of the cross-section, which shows significant laminate damage, delamination, as well as core crush. Due to the large deflections outside of the repair zone, this led to cracking of the potting compound that is smoothed towards the edge of the repair.
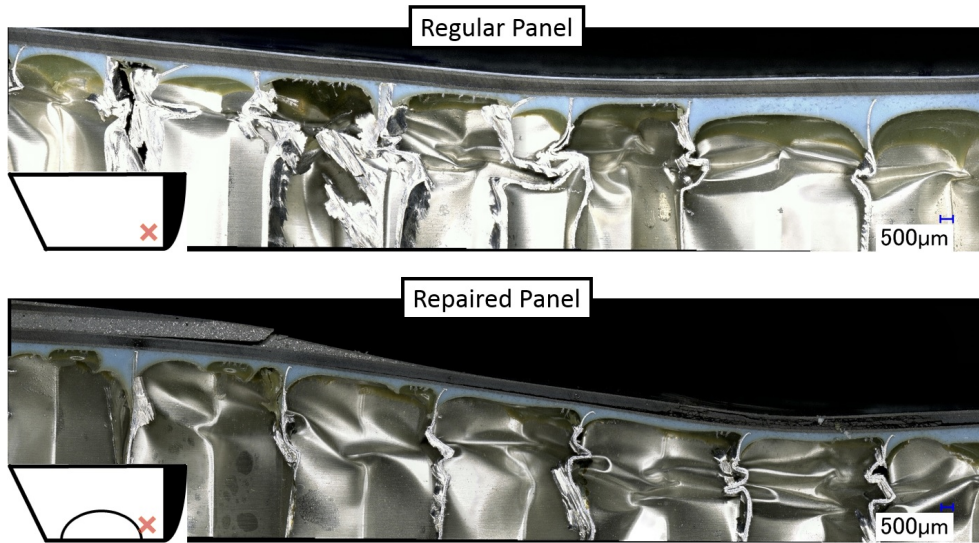
Figure 4.47: Regular (E3) and repair (E3R) panel zone 3 cross-sections. E3 has delamination between the fourth and fifth ply, as well as core crushing. E3R has more significant laminate damage as well as delamination, with a crack in the potting compound at the left side of the cross-section where the repair ends. E3R also has more core crush than E3. Location on panel noted at bottom-left corner of cross-sections.

Table 4.11 provides a summary of the laminate damage depth measured from the impact zone cross-sections. Comparing this internal damage to Table 4.10, it is important to note that while the dent depth measurement was the smallest of all the dents at 0.10 mm for E3R zone 2, the internal laminate damage depth was the greatest of all the impacts. Laminate damage depth (δ_{damage}) is defined as:

$$\delta_{damage} = t_{impactzone} - t_{undamaged}$$

where $t_{impactzone}$ is the thickness of the laminate measured at the point under the impact location and $t_{undamaged}$ is the undamaged laminate thickness. Figure 4.48 defines where the measurements are taken; essentially, laminate damage depth is the maximum separation of all the laminate plies.

Table 4.11: Laminate Damage Depth at Zone Locations

Panel	Zone 1 Damage (μm)	Zone 2 Damage (μm)	Zone 3 Damage (μm)
E3	361	45	35
E3R	151	510	161
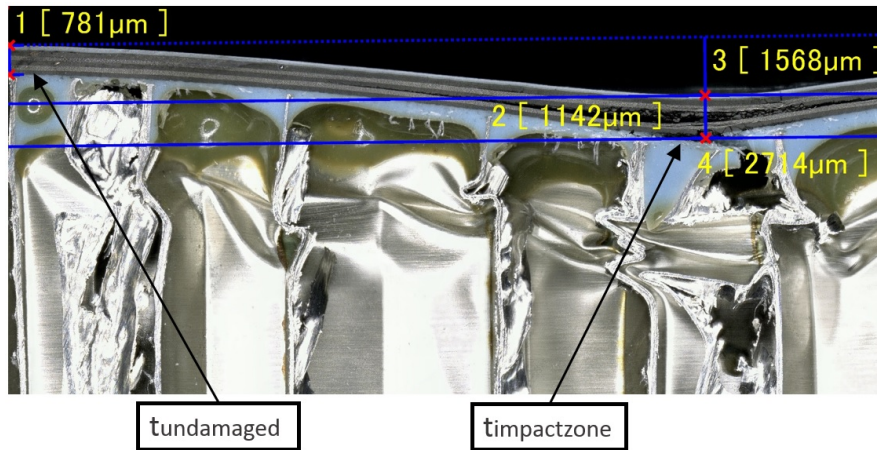
Figure 4.48: Definition for laminate damage depth calculation.

4.2.5 Discussion

Comparison of Damage

The impact depths for the regular panel were approximately all the same and all impacts were detectable. On the repaired panel, impact depths were varied as seen in Table 4.10. The zone 1 E3R impact was on the edge of the repair patch and led to a slightly reduced dent depth due to the additional laminate thickness. The zone 2 dent in the center of the panel was not visually detectable and did not have significant depth; reduced dent depth is expected since the effective laminate thickness at this location is much greater than the regular panel. Zone 3 was just outside of the repair patch, and this led to an increased dent depth and laminate damage when compared to the regular panel. The repair provided a stiff boundary condition on one side of the zone 3 impact site when compared to the regular panel that may have contributed to the result of increased dent depth and damage, however this does not

explain why the force-time curves for the impact event were so similar as seen in Figure 4.38. Additional testing would have to be performed to help to determine if the presence of a nearby repair leads to a reduced ability to resist impact.

For the regular panel, zone 1 incurred more significant laminate damage than the other zones. This is because while the impact energy was the same, the core at zone 1 is higher density than zone 2 or 3; the stiffer zone 1 core absorbs less of the impact, leading to increased damage in the facesheet. The zone 1 impact for the repaired panel incurred less damage than the regular panel.

For the repaired panel, zone 2 incurred laminate damage similar to the regular panel, however the compound bonding the patch to the surface of the composite has cracked, allowing the patch to spring-back and hide the damage (Figure 4.45). This could be a significant problem if the patch is acting as a splice: fatigue may grow the separation between the repair patch and the structure and the damage would not be detectable on the surface; separation between the patch and the panel would lead to it no longer redistributing the load across the damaged area if the patch is structural. External cracking may lead to water ingress which may exacerbate the problem by reducing the static strength of the panel, accelerate fatigue or may lead to aeroelastic issues such as flutter which may cause failure of the panel. This means that careful selection of the bonding material is required for a repair in order to ensure damage resistance, and repair locations may require periodic inspections to ensure there are no issues.

Based on the cross-sections of the repaired panel (i.e. lack of a core plug) and the bonding compound cracking, the repair may be non-standard. Furthermore, it is likely the repair is aerodynamic rather than the structural example seen in Figure 2.19. A tougher bond material (similar to the epoxy used for the facing-core bond) would be used in structural applications which is much less likely to crack or disbond. Assuming the patch is used as part of a "fill and fair" repair (meaning the patch exists for aerodynamic purposes rather than structural) this is still an issue. The underlying facesheet that carries load has been compromised, but may go undetected underneath the cosmetic patch. In either case, this means that additional caution is required for structural and non-structural repairs. The ideal course of action is periodic subsurface NDI (not visual) of patches for possible damage or damage growth throughout the service life of the structure.

Force-Time Curves

The early stiffness change seen in Figure 4.36 for the repaired panel may indicate failure of the bond between the patch and the underlying panel. This stiffness change is also apparent in Figure 4.35 where the impact occurred on the edge of the repair, and is non-existent for the regular panel or the zone 3 impact on the repaired panel, which took place just outside of the patch.

Sources of Error

Sources of error include dent depth measurements due to the uneven surface of the repair patch, small differences regarding how the repaired panel seated in the drop tower fixture compared to the regular panel, differences in panel construction and the assumption that the repair patch was completed properly (e.g. no repair defects, correct curing performed, proper materials used, etc).

4.3   Study 3 - Evaluation of C-scan tap test

An in-house NDI method was developed simulating the theory and basis of the Computer-Aided Tap Test (CATT) that was developed at Iowa State university [51], and will henceforth be called the C-scan tap test. The C-scan tap test was used to substantiate the measurement of local contact time across the damage area as a simple, low cost method of detecting damages internal to a sandwich composite. The results will be compared against two other common NDI methods: through-transmission ultrasound and radiography.

Five panels with varying facesheet thickness and core densities were impacted at energy levels ranging from 3–15 J to determine if the C-scan tap test method of inspection was reliable for detecting damage for varying panel types and impact characteristics. Panel B11 was used to study varied impactor diameter, D21 looked at impact at a septum and the use of both steel and nylon blunt impactors, F3 looked at a panel with higher density core and thicker facesheets, E3 and E3R compared impact on a repair patch and a regular panel. Panel properties are listed in Table 4.12 and parameters for the impacts are listed in Table 4.13.

Table 4.12: Panel Properties

Panel	Facesheet Thickness (µm)	Core Density (kg/m³)
B11	650	36.8
D21	650	36.8 [1]
E3	650	36.8, 49.7 [2]
E3R	650 [3]	36.8, 49.7 [2]
F3	3271	49.7, 84.9 [4]

[1] A strap at the septum midplane increased the stiffness of the panel.

[2] First impact at the location of higher density core (refer to Figure 4.42).

[3] Thickness at repair is greater than noted (refer to section 4.2.4).

[4] Two impacts at each location of core density.

Table 4.13: Parameters of C-scan Tap Test Impacts

Panel	Impactor Diameter(s) Used [1] (mm)	Target Energy Level (J)
B11	12.7, 15.9, 25.4, 79.8	3
D21	25.4	15
	25.4, 79.8 Nylon, 79.8	5
E3	25.4	5
E3R	25.4	5
F3	25.4	15

[1] All impactors made of steel unless otherwise specified.

4.3.1 Panel B11

The results for panel B11 is covered in section 4.1.3. The C-scan tap test effectively found the damages, and using a specified threshold contact time the approximate damage diameter could be approximated.

4.3.2 Panel D21

Panel D21 is a trailing edge specimen that was impacted at five locations as shown in Figure 4.49. Some unique internal details of the specimen are seen in Figure 4.50. The first impact was a 15 J impact with a 25.4 mm steel

impactor on the trailing edge (higher energy was used since it was known that this area was stiffer due to a septum that provides additional rigidity). The second impact was also 15 J with a 25.4 mm steel impactor on the core splice which divides the trailing edge from the remainder of the sandwich panel. All other impacts were 5 J impacts with a 25.4 mm steel impactor, 79.8 mm nylon impactor and 79.8 mm steel impactor respectively. The larger impactors were chosen to see if blunt impactors could be identified.
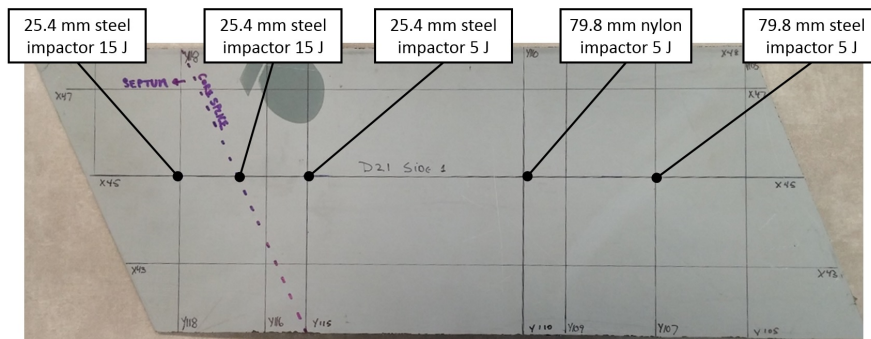
Figure 4.49: D21 impactor type and energy level. Higher impact energy was used at septum and core splice because these locations have higher impact resistance. Different impactor materials were used for the blunt impactors to see if this had any effect on damage or detectability.

Figure 4.51 shows the radiographic image of the damaged panel. This appears to be the most difficult method to detect damage of the three studied. Cracks in the laminate can be detected by this method, and core crushing will show up as a shift in the pattern of the honeycomb cells from the surrounding cells. Careful analysis is required to detect damages with radiography.

Figure 4.52 shows the through-transmission ultrasound of D21. This shows three of the impacts quite clearly, but due to the additional thickness of the core splice and higher density trailing edge, two of the impacts are obscured and were not detected by this method.

Figure 4.53 shows the C-scan tap test method; this method clearly shows four of the five impacts; the impact at the core splice blends in next to the other damages which experience more significant core crushing, which has a larger affect on contact time than delamination alone.
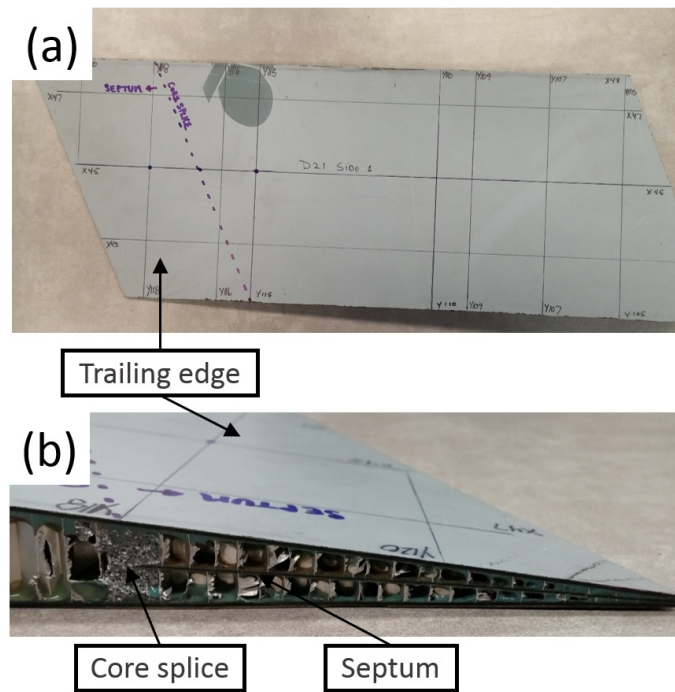
Figure 4.50: Trailing edge of panel D21 noting septum (to provide additional rigidity) and core splice.
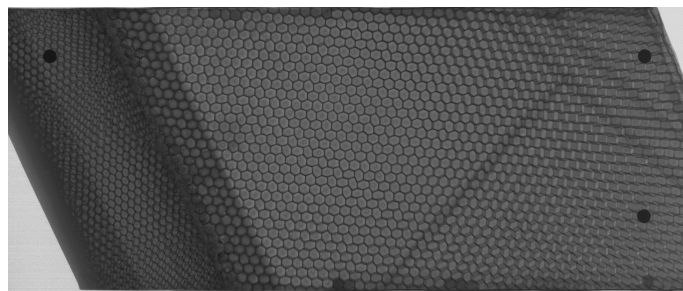
Figure 4.51: D21 after impact radiographic image. Shifting in cells reveals core crush, however it is challenging to identify impact with this method.
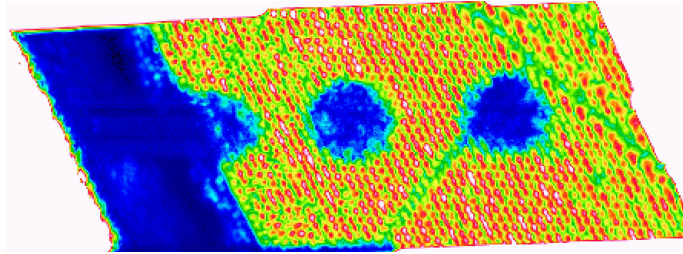
Figure 4.52: D21 after impact through-transmission ultrasound. Higher density septum on the left of the panel obscures damage for two of the five impacts.
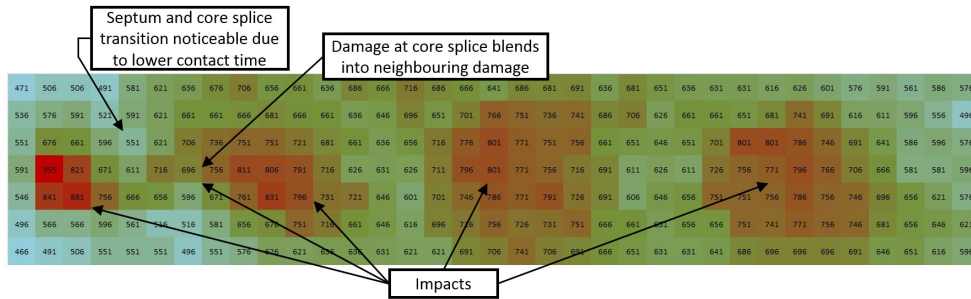
Figure 4.53: D21 after impact C-scan tap test. Four damages clearly identifiable with core splice impact blended into adjacent damage. Septum is the area of lower contact time.
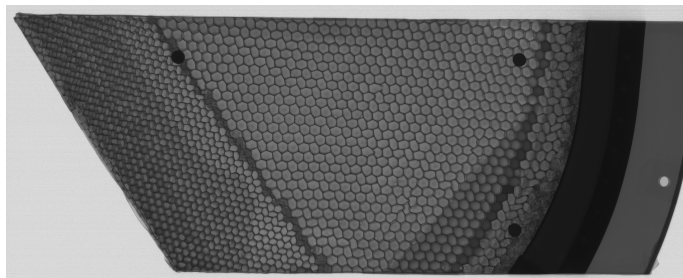
Figure 4.54: E3 after impact radiographic image

104

4.3.3   Panel E3

Panel E3 was the baseline regular panel used for the study in section 4.2 comparing impact on a repaired and regular panel. In the context of this study, the differences in damage detectability for the NDI techniques will be compared.

Relative dent diameter sizes from laser topography can be seen in Figure 4.41. The regular panel had a small diameter zone 1 dent and roughly equal zone 2 and 3 dents.

A radiographic image of panel E3 is shown in Figure 4.54 with some close inspection reveals core crushing due to warpage at the impact locations, but as with the previous panel this method does not detect damages from impact as well as ultrasound or C-scan tap test.

Figure 4.55 shows the through-transmission ultrasound of E3. This clearly shows the areas of damage, and reveals that the first impact has a smaller diameter than the other two. The reason for the leftmost (zone 1) impact having a smaller damage diameter is due to the higher density core at this location.
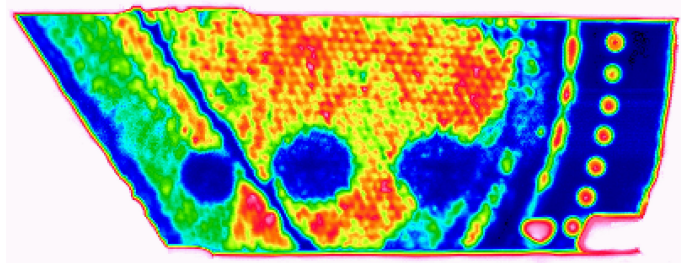
Figure 4.55: E3 after impact through-transmission ultrasound

Figure 4.56 shows the C-scan tap test method of inspection. Like ultrasound, this method was able to detect the impacts and relative damage size.

4.3.4   Panel E3R

Panel E3R was the repaired panel used for the study in section 4.2 comparing impact on a repaired and regular panel. This study will determine if there is a difference in damage detectability for the NDI techniques with the added repair patch.

Relative dent diameter sizes from laser topography can be seen in Figure 4.43 (previous study). The repaired panel had a small diameter zone 1
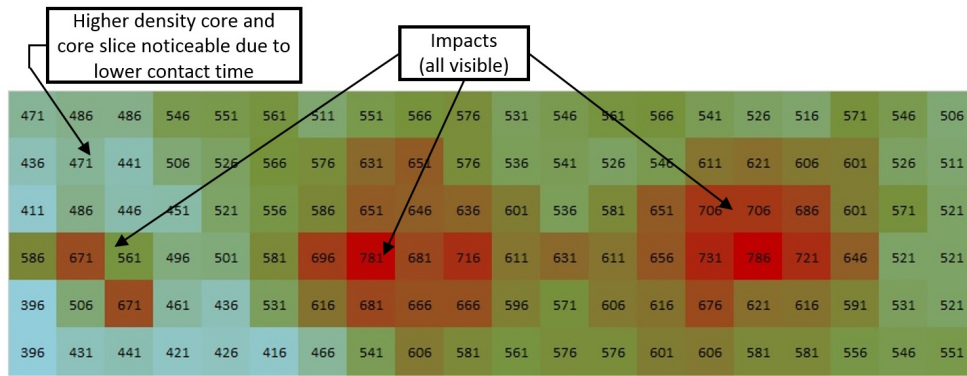
Figure 4.56: E3 after impact C-scan tap test. Higher core density, splice and impacts identified.

dent, a almost undetectable zone 2 dent and a zone 3 dent comparable to the regular panel.
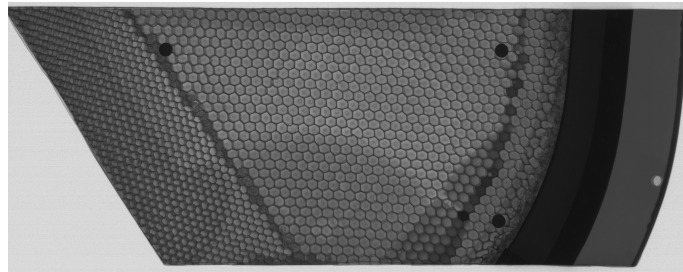
Figure 4.57: E3R after impact radiographic image

Figure 4.57 shows the radiographic image of panel E3R. It is very difficult to identify the damaged areas for this panel using this technique. Figure 4.58 shows the through-transmission ultrasound of E3R. All impacts and their respective sizes are easily detected, and the repair patch and splice are seen using this method.

Figure 4.59 shows the C-scan tap test method of inspection. All impacts are identified with this method, and the core splice and repair patch are noticeable by changes in contact time. While this method provides details about changes to local stiffness over the surface inspected, noting of splices, patches and other panel features by the engineer is important so that discontinuities

106
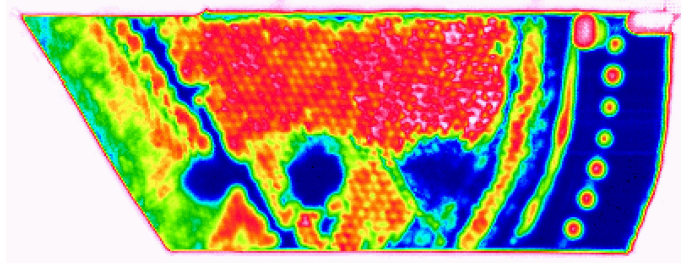
Figure 4.58: E3R after impact through-transmission ultrasound

can be identified as damage, or elements that are characteristic of the undamaged panel.
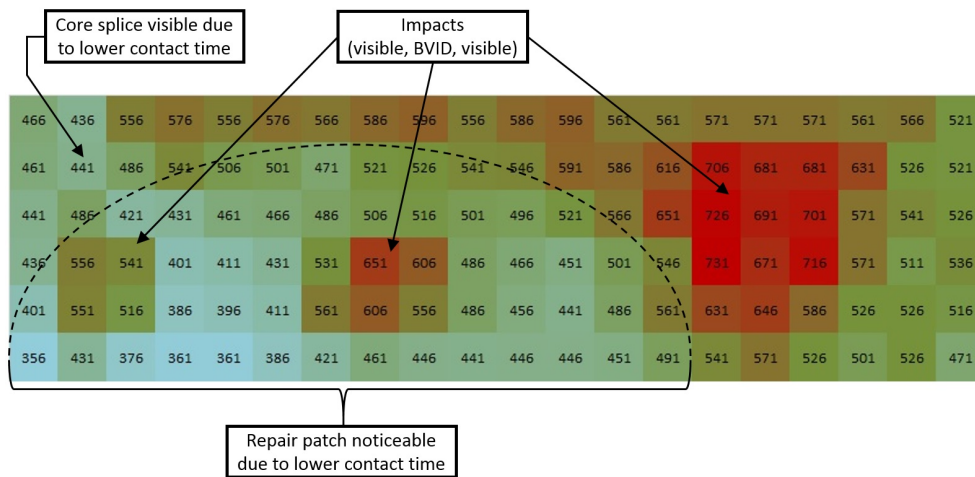
Figure 4.59: E3R after impact C-scan tap test. Core splice, repair patch and impact locations noted.

4.3.5   Panel F3

Panel F3 has thicker facesheets than the other panels studied and was used to observe if this had an effect on the ability of the C-scan tap test to detect damage. The panel has a core splice through the center, and two different core densities on either side. Four 15 J impacts were performed with a 25.4 mm

steel impactor (two impacts on each side of the core splice). All damages were less than 0.5 mm deep (BVID) measured with the micrometer.
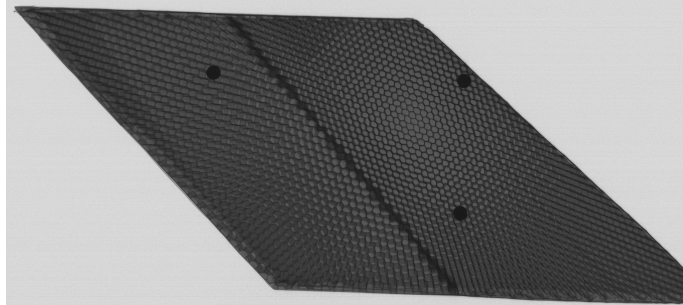
Figure 4.60: F3 after impact radiographic image
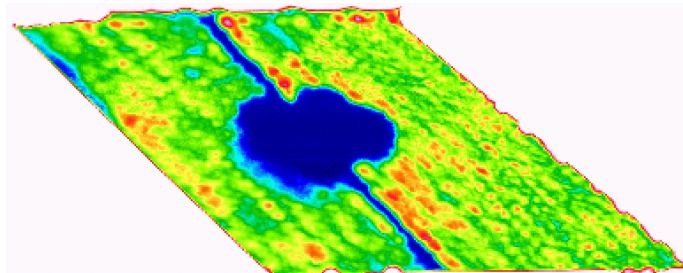
Figure 4.61: F3 after impact through-transmission ultrasound

Figure 4.60 shows the radiographic image of the panel, with the different core sections and core splice running down the middle. It is difficult to detect core crushing in this image. Figure 4.61 shows the ultrasonic scan of F3, and although there were four impacts, their proximity has made damages blend into one large damage area. The higher density core on the right-hand side leads to less dispersion of damage. Figure 4.62 shows the C-scan tap test of the panel; the result is very similar to the ultrasound, with the damages blending into one central area of stiffness loss for the panel. Lower contact time areas correctly identify the core splice location.
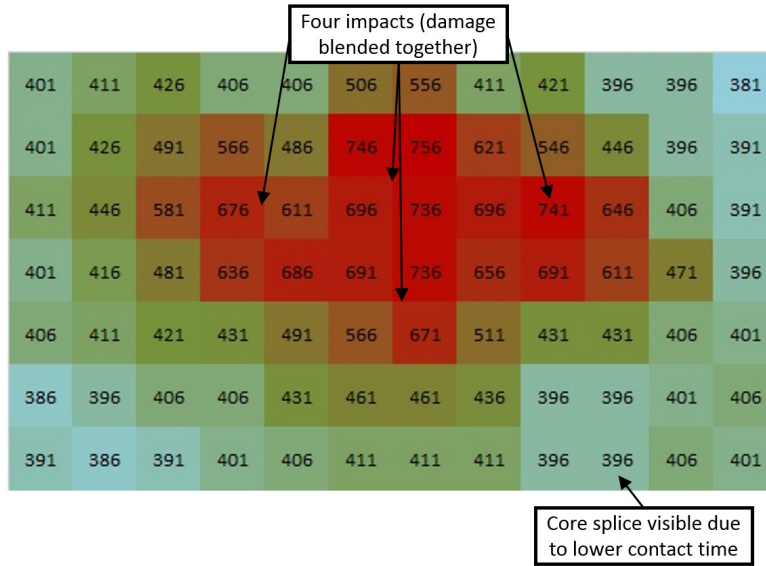
Figure 4.62: F3 after impact C-scan tap test. Four BVID impacts and core splice noted.

4.3.6 Contact Time and Underlying Damage

It was found through contact time measurements of the damage incurred under the impact zone that there is a relationship between this damage and the decrease in stiffness. Contact time increases with local stiffness decreasing which relates to the amount of damage incurred. Impacts at 3 J for panels with equivalent facing thickness and core density were studied to see if the C-scan tap test could provide some indication of failure mode, or the extent of the failure caused by the impact. Figure 4.63 shows a trend of increased contact time with more significant underlying core crush (with the exception of one data point). It is difficult to ascertain if there is a noticeable pattern with laminate damage.
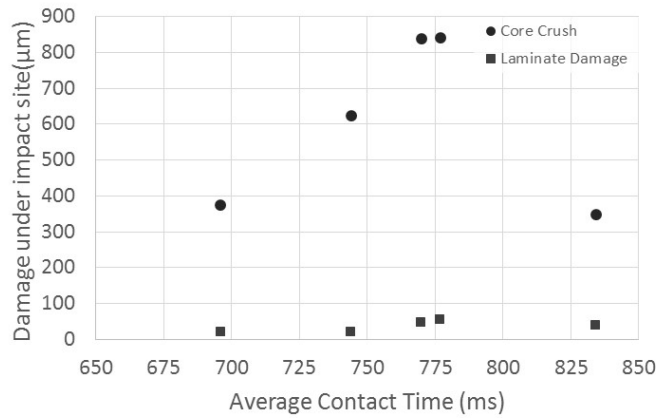
Figure 4.63: Damage at the impact zone (measured when sectioned) against contact time. Core crush increases with contact time.

4.3.7   Repeatability

Figure 4.64 shows the C-scan tap test for the panel E3R, repeated to show the degree of variation that can occur between repeated tests. In both cases (a) and (b), the impact areas are all identifiable, showing a local loss of stiffness as greater contact time than the surrounding area. Figure 4.64 (c) shows the difference between two repeated tap tests of panel E3R. Note that for undamaged areas, the variance is not as significant as for the damaged areas. The tap test confirms some details about the first impact on the panel (leftmost impact). The change in local stiffness is less for this 5 J impact, since the surrounding area is a stiffer (light blue area). This indicates that the core is stiffer, and higher density than the remainder of the panel. Looking at an area with less stiff surroundings, such as the third (rightmost) impact, the damage is spread out over a greater area as a result of the lower density core.
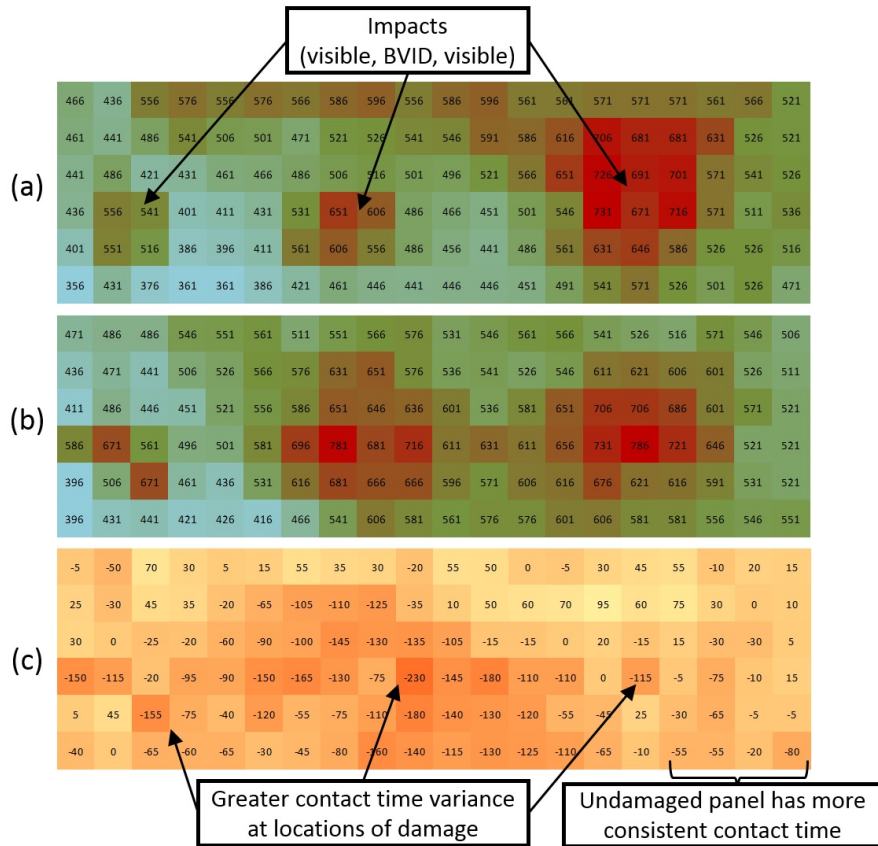
Figure 4.64: E3R C-scan tap test showing (a) first scan, (b) second scan and (c) the difference between the two scans. The difference between the C-scan tap tests shows greater variability when impacting a location of damage.

4.3.8   Discussion

Detection Comparison

The C-scan tap test successfully detected BVID and visible impact damage on a selection of panels. Out of the 19 impacts on the various panels studied, the C-scan tap test easily detected 18, while ultrasound easily detected 17 and radiography did not easily detect any of the damages, although a skilled technician could detect some of the damage using radiography. Careful analysis of the C-scan tap test would have revealed the last impact damage location for panel D21, and performing an additional scan using ultrasound for the septum

111

area of panel D21 would have likely revealed the remaining two damages.

One of the challenges associated with the C-scan tap test is that the edges of the damage area are not specified, whereas ultrasound provides a clear damage zone; preliminary stiffness testing of undamaged components would be best in order to implement this method in the field, whereby a damage threshold could be applied to zones of the structural component. Knowledge of the underlying structure is beneficial when using this method, since core splices, core density changes, and facing thickness will all affect the relative stiffness of this method. However, even without knowledge of the structure, this method appears to detect impact damages well, and should be able to detect damage near the BVID threshold that would lead to a change in the local out-of-plane stiffness.

Advantages of the C-scan tap test when compared to ultrasound and radiography is that it is low cost, easily made portable, fairly easy to use and requires limited operator skill. Some of the disadvantages are that the method has potential to damage the panel if excessive force or incorrect tap hammer tip was used, the method would require some programing to be faster and ideally utilize a scanning cart similar to the CATT. The method was not tested on very thick laminate panels, and likely would not detect core fatigue, fluid ingress, corrosion or very minor cracks in facesheets (which may be more suitable for the other methods). Overlapping multiple NDI methods is most suitable when performing a detailed inspection of a component, especially when the damage type may be unknown to the operator.

Panel Stiffness and Failure Modes

As seen in Figure 4.63 as panel stiffness decreases due to impact damage, contact time increases with measured cross-section core crushing. No definitive relationship is detectable between observed laminate damage and contact time; crushed core has a greater influence on local stiffness reduction than laminate damage.

Due to the different geometries, supporting conditions of the fixture, inexact nature of the cross section measurements and lack of statistical repetition, it is difficult to conclude if the tap test can differentiate between failure modes. A more diverse set of examples would be required to see if this NDI method could be used to differentiate between only laminate damage and core crush.

Sources of Error

Sources of error include variation of force for taps, the angle of incidence of the tap, exact tap location relative to the positioning grid and panel support boundary conditions. Repeated tests did show repeatable detection of impacts, however there was variance in the contact time, especially near damaged locations as seen in Figure 4.64; this variance may be an inherent error in the test, or it may be an exploitable feater for testing out-of-plane stiffness that may aid in damage detection.

4.4 Study 4 - Dent Relaxation

This study investigated how dent depth and profile changed over time for a sandwich composite. Significant reduction in the dent depth and profile over time can be problematic as it may conceal underlying panel damage that had taken place. This study looked at relaxation starting at 3 hours after impact.

The panel selected for the dent relaxation study was B12, which was similar to B11: it has a five-ply facesheet, and a 36.8 kg/m^3 low density core. Impacts were performed with a 25.4 mm steel impactor, with 1.5, 3 and 4 J energy impacts respectively. This was done to see if a higher energy impact led to greater change in dent profile and depth over time.

Before impact, the panel was scanned using laser topography so that a deviation map could be created; this baseline topography of the undamaged panel would be subtracted from all future scans, so that only the dents were left. Following impact the panel was setup for the laser topography scan. Scan duration was approximately three hours. Scans were performed five times over seven days.

Figure 4.65 shows the deviation map after impact, showing only the dent profiles. As expected, the dents increase in depth and diameter as the energy level increased. To detect small changes in the dent profiles, topography maps were subtracted from the baseline map seen in Figure 4.65. This provided an image that shows only the change in the dent profile over time, or 'relaxation' of the dent. Figure 4.66 shows the relaxation of panel B12 over a period of seven days. After day one, the change in dent profile is minimal and within the noise of the laser, however the trend is towards a greater change in dent depth and overall profile over time.

Figure 4.67 shows the dent depth profiles over the seven day period. The troughs of the profiles (i.e. dent depth) changes more than towards the edge of the dents. Figure 4.68 shows the maximum depth for the three impact locations over a period of seven days.
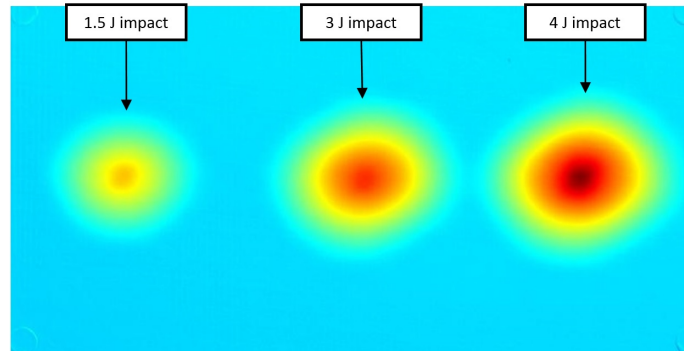
Figure 4.65: Laser topography baseline deviation map of panel B12 for relaxation study, showing 1.5, 3 and 4 J impacts. Dark red indicates greater depth, whereas blue indicates a flat surface.
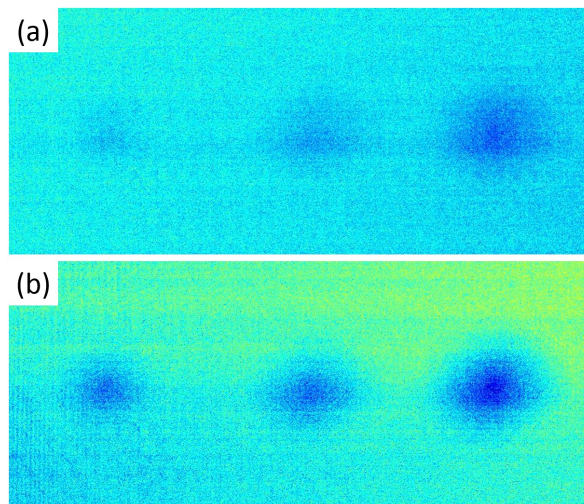
Figure 4.66: Dent relaxation for B12 over one week: (a) after one day; and (b) after seven days. Fuzzy images are a result of the small measurements within the limits of the laser's accuracy. Darker blue indicates greater change in depth.
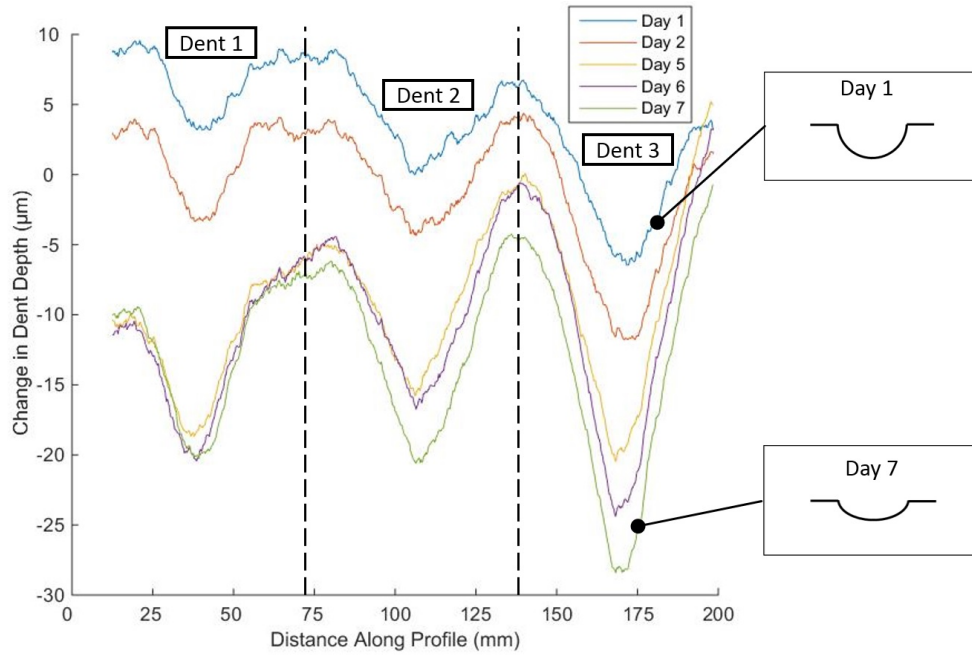
Figure 4.67: Long term dent relaxation profile B12 over time showing the dent depth and profile reducing over time. Plot created using average of scan
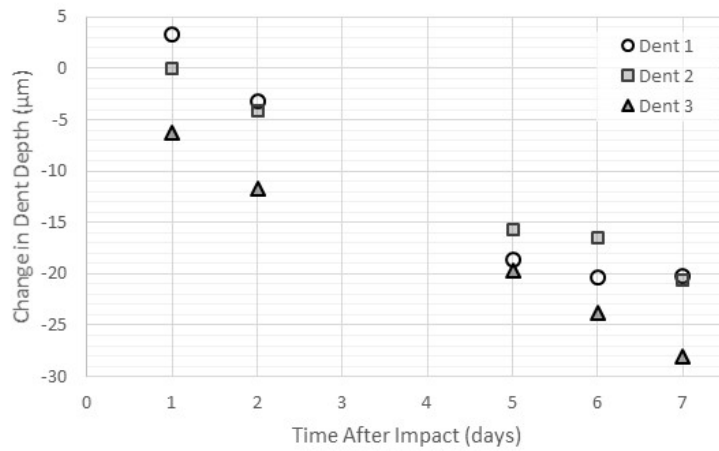
Figure 4.68: Change in dent depth over time for 1.5, 3 and 4 J impacts.

115

4.4.1 Discussion

Dent Relaxation and Damage Detection

Long term dent relaxation does occur over long periods of time. From 3 hours post impact until 7 days, panel relaxation of dents using three different energy levels was observed and relaxation appears to be greater for higher energy impacts. Relaxation was smaller than 30 µm over the week-long period, which is not significant between detecting or not detecting an dent in a panel (for comparison, the thickness of a single ply is roughly 130 µm). The relaxation did not appear to level off noticeably at the end of the week-long period; additional study would be required to determine if the dents reach an equilibrium depth. It is suspected that any significant relaxation occurs shortly following impact, however this method of study would not work for this purpose (a single point laser measurement setup would be required to measure short term relaxation, similar to *Minakuchi* [67]).

Cause of Dent Relaxation

The source of the relaxation is most likely the residual stress in the facesheet post impact; the laminate pulls the crushed core towards a state of zero residual stress, however this is resisted by the yielded core. Due to the small amount of relaxation, it is possible that the source could be changes in the matrix in the laminate, or it could be caused by a gradual change in temperature; these are unlikely causes for what was observed, but they are possibilities given the very small changes in dent depth.

Figure 4.67 shows that there is both a local and global relaxation occurring in the panels over the period observed. When observing the edges of the dent profiles, these change over time along with the center of the dent. One edge relaxes more than the other. This could be a source of error (e.g. very small temperature changes leading to global measurement changes) or could be a phenomenon. Locally, the center of the dent profile for all indentations has a greater change over time, which is the expected relaxation. The reason for the center of the dent changing more than the edges of the dent is shown in Figure 4.69, similar to a slack rope being pulled taut.

Limitations and Sources of Error

The trade off in this study is while a detailed profile of the dents changing over time was developed, a limitation was the time required to perform a scan. By sacrificing some accuracy, change in panel depth and profile over time could possibly be conducted to show changes taking place immediately following impact, which are likely more significant.

Sources of error include small temperature changes which may cause the specimen to expand changing the depth measurements, accumulated superposition error (i.e. a measurement error may be compounded by post-processing which includes translation, rotation and subtraction of the panel topographies), and possible shifting or settling of the specimen (the specimen was placed on a solid table, however minor vibrations could possibly cause slight movement of the specimen relative to the laser).
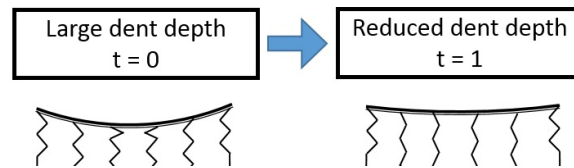
Figure 4.69: Example of dent relaxation over time. Residual stresses in the facesheet straighten out the yielded aluminum crushed core. Change in depth is greater at the center of the dent than towards the outer edges.

5 Conclusions

An exploratory approach was taken to investigate the characteristics of impact damaged aircraft sandwich panels. Destructive and non-destructive characterization of the non-standardized panels uncovered relationships regarding damage as a result of impactor size, possible concerns regarding damage resistance and tolerance of repaired sandwich panels, the effectiveness of using panel stiffness to map out and inspect damaged panels, and dent relaxation in composite panels.

Key conclusions were:

- Increasing impactor diameter led to greater dent and damage diameter for a hemispherical impactor. Failure mode changed from a mixed mode (i.e. fibre breakage, delamination and core crush) to core crush with no facesheet damage as impactor diameter increased for the same energy level of impact.
- A impacted repair patch may result in undetectable damage to the underlying facesheet. The repair adhesive should be selected in order to ensure it has sufficient toughness, and impact should be a consideration when designing and certifying repairs.
- The C-scan tap test was capable of detecting all impact damages that could be detected with ultrasound and radiography. The tap test was able to size damage areas. It is inconclusive if the C-scan tap test can distinguish different failure modes, or if it can detect damages for a very thick laminate.
- Dent relaxation did occur in the panels studied, but the amount of relaxation was negligible. It is suspected that most dent relaxation occurs immediately after the impact event.

A fixture was designed in order to accommodate the panels as they had varying geometry, and this modification to the drop tower allowed for consistent out-of-plane impact in lieu of the ASTM standard for coupon level testing [40].

For a target 3 J impact energy level, it was found that increasing impactor diameter led to greater dent and damage area that became more difficult to visually detect. Dent depth decreased for increasing impactor size. The failure mode for the smallest impactor was mixed with combined laminate damage (i.e. fibre failure, matrix cracking and delamination) and core crushing. Larger impactors had less significant laminate damage, but still caused a crushed core. The largest impactor did not have any laminate damage and had minimal core crushing. Ultrasound and the C-scan tap test could detect the damages in the panel; visual inspection on its own would not have likely uncovered damage from the largest impactors.

Characterization of the damage incurred by a target 5 J impact on a repaired panel found that while the visual indication of damage was less for impact in the center of the repair patch, the underlying damage was more significant than in the regular panel. Impact just outside of the repair patch led to greater damage than a similar unrepaired panel, however this was visually detectable unlike damage in the center of the patch. Brittle failure of the material used to join the repair patch to the panel caused the patch to spring back. Impact damage could potentially grow undetected underneath the patch leading to structural failure. Considerations when repairing sandwich panels should be the potential of impact, and therefore should be considered in certification of repairs for composite sandwich structure. This also shows that follow-up inspections for repairs is an important consideration for composites.

The C-scan tap test was effective in locating the damages caused by low-velocity impact, and comparable to ultrasound in its ability to detect damage. While the C-scan tap test could detect impact damages, this does not mean that this method would detect everything that ultrasound can detect. For example, water ingress in the core leading to corrosion or core fatigue may not cause a local stiffness change and therefore would not be detected using a tap test. By choosing a threshold contact time for components and a consistent test methodology, damages could be sized and compared to ultrasound. Increased crushed core appears to correlate well with contact time, and crushed core appears to affect stiffness more than laminate damage.

Long term dent relaxation was observed between 3 hours and 7 days after impact, and greater relaxation was observed for higher energy impacts. Dent relaxation was negligible within this time frame from a damage detection standpoint, less than 30 µm or roughly 23 % of the thickness of a single lamina of CFRP. Superposition of laser topography allowed for the relaxation to be observed over the entire panel, and showed that the center of the impact locations relaxed more than the edges of the dent. It is expected that dent relaxation would be greater shortly after impact.

5.1 Future Work

There is various research that would be of interest to pursue as a result of this paper for impact on repairs, the C-scan tap test and dent relaxation.

It may be of interest for future studies to evaluate if the fibre failure of the laminate can be distinguished using the profile curvature through the use of laser topography.

Additional impact testing on repaired sandwich panels and composites would reveal if repairs in general are more susceptible to BVID. Damage tolerance of damaged composite repairs would also be interesting to see if the static margin of safety or fatigue life is reduced.

Further exploration of the C-scan tap test or CATT would be of interest to investigate if a decrease in local panel stiffness can be correlated to a decreased static margin of safety for sandwich panels in bending and compression-after-impact. Testing with other damage types such as fatigued core, corroded core, or blown core may also be of interest. Exploring if the contact time variance seen for repeated taps is a source of error, or in fact an exploitable behaviour that could be used to detect damages would be of interest. Testing on other structural composites (e.g. aluminum facesheets, Nomex core, etc) would also be informative for comparison on the effectiveness of using local stiffness for damage detection. Automation of the process would be necessary for extensive study using the C-scan tap test.

Studies of short-term dent relaxation would be more relevant for future research, and would be of interest for various types of sandwich panels to see what combinations of materials are most susceptible to BVID. Sectioning panels in these studies could serve to see if the failure mode plays a large role in the amount of relaxation (it is suspected that certain failure modes, such as delamination of facesheets or disbond will lead to more significant relaxation).

References

[1] William D Callister and David G Rethwisch. *Materials science and engineering: an introduction*. Wiley New York, 2007.

[2] Michael F Ashby. *Materials selection in mechanical design*. Butterworth-Heinemann, 2004.

[3] Dewey H Hodges and G Alvin Pierce. *Introduction to Structural Dynamics and Aeroelasticity*. Cambridge university press, 2011.

[4] Hexcel. Sandwich panel fabrication technology, 2001.

[5] HexWeb. Honeycomb sandwich design technology, 2000.

[6] Frank A Leone Jr, Didem Ozevin, Valery Godinez, Bao Mosinyi, John G Bakuckas Jr, Jonathan Awerbuch, Alan Lau, and Tein-Min Tan. Acoustic emission analysis of full-scale honeycomb sandwich composite curved fuselage panels. In *The 15th International Symposium on: Smart Structures and Materials & Nondestructive Evaluation and Health Monitoring*, pages 69340E–69340E. International Society for Optics and Photonics, 2008.

[7] NSF-ATE (Advanced Technological Education). Applications, acoustic emission, NDT resource center. Internet. Retrieved 14 Oct 2015.

[8] FAA, AC. *AC 20-107B, Composite Aircraft Structure*. U.S. Department of Transportation, Federal Aviation Administration, 2009.

[9] FAA, AC. *AC22.571-1D, Damage Tolerance and Fatigue Evaluation of Structure*. U.S. Department of Transportation, Federal Aviation Administration, 2011.

[10] Hyonny Kim. Impact damage formation on composite aircraft structures. Technical report, Department of Structural Engineering, University of California San Diego, La Jolla, CA, 2010.

[11] AD Balk. Safety of ground handling. Technical report, National Aerospace Laboratory, 2007.

[12] BPY Tang, P Hungler, CP Sweetapple, and LGI Bennett. An quantitative evaluation of the Canadian Forces new radiology inspection systems for the detection of water ingress in CF188 flight control surfaces. Shanghai, China, 2008.

[13] Transportation Safety Board of Canada. *Loss of Rudder in Flight, Air Transat, Airbus A310-308 C-GPAT, Miami, Florida, 90 NM S, 06 March 2005.* Minister of Public Works and Government Services Canada, Gatineau, Quebec, 2007. Aviation Investigation Report A05F0047.

[14] Paolo Feraboli. Some recommendations for characterization of composite panels by means of drop tower impact testing. *Journal of aircraft*, 43(6):1710–1718, 2006.

[15] Shaw Ming Lee and Paul Zahuta. Instrumented impact and static indentation of composites. *Journal of Composite Materials*, 25(2):204–222, 1991.

[16] Paul A Lagace, James E Williamson, PH Wilson Tsang, Edward Wolf, and Stephen Thomas. A preliminary proposition for a test method to measure (impact) damage resistance. *Journal of Reinforced Plastics and Composites*, 12(5):584–601, 1993.

[17] Alan T Nettles and Michael J Dougles. A comparison of quasi-static indentation to low-velocity impact. 2000.

[18] Serge Abrate. *Impact on composite structures.* Cambridge university press, 2005.

[19] KS Raju. *The static indentation behavior of composite sandwich panels with thin quasi-isotropic skins.* PhD thesis, Ph. D. Dissertation, Department of Aerospace Engineering, Wichita State University, 2001.

[20] Peter Shyprykevich, J Tomblin, L Ilcewicz, AJ Vizzini, and TE Lacy. Guidelines for analysis, testing, and nondestructive inspection of impact-damaged composite sandwich structures. Technical report, DTIC Document, 2003.

[21] HP Kan, R Cordero, and RS Whitehead. Advanced certification methodology for composite structures. Technical report, DTIC Document, 1997.

[22] Robin Olsson. Engineering method for prediction of impact response and damage in sandwich panels. *Journal of Sandwich Structures and Materials*, 4(1):3–29, 2002.

[23] Costantino Menna, Alberto Zinno, Domenico Asprone, and Andrea Prota. Numerical assessment of the impact behavior of honeycomb sandwich structures. *Composite Structures*, 106:326–339, 2013.

122

[24] Ines Ivanez and Sonia Sanchez-Saez. Numerical modelling of the low-velocity impact response of composite sandwich beams with honeycomb core. *Composite Structures*, 106:716–723, 2013.

[25] Michele Meo, AJ Morris, R Vignjevic, and G Marengo. Numerical simulations of low-velocity impact on an aircraft sandwich panel. *Composite Structures*, 62(3):353–360, 2003.

[26] FAA, PS. *PS-ANM-25-20, High-Energy Wide-Area Blunt Impact for Composite Structures*. U.S. Department of Transportation, Federal Aviation Administration, 2015.

[27] Chun-Gon Kim and Eui-Jin Jun. Impact resistance of composite laminated sandwich plates. *Journal of Composite Materials*, 26(15):2247–2261, 1992.

[28] Michael L Bernard and Paul A Lagace. Impact resistance of composite sandwich plates. *Journal of Reinforced Plastics and Composites*, 8(5):432–445, 1989.

[29] Tode Palm. Impact resistance and residual compression strength of composite sandwich panels. *Composites*, 1991.

[30] CC Foo, GB Chai, and LK Seah. Quasi-static and low-velocity impact failure of aluminium honeycomb sandwich panels. *Proceedings of the Institution of Mechanical Engineers, Part L: Journal of Materials Design and Applications*, 220(2):53–66, 2006.

[31] Temoana Southward, DPW Horrigan, Gordon D Mallinson, Krishnan Jayaraman, et al. Failure of sandwich composite structure containing face-sheet/core disbonds-an experimental study. *Australian Journal of Mechanical Engineering*, 6(2):127, 2008.

[32] T Besant, GAO Davies, and D Hitchings. Finite element modelling of low velocity impact of composite sandwich panels. *Composites Part A: Applied science and manufacturing*, 32(9):1189–1196, 2001.

[33] WJ Cantwell and J Morton. The impact resistance of composite materials. *Composites*, 22(5):347–362, 1991.

[34] Kwang-Woo Jeon and Kwang-Bok Shin. An experimental investigation on low-velocity impact responses of sandwich panels with the changes of impact location and the wall partition angle of honeycomb core. *International Journal of Precision Engineering and Manufacturing*, 13(10):1789–1796, 2012.

[35] John S Tomblin, KS Raju, J Liew, and BL Smith. Impact damage characterization and damage tolerance of composite sandwich airframe structures. Technical report, DTIC Document, 2001.

[36] Laura S Kistler and Anthony M Waas. Experiment and analysis on the response of curved laminated composite panels subjected to low velocity impact. *International journal of impact engineering*, 21(9):711–736, 1998.

[37] Jean-Claude Flabel. *Practical Stress Analysis for Design Engineers*. Lake City Publishing Company, first edition, 1997.

[38] CMH-17-Vol-6. *Structural Sandwich Composites*. Wichita State University, 2013.

[39] CC Lawrence. A new methodology in the evaluation of non-flat plastic samples when using an instrumented falling weight test approach. *Polymer testing*, 18(6):463–479, 1999.

[40] ASTM D7766 / D7766M-11. Standard practice for damage resistance testing of sandwich constructions. ASTM International, West Conshohocken, PA, 2011, http://www.astm.org.

[41] ASTM D7136 / D7136M-15. Standard test method for measuring the damage resistance of a fiber-reinforced polymer matrix composite to a drop-weight impact event. ASTM International, West Conshohocken, PA, 2015, http://www.astm.org.

[42] Eric J Herup and Anthony N Palazotto. Low-velocity impact damage initiation in graphite/epoxy/nomex honeycomb-sandwich plates. *Composites Science and Technology*, 57(12):1581–1598, 1998.

[43] MIL-HDBK-17-3F. *Composites Materials Handbook, Polymer Matrix Composites: Materials Usage, Design, and Analysis*, volume 3. Department of Defense, 2002.

[44] MIL-HDBK-337. *Repair of Adhesive Bonded Aerospace Structures*. Department of Defense, Washington, DC, USA, 1982.

[45] David K Hsu. Nondestructive evaluation of sandwich structures. In AJM Ferreira, editor, *8th International Conference on Sandwich Structures*, 2008.

[46] David K Hsu, John J Peters, Dong Fei, Daniel J Barnard, and Vinay Dayal. Imaging of flaws in composite honeycomb aircraft structures using instrumented tap test. In *Nondestructive Evaluation Techniques for Aging Infrastructures & Manufacturing*, pages 236–245. International Society for Optics and Photonics, 1999.

[47] David K Hsu, JJ Peters, and Daniel J Barnard. Development of fieldable systems for inspecting aircraft composite structures. In *Key Engineering Materials*, volume 270, pages 1845–1851. Trans Tech Publ, 2004.

[48] T.O. 33B-1-1/NAVAIR 01-1A-16-1/TM 1-1500-335-23. *Nondestructive Inspection Methods, Basic Theory*. United States Air Force, 2014.

[49] NSF-ATE (Advanced Technological Education). Data presentation, ultrasound, NDT Resource Center. Retrieved 16 Apr 2016.

[50] Cory Foreman. Nondestructive detection and characterization of damages in honeycomb composite structures. Master's thesis, Iowa State University, 2008.

[51] Advanced Structural Imaging. Makers of the computer-aided tap tester. Internet, http://www.asi-nde.com/index.html. Retrieved 14 Oct 2015.

[52] Vernal H Kenner, George H Staab, and Hung-Sying Jing. Quantification of the tapping technique for the detection of edge defects in laminated plates. *American Society for Testing and Materials STP*, 876:465–480, 1985.

[53] DK Hsu, DJ Barnard, JJ Peters, and V Dayal. Development of nondestructive inspection methods for composite repair. In *AIP Conference Proceedings*, number B, pages 1019–1025. IOP Institute of Physics Publishing Ltd, 2003.

[54] Maldague Xavier. *Nondestructive Evaluation of Materials by Infrared Thermography*. Springer-Verlag, London New York, 1993.

[55] RD Adams and PDRD Cawley. A review of defect types and nondestructive testing techniques for composites and bonded joints. *NDT international*, 21(4):208–222, 1988.

[56] David K Hsu. Nondestructive evaluation of sandwich structures: a review of some inspection techniques. *Journal of Sandwich Structures and Materials*, 11(4):275–291, 2009.

[57] JF Clarady and M Summers. Electronic holography and shearography NDE for inspection of modern materials and structures. In *Review of Progress in Quantitative Nondestructive Evaluation*, pages 381–386. Springer, 1993.

[58] Christian Garnier, Marie-Laetitia Pastor, Florent Eyma, and Bernard Lorrain. The detection of aeronautical defects in situ on composite structures using non destructive testing. *Composite structures*, 93(5):1328–1336, 2011.

[59] Olympus. Nondestructive bond testing for aircraft composites, http://olympus-ims.com/en/applications/non-destructive-bond-testing-aircraft-composites.html. Retrieved 16 Apr 2016.

[60] FJ Yang and WJ Cantwell. Impact damage initiation in composite materials. *Composites Science and Technology*, 70(2):336–342, 2010.

[61] David M McGowan and Damodar R Ambur. Damage characteristics and residual strength of composite sandwich panels impacted with and without compression loading. In *Proc 39th Structural Dynamics and Materials Conference*, pages 20–23, 1998.

[62] Tom Mitrevski, IH Marshall, and Rodney Thomson. The influence of impactor shape on the damage to composite laminates. *Composite Structures*, 76(1):116–122, 2006.

[63] HP Kan. *Enhanced Reliability Prediction Methodology for Impact Damaged Composite Structures*. U.S. Department of Transportation, Federal Aviation Administration, 1998.

[64] John S Tomblin, KS Raju, J Liew, and BL Smith. Impact damage characterization and damage tolerance of composite sandwich airframe structures phase II. Technical report, DTIC Document, 2002.

[65] MD Rhodes. Impact fracture of composite sandwich structures. In *ASME/AIAA/SAE, 16th Struct., Struct. Dyn. and Materials Conf.*, 1975.

[66] JH Park, SK Ha, KW Kang, CW Kim, and HS Kim. Impact damage resistance of sandwich structure subjected to low velocity impact. *Journal of materials processing technology*, 201(1):425–430, 2008.

[67] S Minakuchi, T Uezono, J Siivola, and N Takeda. Facesheet dent formation and relaxation on indented foam-core sandwich beams.

[68] Roman Ruzek, Radek Lohonka, and Josef Jironc. Ultrasonic C-scan and shearography NDI techniques evaluation of impact defects identification. *NDT & E International*, 39(2):132–142, 2006.

[69] ASTM D6264 / D6264M-12. Damage resistance fiber reinforced polymer matrix composite quasi static indentation force. ASTM International, West Conshohocken, PA, 2012, http://www.astm.org.

[70] Lawrence Cook. *Visual Inspection Reliability for Composite Aircraft Structures*. PhD thesis, Cranfield University, October 2009.

[71] ASTM E2580-12. Standard practice for ultrasonic testing of flat panel composites and sandwich core materials used in aerospace applications. ASTM International, West Conshohocken, PA, 2012, http://www.astm.org.

[72] Mike Brothers. Email on inspection parameters of ultrasonic inspection and radiography performed on panels, July 2015.

Appendices

A Material Data Sheets

The following provides the material data sheets that are available for the panels studied.

HexTow® AS4 carbon fiber is a continuous, high strength, high strain, PAN based fiber available in 3,000 (3K), 6,000 (6K) and 12,000 (12K) filament count tows. This fiber has been surface treated and can be sized to improve its interlaminar shear properties, handling characteristics, and structural properties, and is suggested for use in weaving, prepregging, filament winding, braiding, and pultrusion.

AS4-GP 3k (1%), AS4-GP 12k (0.9%), and AS4 12k carbon fibers have been qualified to NMS 818 Carbon Fiber Specification (NCAMP). This allows customers to call out an industry standard, aerospace grade carbon fiber without the need to write and maintain their own specification.

Typical Fiber Properties	U.S. Units	SI Units
Tensile Strength		
3K	670 ksi	4,620 MPa
6K	640 ksi	4,410 MPa
12K	640 ksi	4,410 MPa
Tensile Modulus (Chord 6000-1000)	33.5 Msi	231 GPa
Ultimate Elongation at Failure		
3K	1.8%	1.8%
6K	1.7%	1.7%
12K	1.7%	1.7%
Density	0.0647 lb/in^3	1.79 g/cm^3
Weight/Length		
3K	11.8×10^{-6} lb/in	0.210 g/m
6K	23.9×10^{-6} lb/in	0.427 g/m
12K	48.0×10^{-6} lb/in	0.858 g/m
Approximate Yield		
3K	7,086 ft/lb	4.76 m/g
6K	3,485 ft/lb	2.34 m/g
12K	1,734 ft/lb	1.17 m/g
Tow Cross-Sectional Area		
3K	1.82×10^{-4} in^2	0.12 mm^2
6K	3.70×10^{-4} in^2	0.24 mm^2
12K	7.43×10^{-4} in^2	0.48 mm^2
Filament Diameter	0.280 mil	7.1 microns
Carbon Content	94.0%	94.0%
Twist	Never Twisted	Never Twisted

Typical HexPly 8552 Composite Properties (at Room Temperature)	U.S. Units	SI Units	Test Method
0º Tensile Strength	320 ksi	2,205 MPa	ASTM D3039
0º Tensile Modulus	20.5 Msi	141 GPa	
0º Tensile Strain	1.55%	1.55%	
0º Flexural Strength	274 ksi	1,889 MPa	ASTM D790
0º Flexural Modulus	18.4 Msi	127 GPa	
0º Short Beam Shear Strength	18.5 ksi	128 MPa	ASTM D2344
0º Compressive Strength	222 ksi	1,530 MPa	ASTM Mod. D695
0º Compressive Modulus	18.6 Msi	128 GPa	
0˚ Open Hole Tensile Strength	64 ksi	438 MPa	ASTM D5766
90º Tensile Strength	11.7 ksi	81 MPa	ASTM D3039
Fiber Volume	60%	60%	

HEXCEL®

Yarn/Tow Characteristics	U.S. Units	SI Units
Specific Heat	0.28 Btu/lb-°F	0.27 cal/g-°C
Electrical Resistivity	5.6×10^{-5} ohm-ft	1.7×10^{-3} ohm-cm
Coefficient of Thermal Expansion	-0.35 ppm/°F	-0.63 ppm/°C
Thermal Conductivity	3.95 Btu/hr-ft-°F	6.83 W/m-°K

Carbon Fiber Certification

This carbon fiber is manufactured to Hexcel aerospace grade specification HS-CP-5000. A copy of this specification is available upon request. A Certification of Analysis will be provided with each shipment.

Available Sizing

Sizing compatible with various resin systems, based on application are available to improve handling characteristics and structural properties. Please see additional information on available Sizes on our website or contact our technical team for additional information.

Packaging

Standard packaging of HexTow® AS4 is as follows:

Filament Count	Nominal Weight		Nominal Length	
	(lb)	(kg)	(ft)	(m)
3K	4.0	1.8	28,340	8,640
6K	4.0	1.8	13,940	4,250
12K	8.0	3.6	13,870	4,230

Other package sizes may be available on request. The fiber is wound on a 3-inch ID by 11-inch long cardboard tube and overwrapped with plastic film.

Safety Information

Obtain, read, and understand the Material Safety Data Sheet (MSDS) before use of this product.

HEXCEL®

Important

Hexcel Corporation believes, in good faith, that the technical data and other information provided herein is materially accurate as of the date this document is prepared. Hexcel reserves the right to modify such information at any time. The performance values in this data sheet are considered representative but do not and should not constitute specification minima. The only obligations of Hexcel, including warranties, if any, will be set forth in a contract signed by Hexcel or in Hexcel's then current standard Terms and Conditions of Sale as set forth on the back of Hexcel's Order Acknowledgement.

For more information

Hexcel is a leading worldwide supplier of composite materials to aerospace and other demanding industries. Our comprehensive product range includes:

- Carbon Fiber
- RTM Materials
- Honeycomb Cores
- Carbon, Glass, Aramid and Hybrid Prepregs

- Structural Film Adhesives
- Honeycomb Sandwich Panels
- Special Process Honeycombs
- Reinforced Fabrics

For US quotes, orders and product information call toll-free 1-866-556-2662 and 1-800-987-0658.
For other worldwide sales office telephone numbers and a full address list, please click here:
http://www.hexcel.com/contact/salesoffice

February 2014

Description

3501-6 is an amine cured epoxy resin system supplied with unidirectional or woven carbon or glass fibers. Typical reinforcement is continuous AS4 carbon filaments. 3501-6 was developed to operate in a temperature environment of up to 350°F (177°C). AS4/3501-6 is recommended for general purpose structural applications.

Features

■ Service Temperature up to 350°F (177°C)

■ Damage-Resistant System

■ 350°F (177°C) Cure

Neat Resin Properties

Density	1.265 gm/cc
T_g dry 6 hr 350°F (177°C) cure	410°F (210°C)
T_g wet 6 hr 350°F (177°C) cure	304°F (151°C)
Tensile strength	6.6 ksi
Tensile modulus	0.615 msi
Tensile elongation	1.10%
Shear strength	7.0 ksi
Shear elongation to failure	1.95%
Flexural modulus	484 ksi
Poisson's ratio	36.50%
Strain energy release rate, G_{1C}	0.733 in-lb/in^2
Gel time @ 350°F (177°C)	4–10 minutes
Minimum viscosity	4.0 Poise
Coefficient of thermal expansion (CTE)	
RT–163°F (RT–73°C)	21.1 x 10^6/°F
160–250°F (71–121°C)	24.4 x 10^6/°F
250–350°F (121–177°C)	33.3 x 10^6/°F

HEXCEL Composites

3501-6 Epoxy Matrix *Product Data*

Physical Properties

		AS4	A185CSW	A193P	A280-5H	A370-8H
Prepreg	% Resin content	32–45	32–45	32–45	32–45	32–45
	Areal weight GSM	150	185	193	280	370
	% Volatiles	1.5 max	1.5 max	1.5 max	1.5 max	1.5 max
	% Flow	12–32	12–32	12–32	12–32	12–32
	Gel time @ 350°F (177°C)	6–12	6–12	6–12	6–12	6–12
Laminate	Cured thickness per ply (in)	5.2 mils	7.5 mils	7.7 mils	10.0 mils	14.0 mils
	Fiber volume	62%	58%	58%	58%	58%

Mechanical Properties

Property	Temp °F (°C)	Condition	AS4	A185CSW	A193P	A280-5H	A370-8H
0° Tensile strength, ksi	RT	Dry	310.0	120.0	110.0	120.0	120.0
0° Tensile modulus, msi	RT	Dry	20.5	10.0	10.0	10.0	10.0
0° Compression strength, ksi	RT	Dry	250.0	120.0	125.0	130.0	125.0
0° Flexural strength, ksi	RT	Dry	260.0	10.0	9.0	9.0	9.0
0° Flexural strength, ksi	350 (177)	Dry	185.0	–	–	150.0	130.0
0° Flexural modulus, msi	RT	Dry	18.5	–	–	–	–
0° Flexural modulus, msi	350 (177)	Dry	18.0	–	–	10.0	9.0
Short beam shear, psi	RT	Dry	18,500	–	–	–	–
Short beam shear, psi	350 (177)	Dry	9,500	12,000	12,000	12,000	12,000

Cure Cycle
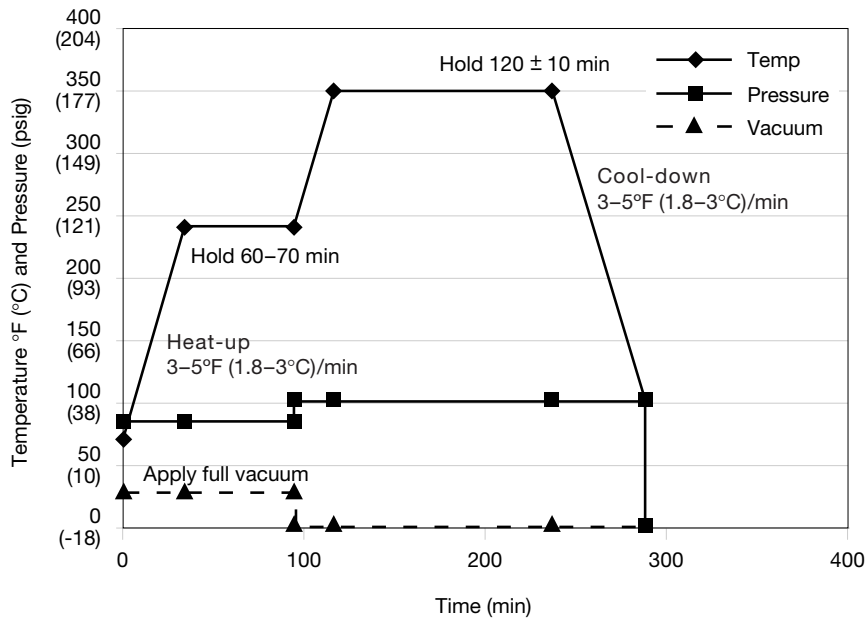
Cure Procedure

Autoclave

1. Apply full vacuum and 85 psig pressure.

2. Heat at 3–5°F (1.8–3°C)/minute to 240°F (116°C).

3. Hold at 240°F (116°C) for 60–70 minutes.

4. Raise pressure to 100 psig; vent vacuum.

5. Raise temperature to 350°F (177°C) at 3–5°F (1.8–3°C)/minute.

6. Hold at 350°F (177°C) for 120 ± 10 minutes.

7. Cool at 2–5°F (1.2–3°C) to 100°F (38°C) and vent pressure.

Note: Straight-up cure cycle may be used.

Handling and Safety Precautions

Hexcel recommends that customers observe established precautions for handling resins and fine fibrous materials. Operators working with this product should wear clean, impervious gloves to reduce the possibility of skin contact and to prevent contamination of the material.

Material Safety Data Sheets (MSDS) have been prepared for all Hexcel products and are available to company safety officers on request from your nearest Hexcel Sales Office.

Storage

3501-6 prepreg should be sealed in a polyethylene bag and refrigerated, preferably below 32°F (0°C). Following removal from refrigerated source, allow the prepreg to reach room temperature before opening the polyethylene bag to prevent moisture condensation.

Shelf Life

12 months at 0°F (–18°C)

4 months at 40°F (4°C)

10 days at 70°F (21°C)

Shipping

Prepreg is generally shipped in a sealed polyethylene bag in refrigerated transportation or in containers with dry ice.

Disposal of Scrap

Disposal of this material should be in a landfill in accordance with state and federal regulations.

Important

Hexcel Corporation makes no warranty, whether expressed or implied, including warranties of merchantability or of fitness for a particular purpose. Under no circumstances shall Hexcel Corporation be liable for incidental, consequential, or other damages arising out of a claim from alleged negligence, breach of warranty, strict liability or any other theory, through the use or handling of this product or the inability to use the product. The sole liability of Hexcel Corporation for any claims arising out of the manufacture, use, or sale of its products shall be for the replacement of the quantity of this product which has proven to not substantially comply with the data presented in this bulletin. Users should make their own assessment of the suitability of any product for the purposes required. The above supercedes any provision in your company's forms, letters, or other documents.

For technical assistance, applications and procedures, or further information, please contact:

Administrative Office and Customer Service Center
5794 West Las Positas Blvd.
P.O. Box 8181
Pleasanton, CA 94588-8781
Tel (925) 847-9500
Fax (925) 734-9676

Hexcel Composites
Duxford, Cambridge CB2 4QD
United Kingdom
Tel 44 (0) 1223 833141
Fax 44 (0) 1223 838808

Sales Offices
2350 Airport Fwy., Suite 550
Bedford, TX 76022-6027
Tel (817) 315-3939
Fax (817) 571-8629

Sales Offices (continued)
101 East Ridge Drive, Suite 102
Danbury, CT 06810-4140
Tel (203) 798-8311
Fax (203) 798-8161

11410 Northeast 122nd Way, Suite 320
Kirkland, WA 98034-6927
Tel (425) 821-7411
Fax (425) 823-6437

Printed on recycled paper.

(8/98)

CYTEC

FM® 300 Epoxy Film Adhesive

DESCRIPTION

FM® 300 is a modified epoxy film adhesive available with three different moisture-resistant polyester carriers. It is designed for bonding metal-to-metal and sandwich composite structures. To achieve ultimate environmental resistance in bonding aluminum details, use pre-cured BR® 127 primer with FM 300 film adhesive.

Extensively used as a surface finished ply on composites material outside layers, FM 300 film adhesive has unique properties which drastically reduce, and in some cases virtually eliminate, time-consuming sanding and filling operations.

FM 300 film adhesive has high elongation and toughness with high ultimate shear strength. This makes it particularly suitable for redistributing the high shear stress concentrations of graphite epoxy- to-metal bonds, and allows it to accommodate the low interlaminar shear strength of the composite. It is particularly good in fatigue resistance in these joints. In properly designed and processed joints, the tight-knit tricot carrier provides a degree of electrical isolation between metal and graphite composites to reduce galvanic corrosion.

FEATURES & BENEFITS

- Superior metal-to-metal peel strength, composite-to-composite bonding and composite-to-metal joints
- Extensively used as surfacing ply for composite materials
- Service temperature from -67°F to 300°F (-55°C to 150°C)
- Excellent moisture and corrosion resistance in high humidity environments with no significant reduction in mechanical properties
- Allows x-ray inspection of assemblies due to natural opacity of adhesive formulations
- Available in a wide range of film thicknesses tailored to specific applications
- Industry wide acceptance

SUGGESTED APPLICATIONS

- Metal-to-metal bonding
- Composite-to-composite bonding
- Composite-to-metal bonding
- Composite surfacing

www.cytec.com

CHARACTERISTICS

Table 1 | Product Description for FM 300 Adhesive Films

Product Number	Weight, psf (gsm) [1]	Nominal Thickness, inches (mm)	Color	Carrier	Characteristics
FM 300 film adhesive	0.08 (390) 0.10 (490)	0.013 (0.32) 0.015 (0.38)	Blue Blue	Tight knit	Enhanced bondline thickness control. Good blend of structural and handling properties
FM 300K film adhesive	0.05 (244) 0.08 (390)	0.008 (0.20) 0.013 (0.32)	Green Green	Wide open knit	Highest overall performance
FM 300M film adhesive	0.03 (150) 0.08 (390)	0.005 (0.13) 0.013 (032)	Green Green	Random mat	Provides the best bondline and flow control. Reduces tendency to trap air during lay-up.
FM 300U film adhesive	0.03 (150) 0.055 (268)	0.005 (0.13) 0.008 (0.20)	Green Green	Unsupported film	Can be reticulated

[1] Weight tolerance equals nominal weight ± 0.005 psf (± 25 gsm)

Table 2 | Handling Properties of FM 300 Adhesive Films

Properties	Description
Volatiles	1.0% maximum
Outgassing properties (after complete cure)	0.92% TWL and 0.07% CVCM (NASA reference publication 1124, Rev. 8/87)
Recommended storage	Supported grades: store at or below 0°F (-18°C) Unsupported grades: store at 40°F (4.5°C)
Shelf life	Supported Grades: 12 months from date of shipment Unsupported Grades: 4 months from date of shipment
Shop life	10 days at 90°F (32°C) 30 days at 70°F (21°C)

Table 3 | Product Description: BR® 127 corrosion inhibiting primer

Properties	Description
Color	Yellow
Solids	10% ± 1% sprayable
Density	7.3 lbs/gal (875 g/liter)
Shop life	5 days at 90°F (32°C)
Shelf life	12 months from date of shipment at recommended storage
Recommended	Store at or below 0°F (-18°C)

PROPERTIES

Table 4 | Mechanical Properties[1]

Sample Description[2] Product Number	FM 300 0.08 psf (390 gsm)	FM 300K 0.05 psf (244 gsm)	FM 300K 0.08 psf (390 gsm)	FM 300M 0.03 psf (150 gsm)	FM300M 0.08 psf (390 gsm)
Tensile shear, psi (MPa)					
-67°F (-55°C)	5080 (35.0)	–	5460 (37.7)	–	4930 (34.0)
75°F (24°C)	5145 (35.5)	5340 (36.8)	5850 (40.3)	4325 (29.8)	5275 (36.4)
250°F (120°C)	3995 (27.6)	3575 (24.7)	4200 (28.9)	3360 (23.2)	4040 (27.9)
300°F (150°C)	2910 (20.0)	2965 (20.4)	3155 (21.8)	2310 (15.9)	2955 (20.4)
Floating roller peel, in-lb/in (kN/m)					
-67°F (-55°C)	28 (4.9)	–	28 (4.9)	–	29 (5.1)
75°F (24°C)	29 (5.1)	23 (40)	28 (4.9)	26 (4.6)	29 (5.1)
250°F (120°C)	–	–	–	–	–
300°F (150°C)	25 (4.4)	–	26 (4.6)	27 (4.7)	26 (4.6)
Honeycomb sandwich peel, in-lb/3 in (Nm/m)					
-67°F (-55°C)	–	25 (37)	40 (58)	–	–
75°F (24°C)	–	22 (32)	45 (66)	11 (16)	–
250°F (120°C)	–	–	–	–	–
300°F (150°C)	–	22 (32)	28 (41)	–	–
Flatwise tensile, psi (MPa)					
-67°F (-55°C)	1350 (9.3)	–	1075 (7.4)	–	1600 (11.0)
75°F (24°C)	1095 (7.6)	–	1030 (7.1)	435 (3.0)	1390 (9.6)
250°F (120°C)	–	–	–	–	–
300°F (150°C)	345 (2.4)	340 (2.3)	470 (3.2)	125 (0.86)	513 (3.5)

[1]FM 300, FM 300K and FM 300M film adhesives with BR 127 primer: Typical average results.
[2] Metal: Tensile shear 0.063 in. (1.63 mm) 2024-T3 clad, honeycomb skins 0.020 in. (0.51 mm) 2024-T3 clad, honeycomb 3/16 in. (4.76 mm)
0.002 (0.65 mm) NP5052, floating roller peel 0.025/0.063 2024-T3 clad

PAA-CORE™ 5056
Aluminum Honeycomb

Description

PAA-CORE 5056 aluminum honeycomb is the industry's highest-performing core material. Phosphoric acid anodized and coated with a proprietary primer, it outperforms all other core materials.

Decades of operational experience have shown that bond durability between core and face sheets is critical to long part life, and for this, PAA-CORE has no equal. Independent analysis confirms the environmental performance durability of PAA-CORE, assuring a lower total life cost than with other core materials. PAA-CORE also has unsurpassed corrosion resistance, experiencing only minimal weight loss after 31 days in an acidified salt spray chamber, which simulates the harshest environmental conditions. PAA-CORE retained virtually all of its physical properties during this test.

PAA-CORE outperforms non-metallic core materials, due to significantly higher strength-to-weight ratio and hot/wet strength. PAA-CORE offers designers higher performance with lower weight at less cost than non-metallic cores.

There is simply no equivalent to Alcore's PAA-CORE.
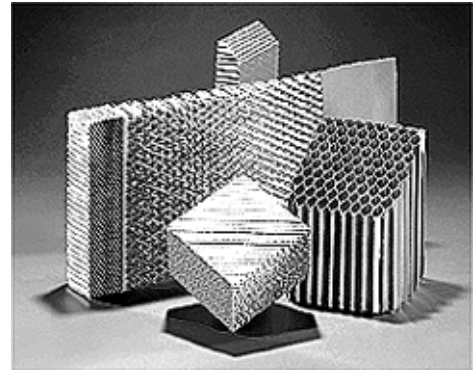
Applications

- Aircraft control surfaces
- Longer service aircraft flooring
- Aircraft landing gear doors
- Extended service aircraft engine nacelles
- Marine and naval panels
- Advanced energy absorbers
- High performance composite structures
- Replacement for non-metallic core materials

Features

- Unsurpassed corrosion resistance and bond durability
- Excellent strength-to-weight ratio
- Elevated temperature performance to 350° F/177° C
- Fire and fungus resistant
- Eliminates need for priming or pour-coat
- Easily machined and formed
- Resistant to hostile environments
- Exceeds MIL-C-7438 and many other aerospace specifications

Availability

- Unexpanded blocks
- Unexpanded slices
- Expanded sheets
- Pieces cut to size

PAA-CORE 5056 aluminum honeycomb is available with cell perforations to facilitate venting. Custom dimensions, cell sizes, tolerances and mechanical properties are also available.

How to Order

When ordering, please specify PAA-CORE 5056 using the following format:

Example: PAA - 5056 - 3.1 - 3/16 - N - E, where

Product	Alloy	Density	Cell Size	Perforated or Non-Perforated	Expanded or Unexpanded
PAA	5056	3.1	3/16	P or N	E or U

Available Dimensions

	Standard		Maximum		Tolerance	
	inches	mm	inches	mm	inches	mm
Ribbon (L)	48	1219	100	2540	+2.0 / -0.0	+50.8 / -0.0
Transverse (W)	96	2438	144	3658	+4.0 / -0.0	+101.6 / -0.0
			35	889		
Thickness (T)	up to 4 inches (102mm) T				±0.005	±0.127
	over 4 inches (102mm) T				±0.062	±1.575
Density	see mechanical characteristics chart					±10%
Cell Size	see mechanical characteristics chart					±10%

Alcore
Lakeside Business Park
1502 Quarry Drive
Edgewood, MD 21040 USA
Tel: +1 (410) 676-7100
Fax: +1 (410) 676-7200
Email: sales@alcore.com
www.alcore.com
www.mcgillcorp.com

Alcore Brigantine
Route de l'Aviation
64600 Anglet France
Tel: +33 (0)5 59 41 25 25
Fax: +33 (0)5 59 41 25 00
Email: sales@alcorebrigantine.fr
www.mcgillcorp.com/alcore_brigantine

Mechanical Characteristics (Typical Values - US units)									
	Stabilized Compressive Strength		Crush Strength	Shear Strength				Shear Modulus	
lbs/ft^3 - inches - inches	psi		psi	psi				ksi	
				L		W		L	W
	75° F	350° F	75° F	75° F	350° F	75° F	350° F	75° F	
3.1 - 1/8 - .0007	355	230	180	255	170	160	110	32	16
4.5 - 1/8 - .0010	700	480	320	450	274	260	180	51	25
6.1 - 1/8 - .0015	1210	780	550	700	425	410	245	77	37
8.1 - 1/8 - .0020	1920	1350	850	960	590	575	340	112	50
10.0 - 1/8 - .0025	2200	1625	1200	1190	830	675	455	140	60
12.0 - 1/8 - .0030	3250	1950	1550	1725*	1430*	1025*	465*	160	75
2.6 - 5/32 - .0007	270	160	130	205	130	120	90	24	12
3.8 - 5/32 - .0010	510	350	230	340	230	200	175	41	20
5.3 - 5/32 - .0015	875	625	435	560	370	335	230	64	31
6.9 - 5/32 - .0020	1350	1040	660	775	525	440	300	91	42
2.0 - 3/16 - .0007	205	115	80	145	100	87	70	17	9
3.1 - 3/16 - .0010	420	230	180	270	170	155	110	32	16
4.4 - 3/16 - .0015	675	475	310	435	260	250	170	50	24
5.7 - 3/16 - .0020	1010	730	480	570	410	335	225	70	34
6.9 - 3/16 - .0025	1250	1025	660	765	525	450	300	91	42
8.1 - 3/16 - .0030	1625	1350	850	925	590	550	340	112	50
1.6 - 1/4 - .0007	115	80	60	92	70	62	40	13	6
2.3 - 1/4 - .0010	270	150	120	185	110	105	75	21	11
3.4 - 1/4 - .0015	490	300	190	300	190	180	125	35	18
4.3 - 1/4 - .0020	630	460	300	410	255	235	160	48	24
5.2 - 1/4 - .0025	830	625	380	500	360	310	195	62	30
6.0 - 1/4 - .0030	1000	775	525	640	415	375	240	75	36
7.9 - 1/4 - .0040	1580	1300	820	900	565	540	330	108	49
1.0 - 3/8 - .0007	62	40	35	56	40	37	35	7	3
1.6 - 3/8 - .0010	115	85	60	93	70	63	40	13	6
2.3 - 3/8 - .0015	230	150	120	175	110	100	75	21	11
3.0 - 3/8 - .0020	350	220	160	250	165	150	100	30	15
3.7 - 3/8 - .0025	450	325	220	325	225	190	130	40	20
4.2 - 3/8 - .0030	550	410	290	395	260	225	155	47	23
5.4 - 3/8 - .0040	850	650	450	565	390	325	200	66	32
6.5 - 3/8 - .0050	1135	950	600	710	460	420	300	83	40
2.6 - 1/2 - .0025	230	160	130	190	130	100	90	24	12
3.0 - 1/2 - .0030	315	220	160	240	165	125	100	30	15
6.0 - 1/2 - .0040	1000	770	525	640	415	375	240	75	36
3.1 - 1/8 - .0007	355	230	180	255	170	160	110	32	16
4.5 - 1/8 - .0010	700	480	320	450	274	260	180	51	25
6.1 - 1/8 - .0015	1210	780	550	700	425	410	245	77	37
8.1 - 1/8 - .0020	1920	1350	850	960	590	575	340	112	50
10.0 - 1/8 - .0025	2200	1625	1200	1190	830	675	455	140	60
12.0 - 1/8 - .0030	3250	1950	1550	1725*	1430*	1025*	465*	160	75

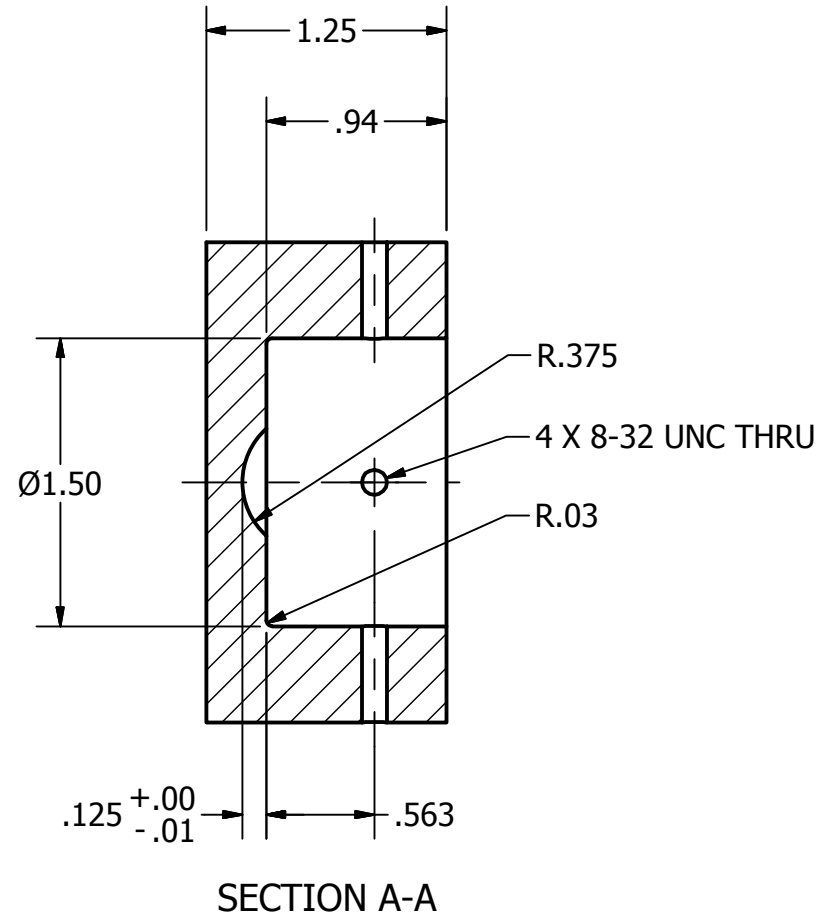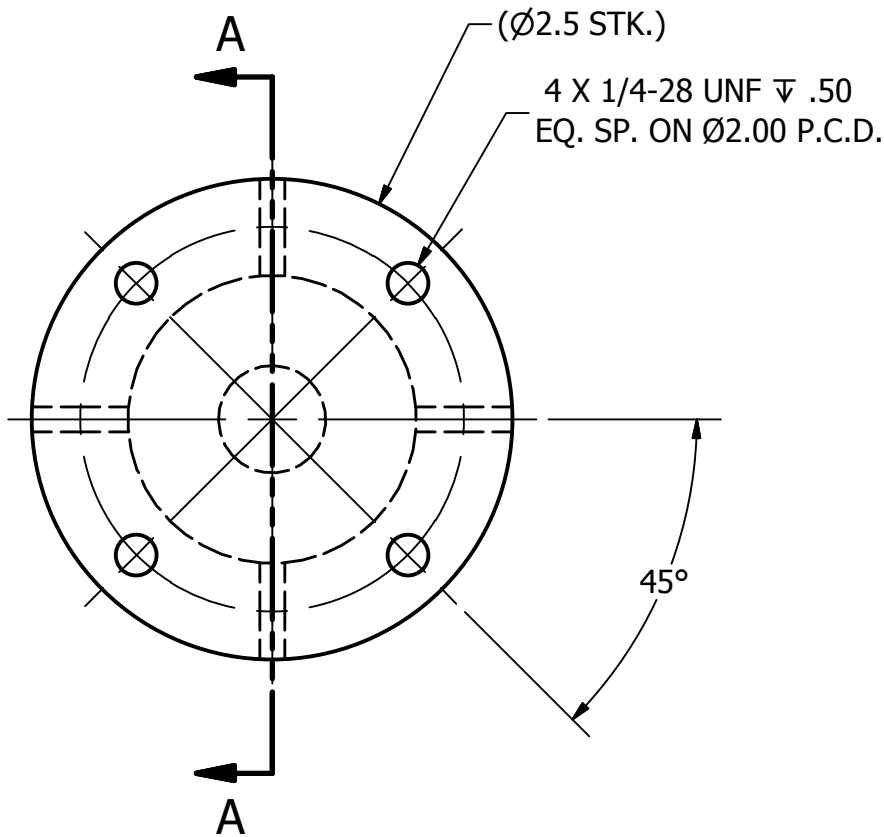For minimum values, please see MIL-C-7438.   * Beam Shear

ALCORE

B Fixture Drawings

The following provides the schematics for the designed fixture.

The guidance for the design was from myself, however the actual drawings and construction of the fixture was a combined effort of John Rogers, John MacMillan, and other staff at National Research Council of Canada, Aerospace Portfolio in Ottawa.

A

(Ø2.5 STK.)

4 X 1/4-28 UNF ⩒ .50
EQ. SP. ON Ø2.00 P.C.D.

Ø1.50

45°

A

1.25

.94

R.375

4 X 8-32 UNC THRU

R.03

.125 +.00 -.01

.563

SECTION A-A

ISSUED FOR REFERENCE

TITLE:
DROP TOWER SCREW JACK
INTERFACE

REQUIREMENTS - UNLESS OTHERWISE SPECIFIED				
GENERAL	LINEAR DIMENSION LIMITS:DECIMAL			

DIMENSIONS ARE IN INCHES
MACHINE FINISH: 125 μ IN. RMS
INTERNAL RADII .015
BREAK SHARP CORNERS .005 TO .015
HOLES: NOMINAL, +1/64
CONCENTRICITY: .010 TIR
ANGLES: ± 1/2°

	0-6"	6-12"	12-∞"
.X= ± .02	.X= ± .04	.X= ± .08
.XX= ± .01	.XX= ± .02	.XX= ± .04
.XXX= ± .005	.XXX= ± .01	.XXX= ± .02

LINEAR DIMENSION LIMITS:FRACTIONAL

0-6"	6-12"	12-∞"
± 1/32	± 1/16	± 1/8

PROJECT CODE:
A1-005561

SOFTWARE:
INVENTOR 2015

DRAWN BY:
J.MACMILLAN

DATE DRAWN:M/D/Y
05/27/2015

APPROVED BY:
J. ROGERS

DATE APPROVED:
06/03/2015

NEXT ASSEMBLY:

MATERIAL SPECIFICATION:
ALUMINUM

SCALE:
1:1

QUANTITY:
1

DRAWING NUMBER:
30149-1

REV:

SIZE:
A

(∅7.0 STK.)

.50

45°

4 x ∅.280 THRU
⌴ ∅.415 ▽ .265
EQ. SP. ON ∅2.00 P.C.D.

4 X ∅.280 THRU
⌴ ∅.415 ▽ .265
EQ. SP. ON ∅6.00 P.C.D.

ISSUED FOR REFERENCE

National Research
Council Canada

INSTITUTE FOR AEROSPACE RESEARCH
STRUCTURES, MATERIALS & PERFORMANCE LABORATORY

DROP TOWER SCREW JACK
PLATEN

REQUIREMENTS - UNLESS OTHERWISE SPECIFIED				PROJECT CODE:	DRAWN BY:	APPROVED BY:	MATERIAL SPECIFICATION:		
GENERAL	LINEAR DIMENSION LIMITS:DECIMAL			A1-005561	J.MACMILLAN	J. ROGERS	ALUMINUM		
DIMENSIONS ARE IN INCHES	0-6"	6-12"	12-∞"		DATE DRAWN:M/D/Y	DATE APPROVED:	SCALE:		QUANTITY:
MACHINE FINISH: 125 μ IN. RMS	.X= ± .02	.X= ± .04	.X= ± .08		05/27/2015	06/03/2015	1:2		1
INTERNAL RADII .015	.XX= ± .01	.XX= ± .02	.XX= ± .04						
BREAK SHARP CORNERS .005 TO .015	.XXX= ± .005	.XXX= ± .01	.XXX= ± .02						
HOLES: NOMINAL, +1/64	LINEAR DIMENSION LIMITS:FRACTIONAL			SOFTWARE:	NEXT ASSEMBLY:		DRAWING NUMBER:		REV: SIZE:
CONCENTRICITY: .010 TIR	0-6"	6-12"	12-∞"						
ANGLES: ± 1/2°	± 1/32	± 1/16	± 1/8	INVENTOR 2015			30149-2		A

(Ø7.0 STK.)

4 X 1/4-28 UNF ▼ .50 △1
EQ. SP. ON Ø6.00 P.C.D.

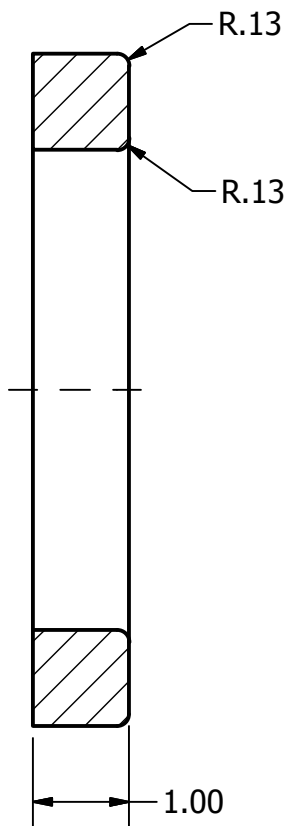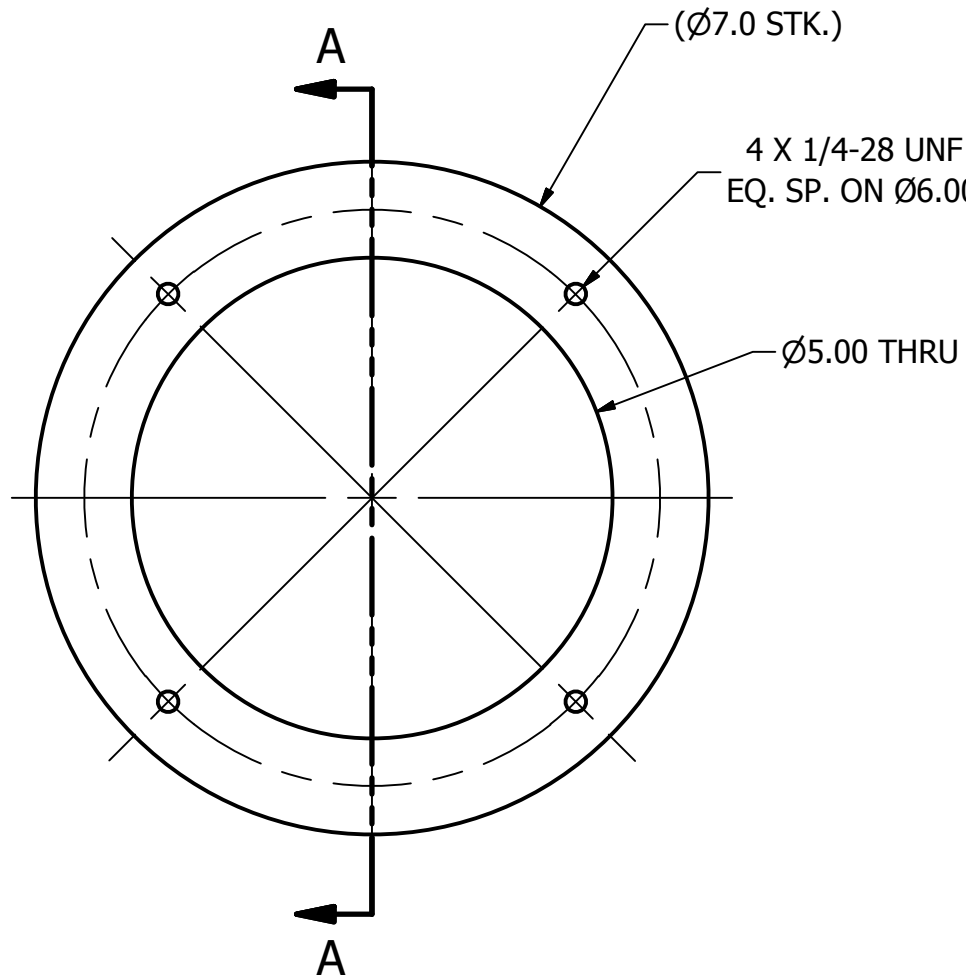Ø5.00 THRU

A

A

R.13

R.13

1.00

SECTION A-A

NOTES:

1. DO NOT BREAK THROUGH.

National Research Council Canada

INSTITUTE FOR AEROSPACE RESEARCH
STRUCTURES, MATERIALS & PERFORMANCE LABORATORY

DROP TOWER SCREW JACK
CONTACT RING

REQUIREMENTS - UNLESS OTHERWISE SPECIFIED

GENERAL

DIMENSIONS ARE IN INCHES
MACHINE FINISH: 125 µ IN. RMS
INTERNAL RADII .015
BREAK SHARP CORNERS .005 TO .015
HOLES: NOMINAL, +1/64
CONCENTRICITY: .010 TIR
ANGLES: ± 1/2°

LINEAR DIMENSION LIMITS:DECIMAL		
0-6"	6-12"	12-∞"
.X= ± .02	.X= ± .04	.X= ± .08
.XX= ± .01	.XX= ± .02	.XX= ± .04
.XXX= ± .005	.XXX= ± .01	.XXX= ± .02

LINEAR DIMENSION LIMITS:FRACTIONAL		
0-6"	6-12"	12-∞"
± 1/32	± 1/16	± 1/8

PROJECT CODE: A1-005561	DRAWN BY: J.MACMILLAN	APPROVED BY: J. ROGERS	MATERIAL SPECIFICATION: ALUMINUM	
	DATE DRAWN:M/D/Y 05/20/2015	DATE APPROVED: 06/03/2015	SCALE: 1:2	QUANTITY: 1
SOFTWARE: INVENTOR 2015	NEXT ASSEMBLY:		DRAWING NUMBER: 30149-3	REV: SIZE: A

18.00

16.00

Ø4.0 THRU

4 X Ø.530 THRU
⌴ Ø.790 ▽ .515

(1.0 STK.)

14.00

16.00

National Research Council Canada

INSTITUTE FOR AEROSPACE RESEARCH
STRUCTURES, MATERIALS & PERFORMANCE LABORATORY

TITLE
DROP TOWER NEW UPPER PLATE

REQUIREMENTS - UNLESS OTHERWISE SPECIFIED

GENERAL

DIMENSIONS ARE IN INCHES
MACHINE FINISH: 125 μ IN. RMS
INTERNAL RADII .015
BREAK SHARP CORNERS .005 TO .015
HOLES: NOMINAL, +1/64
CONCENTRICITY: .010 TIR
ANGLES: ± 1/2°

LINEAR DIMENSION LIMITS:DECIMAL

	0-6"	6-12"	12-∞"
.X=	± .02	.X= ± .04	.X= ± .08
.XX=	± .01	.XX= ± .02	.XX= ± .04
.XXX=	± .005	.XXX= ± .01	.XXX= ± .02

LINEAR DIMENSION LIMITS:FRACTIONAL

0-6"	6-12"	12-∞"
± 1/32	± 1/16	± 1/8

PROJECT CODE: A1-005561	DRAWN BY: J.MACMILLAN	APPROVED BY: J. ROGERS	MATERIAL SPECIFICATION: STEEL
	DATE DRAWN:M/D/Y 05/27/2015	DATE APPROVED: 06/03/2015	SCALE: 1:4 / QUANTITY: 1
SOFTWARE: INVENTOR 2015	NEXT ASSEMBLY:	DRAWING NUMBER: 30149-4	REV: A / SIZE:

(18.0)

(16.0)

11.00

2.75

℄

1

4 X Ø.53 THRU

℄   ℄   3.50   10.00   (14.0)   (16.0)

4 X 3/8-16 UNC THRU

℄

(1⅛ STK.)

NOTES:
1. 8 HOLES ADDED TO EXISTING PLATE.
2. SOME EXISTING HOLES NOT DIMENSIONED
   FOR CLARITY.

ISSUED FOR REFERENCE

TITLE:
DROP TOWER MODIFIED LOWER
PLATE

REQUIREMENTS - UNLESS OTHERWISE SPECIFIED

GENERAL	LINEAR DIMENSION LIMITS:DECIMAL		
DIMENSIONS ARE IN INCHES	0-6"	6-12"	12-∞"
MACHINE FINISH: 125 μ IN. RMS	.X= ±.02	.X= ±.04	.X= ±.08
INTERNAL RADII .015	.XX= ±.01	.XX= ±.02	.XX= ±.04
BREAK SHARP CORNERS .005 TO .015	.XXX= ±.005	.XXX= ±.01	.XXX= ±.02
HOLES: NOMINAL, +1/64	LINEAR DIMENSION LIMITS:FRACTIONAL		
CONCENTRICITY: .010 TIR	0-6"	6-12"	12-∞"
ANGLES: ± 1/2°	± 1/32	± 1/16	± 1/8

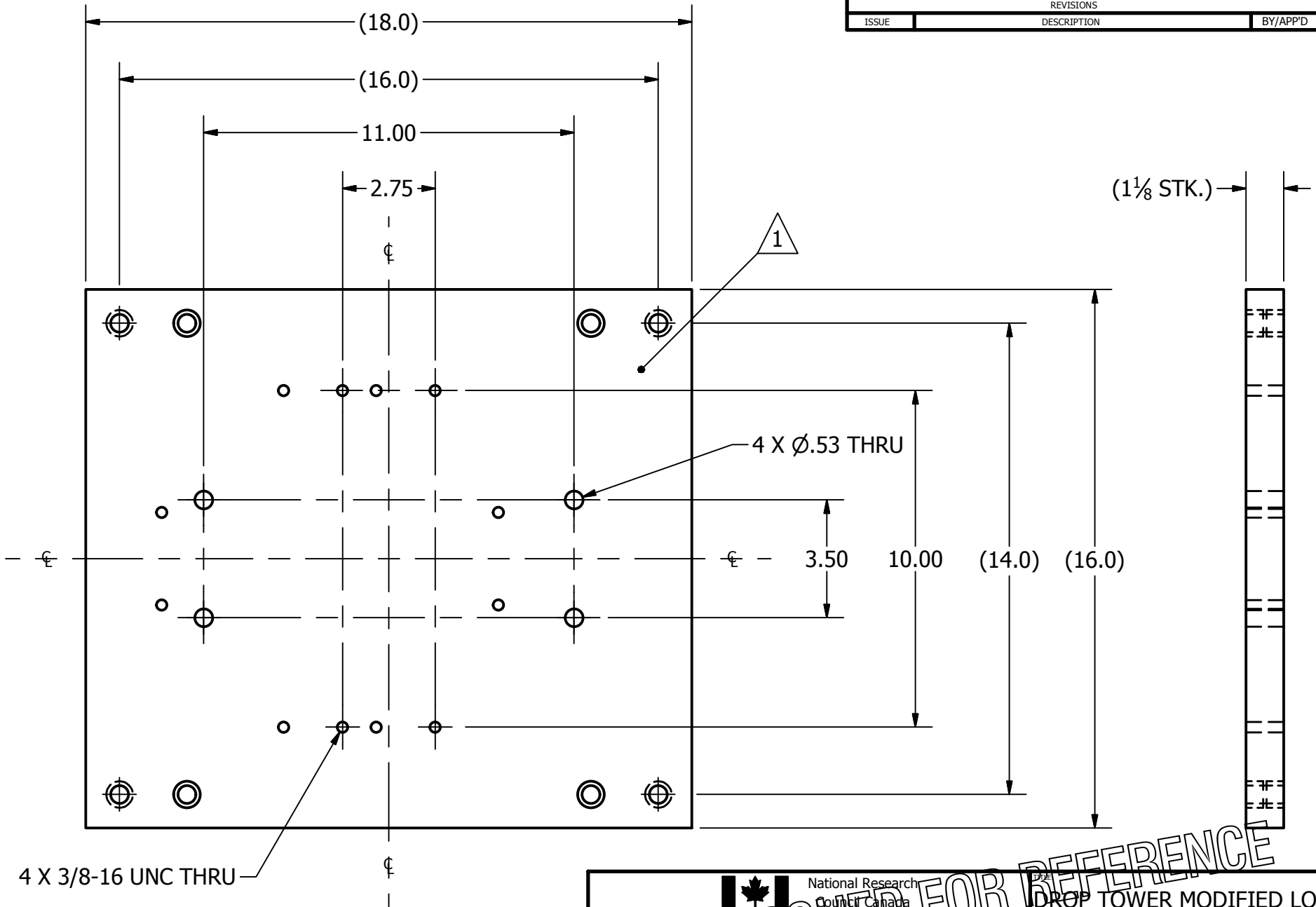| PROJECT CODE: A1-005561	DRAWN BY: J.MACMILLAN	APPROVED BY: J. ROGERS	MATERIAL SPECIFICATION: STEEL
	DATE DRAWN:M/D/Y 05/27/2015	DATE APPROVED: 06/03/2015	SCALE: 1:4 · QUANTITY: 1
SOFTWARE: INVENTOR 2015	NEXT ASSEMBLY:		DRAWING NUMBER: 30149-5 · REV: A · SIZE: A

12.00

10.00

(.75 STK.)

Ø6.38 THRU

4 X Ø.41 THRU

2.75

8.00

National Research Council Canada

INSTITUTE FOR AEROSPACE RESEARCH
STRUCTURES, MATERIALS & PERFORMANCE LABORATORY

DROP TOWER SCREW JACK RETAINER

REQUIREMENTS - UNLESS OTHERWISE SPECIFIED					PROJECT CODE:	DRAWN BY:	APPROVED BY:	MATERIAL SPECIFICATION:		
GENERAL	LINEAR DIMENSION LIMITS:DECIMAL				A1-005561	J.MACMILLAN	J. ROGERS	ALUMINUM		
DIMENSIONS ARE IN INCHES		0-6"	6-12"	12-∞"						
MACHINE FINISH: 125 μ IN. RMS		.X= ± .02	.X= ± .04	.X= ± .08		DATE DRAWN:M/D/Y	DATE APPROVED:	SCALE:		QUANTITY:
INTERNAL RADII .015		.XX= ± .01	.XX= ± .02	.XX= ± .04		05/27/2015	06/03/2015	1:2		1
BREAK SHARP CORNERS .005 TO .015		.XXX= ± .005	.XXX= ± .01	.XXX= ± .02						
HOLES: NOMINAL, +1/64	LINEAR DIMENSION LIMITS:FRACTIONAL				SOFTWARE:	NEXT ASSEMBLY:		DRAWING NUMBER:		REV: SIZE:
CONCENTRICITY: .010 TIR		0-6"	6-12"	12-∞"						
ANGLES: ± 1/2°		± 1/32	± 1/16	± 1/8	INVENTOR 2015			30149-6		A

C   C-scan Tap Test Equipment Data Sheets

The following provides the data sheets for the *Endevco* Modal hammer and the PicoScope oscilloscope used in the C-scan tap test.

PicoScope® 2200A Series

PC OSCILLOSCOPES WITH ARBITRARY WAVEFORM GENERATOR

Benchtop performance in a pocket-sized scope

2 CHANNELS • LOW COST • 200 MHz BANDWIDTH

Up to 1 GS/s sampling rate

Arbitrary waveform generator

Advanced digital triggers

Persistence display modes

USB connected and powered

Free software upgrades

Mask limit testing

Serial bus decoding

5 YEAR WARRANTY
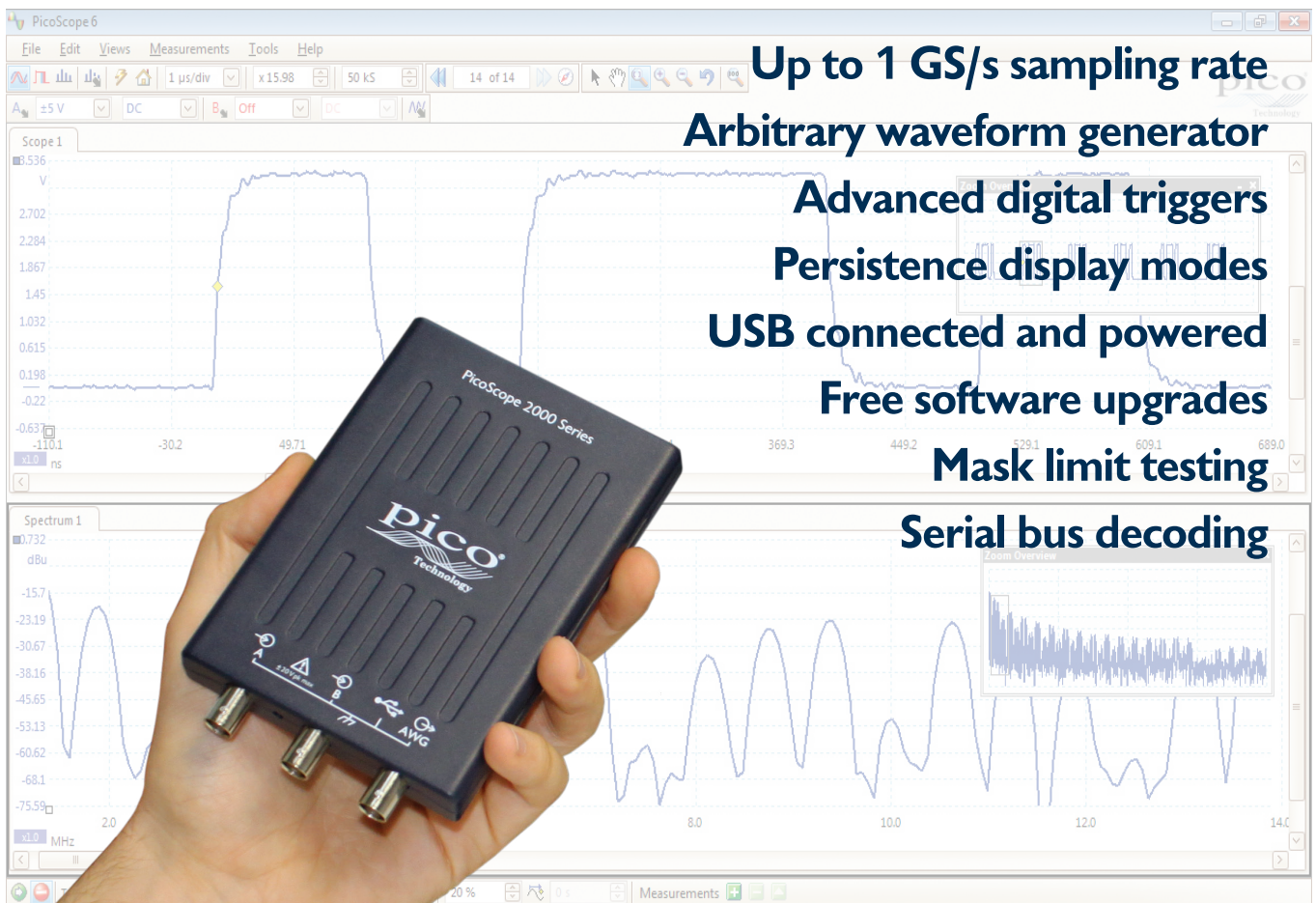
Powerful, portable, and versatile

The PicoScope 2200A Series oscilloscopes offer a small, light, modern alternative to bulky benchtop devices. You can now fit a 200 MHz, 1 GS/s instrument easily in your laptop bag! They are perfect for engineers on the move; ideal for a wide range of applications including design, test, education, service, monitoring, fault finding, and repair.

A small form factor is not the only benefit of these PC-based scopes. With our PicoScope 6 software, high-end features such as serial decoding and mask limit testing are included as standard. New functionality is regularly delivered through free upgrades, optimized with the help of feedback from our customers.

USB connectivity

The USB connection makes printing, copying, saving, and emailing your data from the field quick and easy. The high-speed USB interface allows fast data transfer, while USB powering removes the need to carry around a bulky external power supply.

Fast sampling

The PicoScope 2200A Series oscilloscopes provide fast real-time sampling rates up to 1 GS/s, equivalent to a timing resolution of only 1 ns. For repetitive signals, equivalent-time sampling (ETS) mode can boost the maximum effective sampling rate up to 10 GS/s, allowing even finer resolution down to 100 ps. All scopes support pre-trigger and post-trigger capture.

Arbitrary waveform and function generators

All PicoScope 2200A Series oscilloscopes have a built-in arbitrary waveform generator (AWG). Waveforms can be imported from data files or created and modified using the built-in graphical AWG editor.

A function generator is also included, with sine, square, triangle, DC level and many more standard waveforms. As well as level, offset and frequency controls, advanced options allow y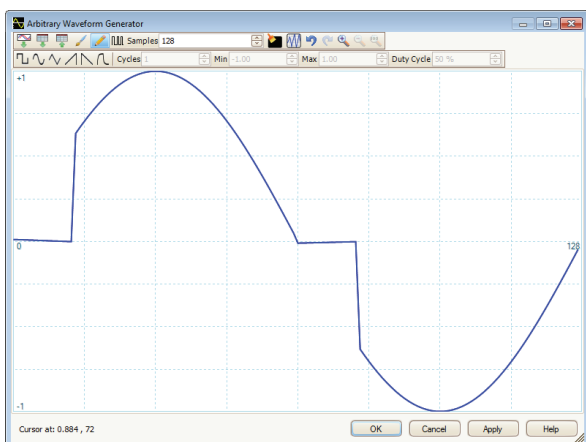ou to sweep over a range of frequencies. Combined with the spectrum peak hold option, this creates a powerful tool for testing amplifier and filter responses.

Digital triggering

Most digital oscilloscopes still use an analog trigger architecture based on comparators. This can cause time and amplitude errors that cannot always be calibrated out. The use of comparators often limits the trigger sensitivity at high bandwidths and can also create a long trigger re-arm delay.
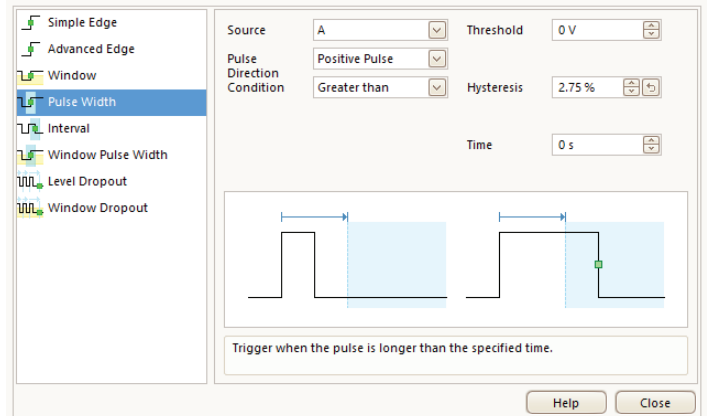
For over 20 years Pico have been pioneering the use of full digital triggering using the actual digitized data. This reduces trigger errors and allows our oscilloscopes to trigger on the smallest signals, even at the full bandwidth. All triggering is digital, resulting in high threshold resolution within programmable hysteresis and optimal waveform stability.

On selected models, the reduced re-arm delay provided by digital triggering, together with segmented memory, allows the capture of events that happen in rapid sequence. At the fastest timebase, rapid triggering can capture a new waveform every 2 microseconds until the buffer is full. The mask limit testing function helps to detect waveforms that fail to meet your specifications.

Advanced triggers

As well as the standard range of triggers found on most oscilloscopes, the PicoScope 2200A Series offers one of the best selections of advanced triggers available. These include pulse width, windowed and dropout triggers to help you find and capture your signal quickly.
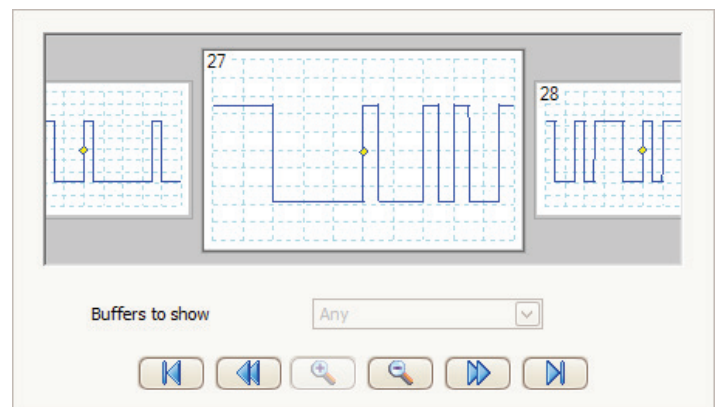
High signal integrity

Most oscilloscopes are built down to a price. PicoScopes are built up to a specification.

Careful front-end design and shielding reduces noise, crosstalk and harmonic distortion. Decades of oscilloscope design experience can be seen in improved pulse response and bandwidth flatness. We are proud of the dynamic performance of our products and publish these specifications in detail. The result is simple: when you probe a circuit, you can trust in the waveform you see on the screen.

Color persistence modes

Advanced display modes allow you to see old and new data superimposed, with new data in a brighter color or shade. This makes it easy to see glitches and dropouts and to estimate their relative frequency. Choose between analog persistence, digital color, or custom display modes.

Spectrum analyzer

With the click of a button, you can open a new window to display a spectrum plot of selected channels up to the full bandwidth of the oscilloscope. A comprehensive range of settings gives you control over the number of spectrum bands, window types and display modes.

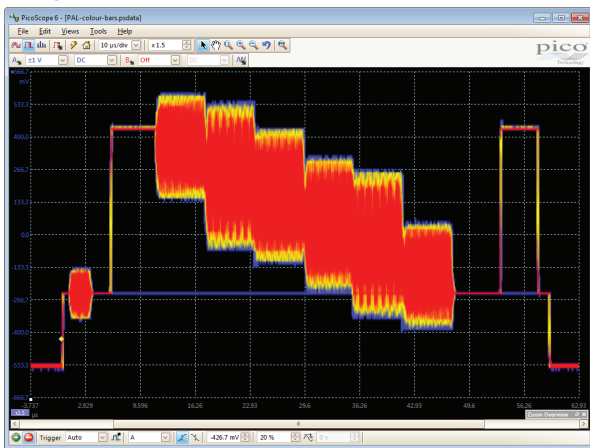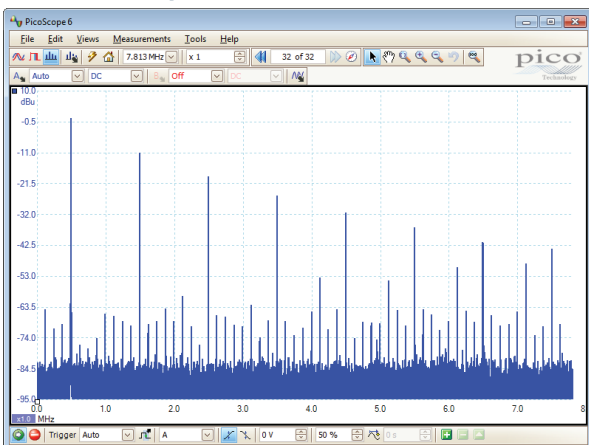PicoScope software allows you to display multiple spectrum views with different channel selections and zoom factors, and see these alongside time-domain waveforms of the same data. A comprehensive set of automatic frequency-domain measurements can be added to the display, including THD, THD+N, SINAD, SNR and IMD. You can even use the AWG and spectrum mode together to perform swept scalar network analysis.

Automatic measurements

PicoScope allows you to automatically display a table of calculated measurements for troubleshooting and analysis. Using the built-in measurement statistics you can see the average, standard deviation, maximum and minimum of each measurement as well as the live value.

You can add as many measurements as you need on each view. Each measurement includes statistical parameters showing its variability.

For information on the measurements available in scope and spectrum modes, see **Automatic Measurements** in the **Specifications** table.
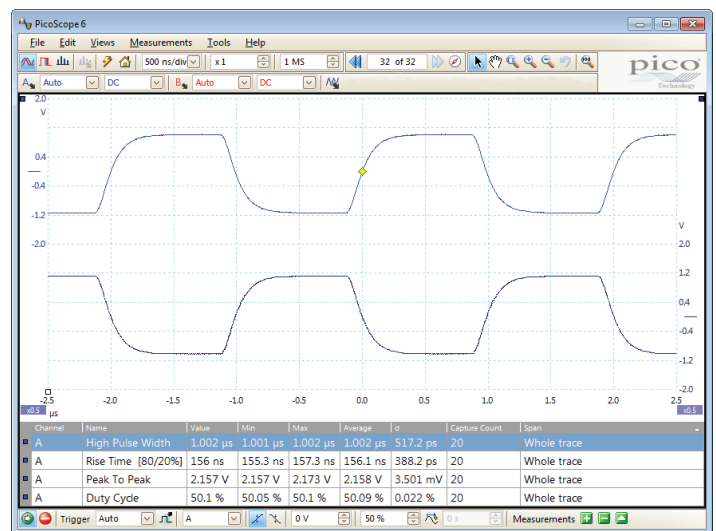
Channel	Name	Value	Min	Max	Average
A	High Pulse Width	1.002 µs	1.001 µs	1.002 µs	1.002 µs
A	Rise Time [80/20%]	156 ns	155.3 ns	157.3 ns	156.1 ns
A	Peak To Peak	2.157 V	2.157 V	2.173 V	2.158 V
A	Duty Cycle	50.1 %	50.05 %	50.1 %	50.09 %

15 scope mode measurements
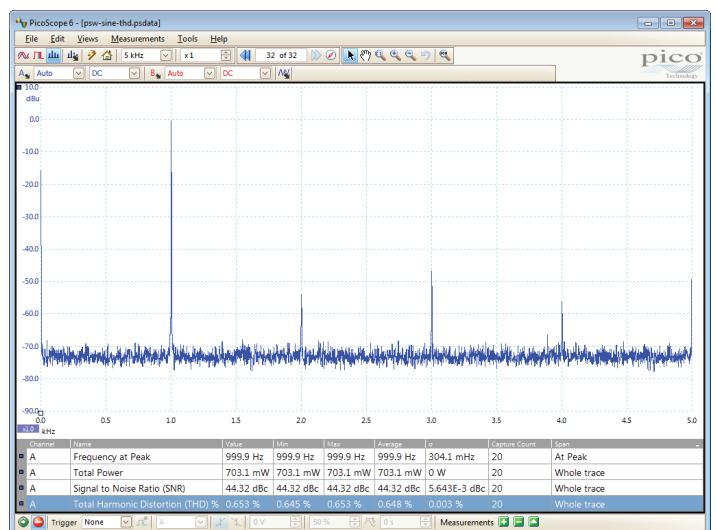
Channel	Name	Value	Min
A	Frequency at Peak	999.9 Hz	999.9 Hz
A	Total Power	703.1 mW	703.1 mW
A	Signal to Noise Ratio (SNR)	44.32 dBc	44.32 dBc
A	Total Harmonic Distortion (THD) %	0.653 %	0.645 %

11 spectrum mode measurements

Math channels
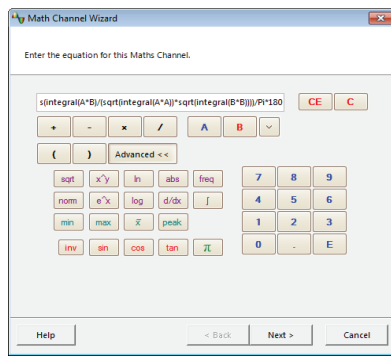
With PicoScope 6 you can perform a variety of mathematical calculations on your input signals and reference waveforms.

Use the built-in list for simple functions such as addition and inversion, or open the equation editor and create complex functions involving trigonometry, exponentials, logarithms, statistics, integrals and derivatives.

Serial decoding

The PicoScope 2200A Series oscilloscopes include serial decoding capability as standard. The decoded data can be displayed in the format of your choice: **In view**, **In window**, or both at once.
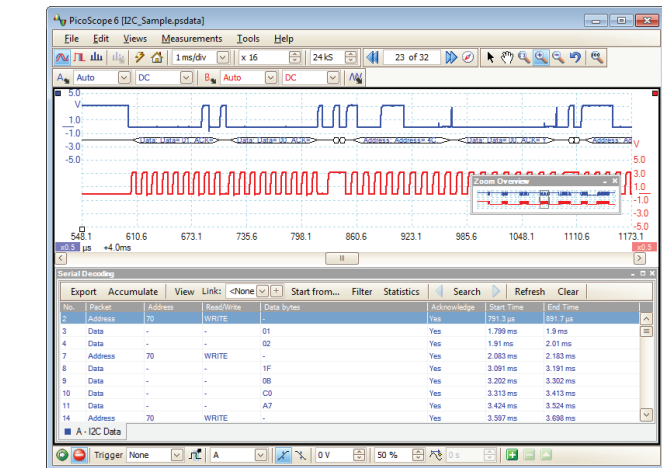
• **In view** format shows the decoded data beneath the waveform on a common time axis, with error frames marked in red. These frames can be zoomed to investigate noise or distortion.

• **In window** format shows a list of the decoded frames, including the data and all flags and identifiers. You can set up filtering conditions to display only the frames you are interested in, search for frames with specified properties, or define a start pattern to signal when the program should list the data.

Serial protocols
UART/RS-232
SPI
I²C
I²S
CAN
LIN

It is also possible to create a spreadsheet to decode the hexadecimal data into user-defined text strings.

High-speed data acquisition and digitizing

The supplied drivers and software development kit allow you to both write your own software and interface to popular third-party software packages such as LabVIEW and MATLAB.

The drivers support data streaming, a mode that captures gap-free continuous data over the USB port directly to the PC's RAM or hard disk at a rate of 1 to 9.6 MS/s, so you are not limited by the size of the scope's buffer memory. Sampling rates in streaming mode are subject to PC specifications and application loading.

Mask limit testing

PicoScope allows you to draw a mask around any signal with user-defined tolerances. This has been designed specifically for production and debugging environments, enabling you to compare signals. Simply capture a known good signal, draw a mask around it, and then attach the system under test. PicoScope will capture any intermittent glitches and can show a failure count and other statistics in the **Measurements** window.

The numerical and graphical mask editors can be used separately or in combination, allowing you to enter accurate mask specifications, modify existing masks, and import and export masks as files.
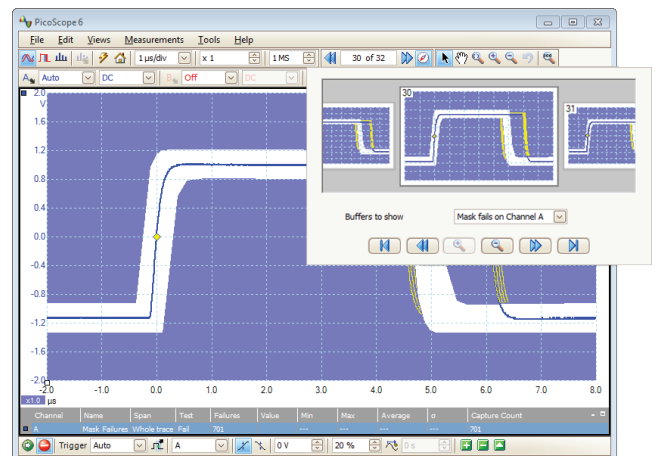
Custom probe settings
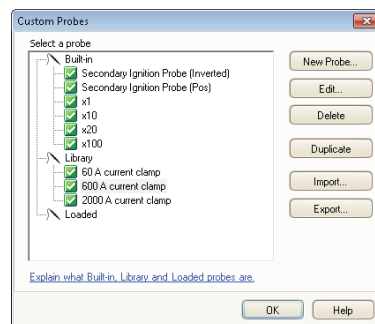
The custom probes menu allows you to correct for gain, attenuation, offsets and nonlinearities of probes and transducers, or convert your waveform data to different units such as current, scaled voltage, temperature, pressure, power or dB. Definitions can be saved to disk for later use. Definitions for standard Pico-supplied oscilloscope probes and current clamps are built in, but you can also create your own using linear scaling or even an interpolated data table.

High-end features as standard

Buying a PicoScope is not like making a purchase from other oscilloscope companies, where optional extras considerably increase the price. With our scopes, high-end features such as resolution enhancement, mask limit testing, serial decoding, advanced triggering, automatic measurements, math channels, XY mode, segmented memory (where available), and a signal generator are all included in the price.

To protect your investment, both the PC software and firmware inside the scope can be updated. Pico Technology have a long history of providing new features for free through software downloads. We deliver on our promises of future enhancements year after year, unlike many other companies in the field. Users of our products reward us by becoming lifelong customers and frequently recommending us to their colleagues.

The PicoScope 6 Software

PicoScope: The display can be as simple or as detailed as you need. Begin with a single view of one channel, and then expand the display to include any number of live channels, math channels and reference waveforms.

Tools > Serial decoding: Decode multiple serial data signals and display the data alongside the physical signal or as a detailed table.

Tools > Reference channels: Store waveforms in memory or on disk and display them alongside live inputs. Ideal for diagnostics and production testing.

Tools > Masks: Automatically generate a test mask from a waveform or draw one by hand. PicoScope highlights any parts of the waveform that fall outside the mask and shows error statistics.

Channel options: Offset, scaling, resolution enhancement, custom probes.

Auto setup button: Configures the timebase and voltage ranges for stable display of signals.

Trigger marker: Drag to adjust trigger level and pre-trigger time.

Oscilloscope controls: Controls such as voltage range, scope resolution, channel enable, timebase and memory depth are placed on the toolbar for quick access, leaving the main display area clear for waveforms.

Signal generator: Generates standard signals or arbitrary waveforms. Includes frequency sweep mode.

Waveform replay tools: PicoScope automatically records up to 10,000 of the most recent waveforms. You can quickly scan through to look for intermittent events, or use the **Buffer Navigator** to search visually.

Zoom and pan tools: PicoScope makes it easy to zoom into large waveforms. Either use the zoom-in, zoom-out and pan tools, or click and drag in the Zoom Overview window for fast navigation.

Views: PicoScope is carefully designed to make the best use of the display area. The waveform view is much bigger and of a higher resolution than with a typical benchtop scope. You can add new scope and spectrum views with automatic or custom layouts.

Rulers: Each axis has two rulers that can be dragged across the screen to make quick measurements of amplitude, time and frequency.

Math channels: Combine input channels and reference waveforms using simple arithmetic, or create custom equations with trigonometric and other functions.

Ruler legend: Absolute and differential ruler measurements are listed here.
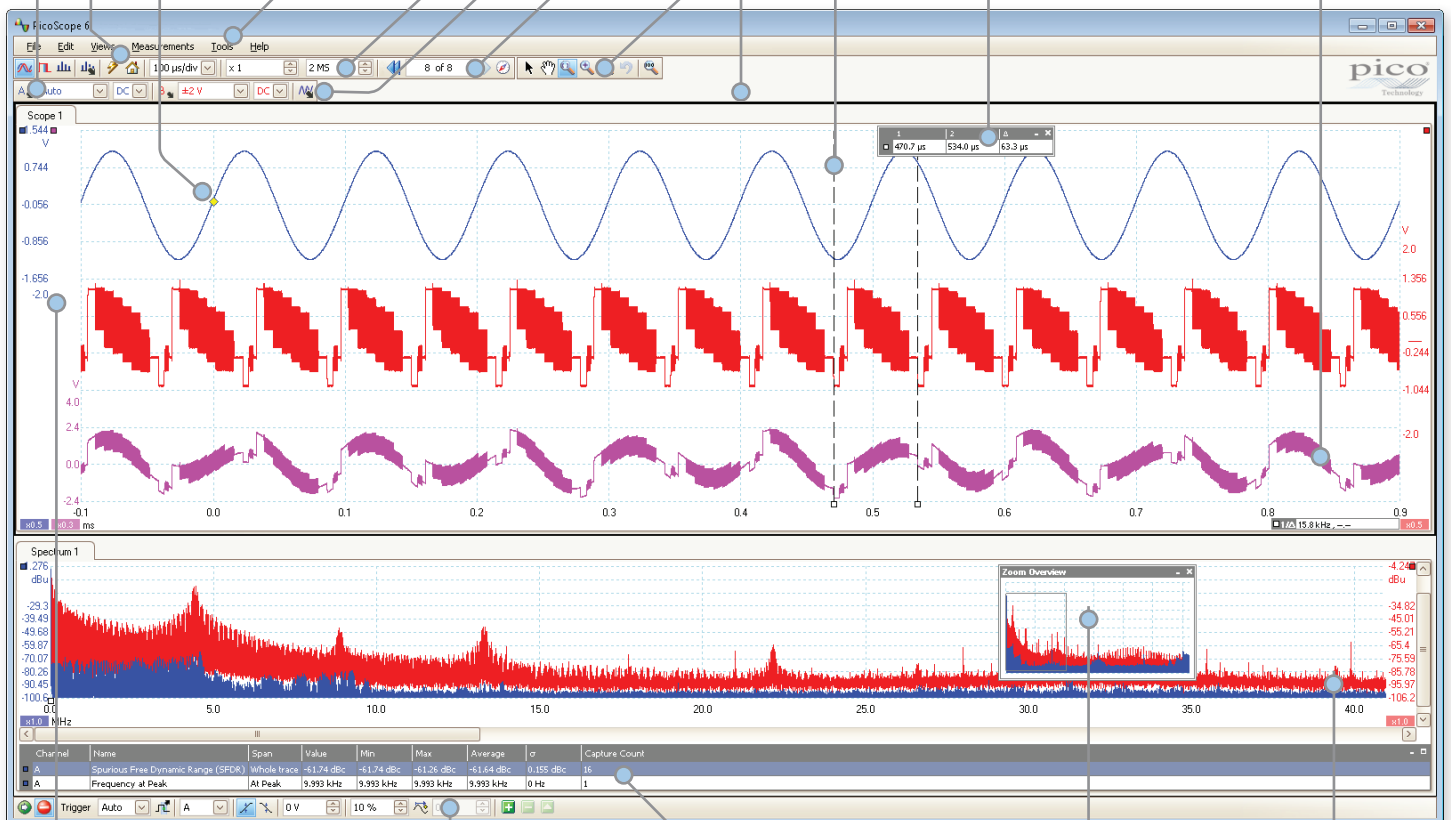
Movable axes: The vertical axes can be dragged up and down. This feature is particularly useful when one waveform is obscuring another. There's also an **Auto Arrange Axes** command.

Trigger toolbar: Quick access to main controls, with advanced triggers in a pop-up window.

Automatic measurements: Display calculated measurements for troubleshooting and analysis. You can add as many measurements as you need on each view. Each measurement includes statistical parameters showing its variability.

Zoom overview: Click and drag for quick navigation in zoomed views.

Spectrum view: View FFT data alongside scope view or independently.

PRODUCT SELECTOR

MODEL	PicoScope 2204A	PicoScope 2205A	PicoScope 2206A	PicoScope 2207A	PicoScope 2208A
Bandwidth (-3 dB)	10 MHz	25 MHz	50 MHz	100 MHz	200 MHz
Maximum sampling rate	100 MS/s	200 MS/s	500 MS/s	1 GS/s	1 GS/s
Buffer memory	8 kS	16 kS	32 kS	40 kS	48 kS
Function generator + AWG	100 kHz	100 kHz	1 MHz	1 MHz	1 MHz

DETAILED SPECIFICATIONS

VERTICAL					
Input channels	2				
Bandwidth (-3 dB)	10 MHz	25 MHz	50 MHz	100 MHz	200 MHz
Rise time (calculated)	35 ns	14 ns	7 ns	3.5 ns	1.75 ns
Vertical resolution	8 bits				
Enhanced vertical resolution	Up to 12 bits				
Input ranges	±50 mV, ±100 mV, ±200 mV, ±500 mV, ±1 V, ±2 V, ±5 V, ±10 V, ±20 V				
Input sensitivity	10 mV/div to 4 V/div (10 vertical divisions)				
Input coupling	AC / DC				
Input characteristics	BNC, 1 MΩ ‖ 14 pF		BNC, 1 MΩ ‖ 13 pF		
Analog offset range (vertical position adjustment)	-		±250 mV (50 mV to 200 mV ranges) ±2.5 V (500 mV to 2 V ranges) ±20 V (5 V to 20 V ranges)		
DC accuracy	±3% of full scale				
Overvoltage protection	±100 V (DC + AC peak)				

HORIZONTAL (TIMEBASE)					
Maximum sampling rate (real-time) 1 ch. / 2 ch.	100 MS/s 50 MS/s	200 MS/s (ChA) 100 MS/s	500 MS/s 250 MS/s	1 GS/s 500 MS/s	1 GS/s 500 MS/s
Equivalent sampling rate (ETS)	2 GS/s	4 GS/s	5 GS/s	10 GS/s	10 GS/s
Maximum sampling rate (streaming)	1 MS/s		9.6 MS/s		
Timebase ranges	10 ns to 5000 s/div	5 ns to 5000 s/div	2 ns to 5000 s/div	1 ns to 5000 s/div	500 ps to 5000 s/div
Buffer memory (shared between active channels)	8 kS	16 kS	32 kS	40 kS	48 kS
Buffer memory (streaming mode)	2 MS per channel in PicoScope software.		100 MS (shared) in PicoScope software. Up to available PC memory when using SDK.		
Maximum buffers (normal triggering)	10 000				
Max. buffers (rapid block triggering)	Not available		32		
Timebase accuracy	±100 ppm		±50 ppm		
Sample jitter	< 30 ps RMS		< 5 ps RMS		

DYNAMIC PERFORMANCE (typical)					
Crosstalk (full bandwidth)	Better than 200:1 (equal ranges)		Better than 400:1 (equal ranges)		
Harmonic distortion	< −50 dB at 100 kHz, full-scale input				
SFDR	> 52 dB at 100 kHz, full-scale input				
Noise	< 150 µV RMS (±50 mV range)		< 200 µV RMS (±50 mV range)		
Bandwidth flatness (at scope input)	(+0.3 dB, −3 dB) from DC to full bandwidth				

TRIGGERING					
Sources	Ch A, Ch B				
Trigger modes	None, auto, repeat, single		None, auto, repeat, single, rapid (segmented memory)		
Advanced triggers	Edge, window, pulse width, window pulse width, dropout, window dropout, interval, logic.				
Trigger types, ETS	Rising or falling edge				
Trigger sensitivity	Digital triggering provides 1 LSB accuracy up to full bandwidth In ETS mode, typical 10 mV p-p at full bandwidth				
Maximum pre-trigger capture	100% of capture size				
Maximum post-trigger delay	4 billion samples				
Trigger re-arm time	PC-dependent		< 2 µs on fastest timebase		
Maximum trigger rate	PC-dependent		Up to 32 waveforms in a 64 µs burst		

	PicoScope 2204A	PicoScope 2205A	PicoScope 2206A	PicoScope 2207A	PicoScope 2208A
FUNCTION GENERATOR					
Standard output signals	Sine, square, triangle, DC voltage, ramp, sinc, Gaussian, half-sine				
Pseudorandom output signals	None		White noise, PRBS		
Standard signal frequency	DC to 100 kHz		DC to 1 MHz		
Sweep modes	Up, down, dual with selectable start/stop frequencies and increments				
Triggering	-		Free-run or up to 1 billion waveform cycles or frequency sweeps. Triggered from scope trigger or manually.		
Output frequency accuracy	±100 ppm		±50 ppm		
Output frequency resolution	< 0.01 Hz				
Output voltage range	±2 V				
Output adjustments	Any amplitude and offset within ±2 V range				
Amplitude flatness (typical)	< 1 dB to 100 kHz		< 0.5 dB to 1 MHz		
DC accuracy	±1% of full scale				
SFDR (typical)	> 55 dB at 1 kHz full-scale sine wave		> 60 dB at 10 kHz full-scale sine wave		
Output characteristics	Front panel BNC, 600 Ω output impedance				
Overvoltage protection	±10 V				
ARBITRARY WAVEFORM GENERATOR					
Update rate	2 MS/s		20 MS/s		
Buffer size	4 kS		8 kS		
Resolution	12 bits				
Bandwidth	> 100 kHz		> 1 MHz		
Rise time (10% to 90%)	< 2 μs		< 120 ns		
SPECTRUM ANALYZER					
Frequency range	DC to 10 MHz	DC to 25 MHz	DC to 50 MHz	DC to 100 MHz	DC to 200 MHz
Display modes	Magnitude, average, peak hold				
Windowing functions	Rectangular, Gaussian, triangular, Blackman, Blackman-Harris, Hamming, Hann, flat-top				
Number of FFT points	Selectable from 128 to half available buffer memory in powers of 2				
MATH CHANNELS					
Functions	−x, x+y, x−y, x*y, x/y, x^y, sqrt, exp, ln, log, abs, norm, sign, sin, cos, tan, arcsin, arccos, arctan, sinh, cosh, tanh, freq, derivative, integral, min, max, average, peak, delay				
Operands	A, B (input channels), T (time), reference waveforms, constants, Pi				
AUTOMATIC MEASUREMENTS					
Scope mode	AC RMS, true RMS, cycle time, DC average, duty cycle, falling rate, fall time, frequency, high pulse width, low pulse width, maximum, minimum, peak to peak, rise time, rising rate.				
Spectrum mode	Frequency at peak, amplitude at peak, average amplitude at peak, total power, THD %, THD dB, THD plus noise, SFDR, SINAD, SNR, IMD				
Statistics	Minimum, maximum, average and standard deviation				
SERIAL DECODING					
Protocols	CAN, LIN, I²C, UART/RS-232, SPI, I²S, FlexRay				
MASK LIMIT TESTING					
Statistics	Pass/fail, failure count, total count				
DISPLAY					
Interpolation	Linear or sin(x)/x				
Persistence modes	Digital color, analog intensity, custom, or none				
GENERAL					
PC connectivity	USB 2.0 (USB 1.1 and 3.0 compatible). USB cable included.				
Power requirements	Powered from USB port				
Dimensions (including connectors)	142 x 92 x 19 mm				
Weight	< 0.2 kg (7 oz)				
Temperature range	Operating: 0 °C to 50 °C (20 °C to 30 °C for stated accuracy). Storage: −20 °C to +60 °C.				
Humidity range	Operating: 5% to 80% RH non-condensing. Storage: 5% to 95% RH non-condensing.				
Safety approvals	Designed to EN 61010-1:2010				
Compliance	RoHS, WEEE, and LVD compliant. Tested to meet EN61326-1:2006 and FCC Part 15 Subpart B.				
Software included	PicoScope 6, Windows and Linux SDK, example programs (C, Visual Basic, Excel VBA, LabVIEW)				
PicoScope software PC requirements	Microsoft Windows XP (SP3), Windows Vista, Windows 7 or Windows 8 (not Windows RT). 32- or 64-bit				
Languages (manual)	Chinese (simplified), English, French, German, Italian, Spanish				
Languages (software interface)	Chinese (simplified & traditional), Czech, Danish, Dutch, English, Finnish, French, German, Greek, Hungarian, Italian, Japanese, Korean, Norwegian, Polish, Portuguese, Romanian, Russian, Spanish, Swedish, Turkish				
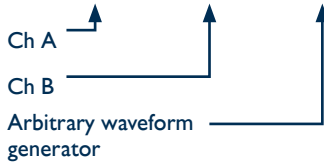
Pack Contents

- PicoScope 2200A Series oscilloscope
- USB cable
- Two x1/x10 passive probes
- Quick Start Guide
- Software and reference CD

Ch A

Ch B

Arbitrary waveform
generator

USB port

Matching probes included

Two x1/x10 passive probes are included, chosen
to match the bandwidth of your scope.

PicoScope model	Probes included	Order code
2204A 2205A 2206A	60 MHz probes (2)	MI007
2207A	150 MHz probes (2)	TA132
2208A	250 MHz probes (2)	TA131

Hand-held oscilloscopes

Also available in the PicoScope 2000 Series,
the PicoScope 2104 and 2105 single-channel
hand-held oscilloscopes are the ultimate in
compact design.

See www.picotech.com for details.

Ordering information

ORDER CODE	DESCRIPTION
PP906	PicoScope 2204A 10 MHz oscilloscope
PP907	PicoScope 2205A 25 MHz oscilloscope
PP908	PicoScope 2206A 50 MHz oscilloscope
PP909	PicoScope 2207A 100 MHz oscilloscope
PP910	PicoScope 2208A 200 MHz oscilloscope

For deeper memory, higher or flexible resolution, see the PicoScope 3000, 4000 and 5000 Series oscilloscopes.

UK headquarters:

Pico Technology
James House
Colmworth Business Park
St. Neots
Cambridgeshire
PE19 8YP
United Kingdom

☎ +44 (0) 1480 396 395
🖨 +44 (0) 1480 396 296
✉ sales@picotech.com

US headquarters:

Pico Technology
320 N Glenwood Blvd
Tyler
Texas 75702
United States

☎ +1 800 591 2796
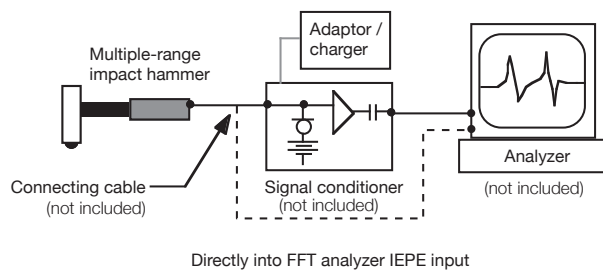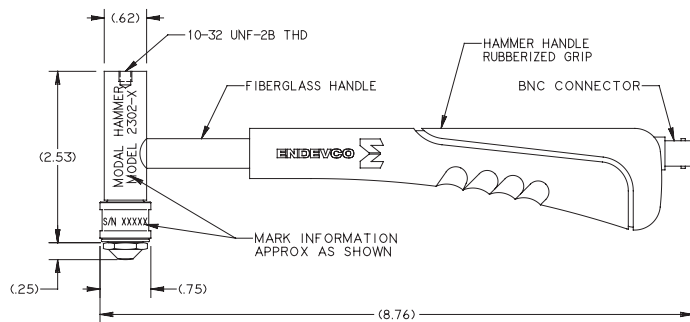🖨 +1 620 272 0981
✉ sales@picotech.com

www.picotech.com

pico
Technology

Model 2302
Modal hammer

Features

- Four ranges available (50, 100, 500, 1000 lbf)
- 3 replaceable tips
- Low impedance (Isotron®) output
- Acceleration compensated
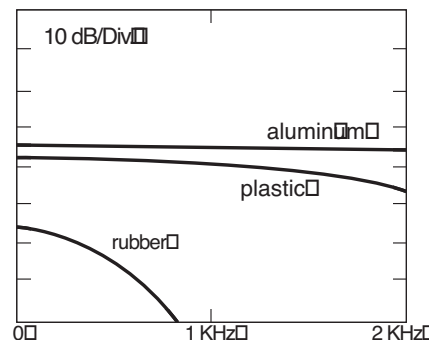- Ergonomically designed grip

Description

Scaled modal models require a precise force measurement. This can be achieved by electrodynamic and servohydraulic exciters controlled by a signal generator via a power amplifier. A more convenient and economical excitation method is a hammer fitted with a high-quality piezoelectric force transducer. In applications where a high crest factor and a limited ability to shape the input force spectrum is of no concern, impact hammer testing is an ideal source of excitation. Impact hammers are highly portable for field work and provide no unwanted mass loading to the structure under test.

The modal hammer excites the structure with a constant force over a frequency range of interest. Three interchangeable tips are provided which determine the width of the input pulse and thus the bandwidth. Typical force spectra produced with different tips are shown at the bottom.

For larger structures, an optional head extender is available to increase the head's mass. The hammer structure is acceleration compensated to avoid glitches in the spectrum due to hammer structure resonances. The ergonomically designed handle grip helps the user optimize control and reduce the possibility of "double hits".

The hammer features an Isotron impedance converter providing an IEPE output which is compatible with most FFT analyzers and data acquisition systems.

Endevco brand model 133, 2775B, 2793, 4416B, 4999, 6634C and Oasis 2000 (4990A-X with cards 428 and/or 433) signal conditioners are recommended for use with the 2302. To excite larger structures, see Endevco brand model 2303, 2304 and 2305 sledge hammers.

Directly into FFT analyzer IEPE input

Model 2302
Modal hammer

MEGGiTT
smart engineering for
extreme environments

Specifications

The following performance specifications are typical values, referenced at +75°F (+24°C, 4 mA and 100 Hz, unless otherwise noted.

	Units	-5	-10	-50	-100
Range (full scale)	lbf (N)	1000 (4448)	500 (2200)	100 (445)	50 (220)
Sensitivity (typical)	mV/lbf (mV/N)	5 (1.14)	10 (2.27)	50 (11.4)	100 (22.7)
Maximum force (typical)	lbf (N)	1000 (4448)			
Resonance frequency	kHz	●———————— 50 ————————●
Frequency range, (max)	kHz	●———————— 8 ————————●
Head mass	grams	●———————— 100 ————————●
Head diameter	inches (mm)	●———————— 0.75 (19) ————————●
Impact tip diameter	inches (mm)	●———————— 0.25 (6.4) ————————●
DC output bias	Vdc	●———————— 9 to 10 ————————●
Output impedance	Ohms	●———————— ‹ 100 ————————●
Full scale output	V	●———————— ±5 ————————●
Suppy voltage	Vdc	●———————— 18 to 24 ————————●
Suppy current	mA	●———————— 2 to 10 ————————●
Temperature range	°F (°C)	●———————— -67 to 257 (-55 to 125) ————————●
Overall length	in (mm)	●———————— 8.76 (223) ————————●
Sensor material		●———————— 17-4 PH stainless steel ————————●
Handle material		●———————— Fiberglass with rubber grip ————————●
Connector		●———————— BNC ————————●

Accessories

Product	Description	2302
	Carrying case	Included
EHM1208	Impact tip, aluminum	Included
EHM1209	Impact tip, plastic	Included
EHM1210	Impact tip, rubber	Included
EHM1653	Head extender	Optional
133	Signal conditioner	Optional
2775B	Signal conditioner	Optional
2793	Isotron® signal conditioner	Optional
4416B	Signal conditioner	Optional
4999	Signal conditioner	Optional
6634C	Signal conditioner	Optional
EW967	BNC to BNC, 6 ft cable	Optional
4990A-X	Oasis 2000 computer-controlled system with cards 428 and/or 433	Optional

Endevco complete modal front end system

Notes:

1. Only the 2 gram tips supplied with the hammer set should be used. Heavier or lighter tips may affect acceleration compensation.

2. To prevent damage to mounting threads, do not use excessive torque when installing/changing impact tips.

3. Maintain high levels of precision and accuracy using Meggitt's factory calibration services. Call Meggitt's inside sales force at 800-982-6732 for recommended inervals, pricing and turn around time for these services as well as for quotations on our standard products.

CERTIFIED ISO 9001
ACCREDITED
APPLIES TO CALIFORNIA FACILITY